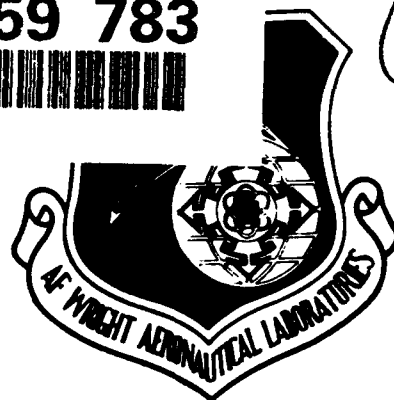


AFWAL-TR-86-4032

AD-A259 783



2

RAIN AND SOLID PARTICLE EROSION DAMAGE
MECHANISMS AND MATERIALS EVALUATIONS

Dr. S. van der Zwaag
Dr. J. P. Dear
D. Townsend
Dr. S. M. Walley

Physics and Chemistry of Solids
Cavendish Laboratory
Madingley Road
Cambridge CB3 0HE, U.K.

August 1986

Final Report: 1st October 1983 - 30th September 1984



Approved for Public Release: Distribution Unlimited

93-00302



7988

MATERIAL LABORATORY
AIR FORCE WRIGHT AERONAUTICAL LABORATORIES
AIR FORCE SYSTEMS COMMAND
WRIGHT-PATTERSON AIR FORCE BASE, OHIO 45433-6533

98

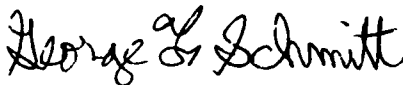
1 01 010

NOTICE

When Government drawings, specifications, or other data are used for any purpose other than in connection with a definitely Government-related procurement, the United States Government incurs no responsibility or any obligation whatsoever. The fact that the government may have formulated or in any way supplied the said drawings, specifications, or other data, is not to be regarded by implication, or otherwise in any manner construed, as licensing the holder, or any other person or corporation; or as conveying any rights or permission to manufacture, use, or sell any patented invention that may in any way be related thereto.

This report is releasable to the National Technical Information Service (NTIS). At NTIS, it will be available to the general public, including foreign nations.

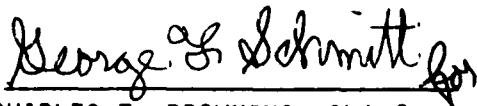
This technical report has been reviewed and is approved for publication.



George F. Schmitt, Project Engineer
Nonstructural Materials Branch
Nonmetallic Materials Division
Materials Directorate



KENT J. EISENTRAUT, Chief
Nonstructural Materials Branch
Nonmetallic Materials Division
Materials Directorate



CHARLES E. BROWNING, Chief
Nonmetallic Materials Division
Materials Directorate

If your address has changed, if you wish to be removed from our mailing list, or if the addressee is no longer employed by your organization please notify WL/MLBT, WPAFB, OH 45433-6533 to help us maintain a current mailing list.

Copies of this report should not be returned unless return is required by security considerations, contractual obligations, or notice on a specific document.

REPORT DOCUMENTATION PAGE

Form Approved
OMB No 0704 0183

Public reporting burden for this collection of information is estimated to average 1 hour per response, including the time for reviewing instructions, searching existing data sources, gathering and maintaining the data needed, and completing and reviewing the collection of information. Send comments regarding this burden estimate or any other aspect of this collection of information, including suggestions for reducing this burden, to Washington Headquarters Services, Directorate for Information Operations and Reports, 1215 Jefferson Davis Highway, Suite 1204, Arlington, VA 22202-4302, and to the Office of Management and Budget, Paperwork Reduction Project (0704-0183), Washington, DC 20503.

1. AGENCY USE ONLY (Leave blank)		2. REPORT DATE August 1986		3. REPORT TYPE AND DATES COVERED Final - 1 Oct 83 - 30 Sept 84	
4. TITLE AND SUBTITLE Rain and Solid Particle Erosion Damage Mechanisms and Materials Evaluations				5. FUNDING NUMBERS PE: 61102F/62103F PR: 2422 TA: 01 WU: 23	
6. AUTHOR(S) J.E Field, J. P. Dear, D. Townsend and S.M. Wally					
7. PERFORMING ORGANIZATION NAME(S) AND ADDRESS(ES) Physics & Chemistry of Solids Cavendish Laboratory Madingley Road Bollong AFB, DC 20332				8. PERFORMING ORGANIZATION REPORT NUMBER	
9. SPONSORING/MONITORING AGENCY NAME(S) AND ADDRESS(ES) George G. Schmitt (513/255-2334) Material Laboratory (WL/MLBT) Air Force Wright Aeronautical Laboratories Wright Patterson Air Force Base OH 45433-6533				10. SPONSORING/MONITORING AGENCY REPORT NUMBER AFWAL-TR-86-4032	
11. SUPPLEMENTARY NOTES					
12a. DISTRIBUTION/AVAILABILITY STATEMENT Approved for public release, distribution unlimited.				12b. DISTRIBUTION CODE	
13. ABSTRACT (Maximum 200 words) In the initial stage of liquid impact, high pressures are developed due to compressible behaviour of the liquid. This is followed by the release of liquid in the form of high speed jets. Studies of these processes in millimeter sized spherical drops is complicated. Some features are best studied using liquid shapes other than a sphere. Sec. II describes techniques using water/gelatine layers. The gel cut into shape and fired by a gas gun. This is viewed by high speed camera. Results are given for the shock structures, conditions, jetting and target impedance on impact. Sec. III describes methods developed for controlled single impacts. Reasonably Accurate results are obtained and methods for quantitative assessment are provided. Methods for improving accuracy are provided. Sec IV provides an analysis of double layer gel particles with different elastic properties. Sec V give novel methods of recording properties at strain rates of ca. $2 \times 10^4 \text{ s}^{-1}$. Data for a range of polymers is given.					
14. SUBJECT TERMS Rain, erosion, fracture, coatings, liquid impact				15. NUMBER OF PAGES 95	
				16. PRICE CODE	
17. SECURITY CLASSIFICATION OF REPORT unclassified	18. SECURITY CLASSIFICATION OF THIS PAGE unclassified	19. SECURITY CLASSIFICATION OF ABSTRACT unclassified	20. LIMITATION OF ABSTRACT UL		

TABLE OF CONTENTS

	PAGE
I. INTRODUCTION	1
II. STUDIES OF TWO-DIMENSIONAL LIQUID WEDGE IMPACT AND THEIR RELEVANCE TO LIQUID-DROP IMPACT PROBLEMS	3
2.1 INTRODUCTION	3
2.2 TRANSIENT PHENOMENA IN LIQUID IMPACT	5
2.3 EXPERIMENTAL	10
2.4 RESULTS:	13
(a) Wedge Impact	13
(b) Target admittance	14
(c) The double-angled wedge	14
2.5 DISCUSSION:	14
(a) Angle for jetting	15
(b) Jet velocity	17
(c) Cavitation in the drop	18
(d) Damage	19
(e) Drop oblateness	20
(f) Specimen orientation in erosion testing	20
(g) Other situations	21
2.6 CONCLUSIONS	21
REFERENCES	23
TABLES	25
FIGURE CAPTIONS	30
FIGURES	33
III. LIQUID JET APPARATUS FOR RAIN EROSION STUDIES	47
3.1 INTRODUCTION	47
3.2 JET IMPACT	48
3.3 PRACTICAL POINTS:	49
(a) Loading a chamber	49
(b) Reason for convex meniscus	49
(c) Low velocity shots; momentum exchanger	49
(d) PMMA	50
(e) Acoustic matching	50
3.4 DAMAGE ASSESSMENT	51
REFERENCES	52
FIGURE CAPTIONS	53
FIGURES	54

IV.	THE EFFECT OF DOUBLE LAYER COATINGS OF HIGH MODULUS ON CONTACT STRESSES	59
4.1	INTRODUCTION	59
4.2	THE MODEL	60
4.3	RESULTS:	61
	(a) The radial stress fields in two example programmes	61
	(b) Effect of the coating parameters on the radial stress in the substrate	62
	(c) Effect of the coating parameters on the interlayer stresses	63
	(d) Effect of the coating parameters on the surface stresses	63
4.4	DISCUSSION	64
4.5	CONCLUSIONS	65
	REFERENCES	67
	FIGURE CAPTIONS	68
	FIGURES	69
V.	COMPRESSIVE STRESS-STRAIN CURVES OF VARIOUS POLYMERS AT STRAIN RATES OF $2 \times 10^4 \text{ s}^{-1}$	78
5.1	INTRODUCTION	78
5.2	PRESENT EXPERIMENTS	83
	TABLE	86
	REFERENCES	87
	FIGURE CAPTIONS	88
	FIGURES	89

DTIC QUALITY INSPECTED 8

Accession For	
NTIS GRA&I	<input checked="" type="checkbox"/>
DTIC TAB	<input type="checkbox"/>
Unannounced	<input type="checkbox"/>
Justification	
By	
Distribution/	
Availability Codes	
Dist	Avail and/or Special
A-1	

SECTION I

The research on this contract has been concerned with (i) basic theoretical and experimental studies of liquid/solid impact, (ii) further developing the jet method for producing controlled impacts in the laboratory, (iii) extending our analytic studies on protective coatings, and (iv) developing techniques and obtaining high strain rate data on a range of polymers. Below, we summarise each of these areas which are then described in detail in Sections II to V.

In the initial stage of liquid drop impact, the contact region expands faster than the wave speed in the liquid. This causes compressible behaviour in the liquid, and high transient pressures. High velocity jetting results when the wave motion in the liquid overtakes the expanding contact edge and moves up the free surface of the drop. The detailed pressure fields in this early time history of impact have been calculated by one of us (Lesser 1981) for both two- and three-dimensional liquid masses and for targets of finite admittance. An important result is that the edge pressures exceed the central "water-hammer" pressure $\rho_0 C U_i$ and at the time of shock detachment approach ca. $3 \rho_0 C U_i$. At this stage the edge pressures, for both spherical drops and two-dimensional liquid wedges, depend only on the impact velocity and the instantaneous angle between the liquid and solid surfaces. This suggests that the essential features of the early stage of liquid impact can be usefully studied by producing impacts with two-dimensional liquid wedges and predicted data for pressures, shock angles and velocities are presented. Experiments are described in Section II for producing impacts with pre-formed shapes using water-gelatine mixes and observing the impact events with high-speed photography. The results confirm the main features of the model and give information on edge pressures, jetting, cavitation in the liquid and the effect of the admittance of the solid. The relevance of the results to the damage and erosion of materials subjected to liquid impact is discussed. In particular, it is possible to explain the apparently low damage threshold of some materials, the form of damage and its development with repeated impact. This study highlights the importance of the detailed surface geometry in the region of contact. A paper based on this section has been accepted by Proc. Roy. Soc. (Lond.)

We have described in earlier reports and papers the development of the Cambridge jet technique which can be used for simulating liquid drop impact. Section III summarises this development and gives practical details on its use. The advantages of the approach are that the specimen is kept stationary and that a wide range of drop sizes and impact velocities can be obtained.

In an earlier paper (van der Zwaag and Field 1982), we investigated, using finite element methods, the effect of a thin hard coating on the stress field generated by a spherical indenter on a uniform halfspace. Of particular practical interest was the reduction in the maximum (radial) tensile stresses in the substrate solid as the modulus and thickness of the coating increased. Experimental support for the theoretical predictions was given in van der Zwaag and Field (1983). As reported in Section IV, the investigation is extended to examine the potential of double-layer coatings of two different high modulus materials. It is shown that a suitable selection of the properties of the two layers can reduce the tensile stresses in the substrate solid compared with the values in an uncoated substrate. Two particular systems are examined in detail. Potential benefits of monolayer and multilayer coatings are discussed critically. The results have application to a range of practical problems. A paper on this topic has been submitted to Phil. Mag.

Under impact conditions, the strain rates involved can be very high. It is important, therefore, to know the properties of materials at these high strain rates. Section V describes a novel technique which we have developed for recording the properties of solids at strain rates of ca. $2 \times 10^4 \text{ s}^{-1}$. Data is given in this report for a range of polymers.

SECTION II

STUDIES OF TWO-DIMENSIONAL LIQUID WEDGE IMPACT AND THEIR RELEVANCE TO LIQUID-DROP IMPACT PROBLEMS

2.1 INTRODUCTION

As is well known, the collision between a liquid mass and a solid surface can generate high transient pressures and cause significant damage, particularly if the impact velocity is high. The high pressures have been attributed to compressible behaviour in the liquid. The fact that numerous situations exist in which such collisions occur has made the study of liquid impact crucial for the further development of related technologies. The interested reader can find details in the proceedings of several recent international conferences and collections of review articles on rain erosion, steam turbine blade erosion, cavitation, jet cutting and associated topics (Bowden 1966, Adler 1979a, Field 1979, Preece 1979, B.H.R.A. 1972, 1974, 1976, 1978, 1980, 1982, Field and Corney 1983, Lesser and Field 1983a). However, despite considerable activity in the subject there exists a large number of unexplained and poorly understood phenomena associated with liquid impact. The reasons for this are connected with the fact that the high pressures and much of the damage formation take place during a very short time period following the initial contact, and as we will show involve a complex dependence on the geometry of the liquid and solid surfaces in the contact area.

Considerable progress has been made in overcoming these obstacles by making extensive use of high speed photographic techniques and rapid response crystal gauges. One result of this work is that when a curved liquid drop strikes a solid, the highest pressures do not occur at the centre of impact where the normals to both the liquid and solid surfaces are parallel (figure 1) but on a nearly circular boundary at a distance which depends on the drop radius and the velocity of impact (see reviews by Brunton and Rochester 1979, Adler 1979b, Lesser and Field 1983a). Another result is that after an interval comparable to the time it takes the drop to spread out to the maximum pressure radius, a "jetting" motion develops (figure 2). In certain impact speed ranges this jet has been observed to have a speed up to ten times the impact speed (Jenkins and Booker 1960, Fyall 1967, Brunton and Camus 1970a, Camus 1971).

The study of these events has been considerably complicated by the fact

that for the drop sizes normally used in experiments, which are typically up to a few millimeters in diameter, both the "jetting" and high pressure thresholds are reached when the intercept angle between drop edge and solid surface is, at most, a few degrees. Thus it becomes difficult to interpret the photographic evidence, and to observed the detailed behaviour of the liquid in the critical zone.

The main object of the present investigation was to overcome these experimental difficulties by the use of a technique designed to isolate the behaviour of the liquid in the critical zone and to prolong the duration of the critical period between the attainment of maximum "edge" pressure and "jetting". The rationale of our method is based on the mechanics of wave fronts spreading through the drop during the initial collision period. The liquid is compressed by the collision, and the compression is signalled to the unaffected portions of the drop by waves moving at sonic speeds and even considerably exceeding the sound speed in the undisturbed liquid. One of these waves will be attached to the spreading edge contact point (figure 1) and, as first observed by Heymann (1969), this wave will be a shock which can be calculated by the use of conservation laws. Such a calculation shows that the edge pressures (see also below) can easily attain values up to about three times the normal impact pressure. Thus a crucial aspect of any liquid impact involves this attached shock. The present experiment is designed to study how the impact parameters of collision velocity and surface geometry influence this wave system. In particular, we shall be concerned with how such a shock system can become detached from the solid surface, and how this detachment process leads to the formation of "jetting".

One of us (Lesser (1981) has carried out significant extensions of Heymann's work which shows that the shock system at the edge of a spreading spherical drop (figure 1a) and the plane shock developed on a two-dimensional wedge-shaped impact surface (figure 1b) are in a certain sense equivalent. This equivalence applies exactly in the vicinity of the edge when the wedge angle equals the tangent angle of the oncoming drop at the contact edge, and the impact speed of the oncoming wedge equals the drop impact speed. The implications and some of the theory which bears upon the present experiments are discussed further in section 2. It is important to appreciate that during the crucial initial stage of impact the information that a collision has taken place is confined to the liquid region reached by the compression wave developed during the initial contact. This means (figure 1) that the collision with a large drop can be effectively studied by using a sector of liquid. As shown in Lesser (1981) the pressure field is higher in the interior of a cylindrical or two-dimensional drop than a spherical drop, how-

ever, the edge behaviour is identical in both the two- and three-dimensional cases. Thus it becomes reasonable to simplify the experimental study of the collision by using two-dimensional, preformed liquid shapes which are struck by a moving "target". This technique has been in part employed by Brunton and Camus (1970a and b), Camus (1971) and by Rochester and Brunton (1979) to study the impact with curved liquid surfaces. What is new in the present work is the use of a water/gelatine mix that allows the "liquid" to be preformed into any desired shape, yet which gives liquid behaviour under the high strain rates of the experiment, thus providing strong control of the impact parameters. This method makes detailed observations of the liquid behaviour possible during the critical phase of edge shock detachment.

In the next section a qualitative summary of the theory developed in Lesser (1981) and Lesser and Field (1983a) is presented, to the extent needed to understand the experiments. The experimental techniques employed in our investigation and a number of particular events are then described. In the concluding section we discuss some of the implications of the experiments and their significance to the problems of liquid impact erosion of surface and related phenomena.

2.2 TRANSIENT PHENOMENA IN LIQUID IMPACT

From the point of view of erosion or material damage, the most significant part of a liquid solid impact event occurs during a period of the order of a few microseconds following the initial contact. There exist exceptions to this, however they are few and the present work is mainly concerned with the more common situation in which this is true. The short time scale has important implications to both the fluid and solid mechanical aspects of the impact process. In the present section a qualitative discussion of the initial impact behaviour is given. The theoretical and mathematical background to this discussion can be found in Lesser (1981) and Lesser and Field (1983a and b).

The first case considered is that of a spherically shaped liquid drop impacting a rigid or immovable surface. Later we show how the same concepts and methods can be applied to the more general situation of an arbitrary contact geometry and a non-rigid solid. The primary fact that allows us to build an understanding of the impact mechanics is that what are considered relatively high impact speeds, e.g. three or four hundred m s^{-1} are still relatively small compared to the speed of longitudinal waves in typical liquids such as water, with speeds in excess of 1500 m s^{-1} . This means that

there is ample time for the initial compression wave to sweep out over the impacting liquid mass before most of the liquid has an opportunity to undergo any extensive change of shape. The important exception to this is the region near the spreading contact boundary. This region is compressed by collision; however the information that a collision has occurred is carried by a compression wave, so that the drop is divided into two regions in the first stage of contact. The geometry of the situation (figure 1) is such that the contact boundary at first expands over the solid surface with a speed exceeding the wave speed in the liquid. By the classical Huygens construction (see Lesser 1981 and figure 2a) this fact implies that the compression wave spreading into the liquid must be attached to the edge contact point. However for a convex surface such as possessed by a spherical drop, the geometry of the situation dictates that the contact edge speed will decrease until it falls below the compression wave speed. When this occurs the contact signal moves up the free drop surface (figure 2), and the liquid in the vicinity of the free surface is then able to expand so as to meet the ambient conditions of pressure in the vicinity of the surface. Thus compressed liquid undergoes an expansion and "jets" out from the compressed edge region.

A variety of factors complicate the description given above. The most important is that the wave speed is dependent on the amount of compression or strength of the wave, i.e. the wave is a "shock". For the collision speed ranges considered here, this point is of particular significance at the contact edge during the period when the shock is about to detach from the surface. Another key factor affecting the shock detachment process is the elastic behaviour of the target. The time to detachment can considerably longer for a soft target than for a rigid one. However, despite these complications the initial collision mechanics can be understood both qualitatively and quantitatively in terms of essentially geometrical acoustic considerations (Lesser 1981, Lesser and Field 1983b).

A method of visualising the parameter dependencies which we feel to be particularly useful is to examine the coordinate plane M_i and M_e (figure 3). M_i is the ratio of impact speed to ambient liquid sound speed $= U_i/C$ and M_e the edge contact Mach number or ratio of edge contact speed to liquid sound speed $= U_e/C$. In this representation the state at the contact edge for a curved impacting drop is given by the straight line labelled 1, where M infinite corresponds to the initial normal impact. The $M_i = M_e \tan \beta$ relation is of course only meaningful during the period before detachment, since after detachment the free surface near the edge "jets" out in order for the compressed liquid to adjust its density to external conditions. However, even in this region, for reasons given below, we feel this parametric repre-

sentation to be useful.

In a collision where the contact point is moving out on the wetted surface in advance of the wave speed, as was first pointed out by Bowden and Field (1964), the free edge of the liquid is in a zone still unaffected by the impact. Hence in the neighbourhood of the moving contact point the dynamic state of the liquid is given by a local application of the laws of mass and momentum conservation, due account being taken of the presence of the free surface. Thus in this region of time and space the problem possesses a locally similar solution. It is important to realize, Lesser (1981), that the solution so obtained at the contact point is in fact exact and would be used as a boundary condition in any complete analytical solution of the problem. As soon as we leave the vicinity of this point, the past history and global geometry of the interaction influences the solution, however at the contact point the pressure, density and liquid velocity are the same for the impact of a curved front and for a wedge with the same angle between the solid and liquid surface. This means that as long as the contact point is moving supersonically we can denote the conditions at the contact point by a point in the M_e - M_i plane which moves along a line parallel to the M_e axis, the M_e value being the impact Mach number relative to the sound speed in the liquid. From figure 3, it can be seen that in this plot the angle between the M_e axis and a line drawn to the current state point of the contact edge has the same angle as the free drop edge has with the solid.

As shown in Heymann (1969) and Lesser (1981) the attached shock solution at the contact edge is not possible for all values of M_e and M_i or equivalently β and M_i . The equation for the pressure under such a wave system as derived by Lesser (see Lesser 1981, equation 3.20) is given by:-

$$\begin{aligned} \bar{p}^2 M_e^2 F(M_i \bar{p}) - (\bar{p} - M_i)^2 - M_e^2 - \bar{Y}^2 \bar{p}^2 (M_e^2 + M_i^2) \\ + 2 \bar{Y} \bar{p} (M_e^2 + M_i^2 - M_i \bar{p}) = 0, \end{aligned} \quad (1)$$

$$F(\xi) = (1 - (1 + K\xi)^{-1/K})/\xi$$

$$\bar{Y} = \rho_o CY; \quad Y = v_w/p; \quad \bar{p} = p/\rho_o C U_i$$

where p is the wall pressure normalized by the so-called "water-hammer" pressure, Y and \bar{Y} are the admittance and normalized admittance respectively, K is a constant with a value of ca. 7 for water, and v_w is the wall particle velocity. Since $p \gg p_o$ the distinction between $p - p_o$ and p is ignored. The subscript o denotes an initial value for the property concerned. Relevant solutions for this equation only exist for the region indicated in figure 3. When the contact point's motion slows sufficiently, the shock system must move away from the wall and up the free edge. The pressure at the wall maxi-

mizes at this stage to about three times the "water-hammer" pressure and then is relieved by the detachment of the shock system. The pressure relief process is accompanied by a lateral expansion of the liquid or jetting motion, which because of the high pressures developed under the attached shock system can be expected under suitable conditions to move with a speed substantially higher than the initial impact speed.

Recent theoretical considerations (Lesser and Field 1983b) indicate that the liquid motion near the point of edge shock detachment is normal to the free surface. This implies that the spalled liquid drops are directed at an angle of β_c with respect to the normal of the target surface towards that surface. This leads to the situation depicted in figure 4. Note the way the particle trajectories cross. The particles which on rebound travel closest to the target surface are those which are ejected at a later stage. This picture of jetting is contrary to what has often been described in the drop impact literature (even by the present authors). However, careful study of our photographic evidence and of plots of computer simulations (Rosenblatt, Ito and Eggum 1979) support the view that the jetting motion is initially towards the target surface rather than tangent to it. The relief waves moving into the drop soon bring the high pressure phase of the process to an end, with the additional development, which can be observed in the experiments of Camus (1971), that the crossing of the relief waves produce sufficient tensile stresses to initiate cavitation of the liquid.

The qualitative aspects of the above picture has to some extent been substantiated by experimental evidence. One problem has been the fact that the circular damage zone and the observed initiation of "jetting" seems to occur at a larger angle (hence later in the collision process) between liquid and solid surfaces than predicted by the theory summarized above (Hancox and Brunton 1966, Rickerby 1977, Adler 1979c). The numerical investigations of Rosenblatt et al (1979) have also led to larger angles for the commencement of jetting for impact against an idealized rigid target. Lesser (1981) showed that the introduction of a surface admittance parameter into the theory (i.e. treating a non-rigid target) permits the shock to remain attached to the contact point until a larger angle is reached. In addition, it was pointed out that the artificial viscosity method used by Rosenblatt requires a relatively greater length of time for the shock system to form, hence effectively stretching the time scales of the problem. This means that the numerical solution gives the longer time to shock release as an artifact and is thus not an explanation of the experimental observations.

The major difficulty with the experimental observations is that for practical drop sizes and impact velocities the escape angle and jet initia-

tion are extremely difficult to observe. Thus it seemed desirable to design an experiment which would isolate the essential features of the collision process noted above. The technique for doing this involves the use of gelatine wedges which can be preformed into desired shapes and impacted with a moving target. The experimental details are given below. However, before presenting them it is useful to examine a theoretical model of the collision of such a wedge with a solid surface. This theory was reported in preliminary form in Lesser and Field (1974).

Figure 5 shows such wedge-shaped liquid masses impacting rigid targets. The results of such impacts depend on the wedge angle, the impact speed and the wave speed in the liquid. As noted above, what is usually regarded as a high speed impact will in many cases of practical interest be quite small compared to the compressional wave speeds of most liquids. This permits us to use a perturbation procedure based on the fact that the waves spread out over the wedge much faster than the wedge distorts. Using such a perturbation method it is possible to calculate all the quantities of interest, including the lateral liquid motion. In fact such motion only occurs for a given impact speed when the wedge angle is such that the contact point moves subsonically. The wave geometrical reasons for this are illustrated in figure 5b. Such calculations compared well with numerical work carried out by Glenn (1974) for the impact of liquid cylinders.

Thus a major experimental objective is to study such wedge impacts with angles bracketing the shock escape angle. In addition, it is shown that the experimental observations give important clues for the complex effects produced by the details of the surface geometry.

Figures 6-8 give the results of calculations for the impact of liquid wedges by rigid targets (Field, Lesser and Davies 1979, Lesser 1981)

Figure 6 gives the non-dimensional edge pressure p as a function of M_i for various wedge angles β . Note that the values are always above the "water-hammer" pressure $p = 1$. At high M_i the curves run together, while at low M_i each curve has a minimum M_i (where a line such as OA cuts the $Y = 0$ curve on figure 3) and at this point p is a maximum. These maxima are at values of p ca. 3. The same data is plotted in absolute terms taking $C = 1500 \text{ m s}^{-1}$ (figure 7). OA is the "water-hammer" pressure curve. If, for example, we consider a wedge with $\beta = 40^\circ$, then U_i has to exceed 168 m s^{-1} for the configuration of figure 1 to apply. At this stage the edge pressure equals 2.7 times the "water-hammer" pressure or 0.73GPa in absolute terms. High edge pressures will, of course, always result with a spherical drop since the initial value of β is 0° .

Figure 8 gives the various velocities associated with the contact region

of figure 1b. For M_i values up to 0.5, the non-dimensional wave (shock) speed C increases reaching ca. 2.8 at $M_i = 0.5$. The non-dimensional particle velocity behind the shock front (equal to u_w/C) is small; its curve is multiplied by 100. Note that the high edge pressures cause both C and M_w to increase in the vicinity of low M_i .

2.3 EXPERIMENTAL

The idea of using disc-shaped bubbles or drops for cavitation or liquid impact studies was first suggested by Brunton (1967). The technique was further developed in subsequent research (Brunton and Camus 1970a and b, Camus 1971, Rochester and Brunton 1974a and b, Rochester 1979). In the case of drop impact, a small quantity of liquid was placed between two transparent plates separated by a small distance; surface tension pulled the liquid into a curved profile. Impact was achieved by projecting a third plate between the two spaced plates. High-speed photography, using either a Beckman and Whitley (model 189) rotating mirror camera or single-shot schlieren photography, was used to record the impact events on a micro-second time scale. To obtain synchronization with the rotating mirror camera, the impact plate was accelerated with an explosive detonator; the arrangements used achieved velocities of typically 100 m s^{-1} (Brunton and Camus 1970a and b, Camus 1971). The great advantage of this two-dimensional work was that it allowed processes occurring inside an impacted drop to be observed in detail without the refraction problems inherent with spherical drops.

An example from Caums's work (1971), for a 70 m s^{-1} impact is shown in figure 9. The "sequence" is in fact a composite of three different experiments since the single-shot schlieren approach was used to show the stressed regions and shock wave more clearly. Frame a is from the very early stage of impact where both solid and liquid are highly compressed in the contact region, and there is no jetting. In b a shock has detached and is moving up through the drop and jetting has started, though high pressure regions, labelled p, still persist in the liquid. Finally, in c the shock is about to reflect at the upper surface and the jetting is more advanced. In view of our earlier comments on the motion of the liquid in the jet, it is interesting to note that the spray is angled upwards rather than tangent to the target surface. Note also that in frames b and c the interface between liquid and solid appears textured (labelled B): other sequences (Camus 1971) have confirmed that the effect is due to cavities which form during impact and which may eventually collapse violently and cause damage. Cavities can

also develop when the primary shock reflects at the upper liquid/air interface; however, these are well away from the solid and do not contribute to the damage process.

In their extension of this work (Rochester and Brunton 1974a and b, 1979, Rochester 1979) fired an instrumented bullet (simulated target) at a two-dimensional drop and the impact pressure distribution was measured. The results showed that, although the "water-hammer" pressure occurred at the centre, there were off-axis ressurees of even greater magnitude and of roughly the size predicted by the theoretical work of Heymann (1969), Lesser (1981) and above (section two).

A disadvantage of impact with a drop, both from the viewpoints of analysis and experimental interpretation, is that there is a constantly changing angle between the drop boundary and the solid (angle in figure 1). This is overcome by using wedges of liquid which have a constant, prechosen β .

In the present experiments, two-dimensional wedges and other geometries were prepared by first mixing 12% by weight of gelatine with water, allowing it to set into a thin sheet and then cutting into the required shape. Previous work in the laboratory (Rickerby 1977, Field, Gorham and Rickerby 1979) had used a similar approach to produce large spherical drops of liquid of up to 6mm diameter, and had shown that the flow properties were not significantly different to that of pure water once impact velocities exceeded a few metres per second.

The water/gelatine sheets were made by casting into a 200 x 200 x 3mm vertical mould to reduce evaporation. Both liquid and mould were at 300 K. Each of the large mould faces had been lightly greased and covered with a thin plastic film. After slow cooling, to reduce shrinkage, the mould was disassembled and the sheets placed horizontally. The layers, with plastic sheets attached, could be kept for several days. After some practice it was possible to cut out wedges with flat and smooth edges.

In early experiments, the chosen liquid/gelatine layer was placed between two thick, spaced glass blocks and mounted vertically in a frame (Field et al 1979). The impacting solid was a steel or phosphor bronze plate which was inserted between the glass plates to within 5mm of the liquid wedge and with its rear surface projecting out from the blocks. The steel plate could be moved at velocities up to ca. 100 m s^{-1} from a 25mm diameter bore gas gun. The steel plate triggered an Imacon framing image converter camera by intersecting a laser light beam just before impact. A schematic diagram of the apparatus is shown in figure 10. A description of the basic gas gun design can be found in Hutchings and Winter (1975). Schlieren optics were

used to make the stress waves visible.

The basic problem with impact velocities of only up to ca. 100 m s^{-1} is that the angle β for supersonic behaviour has to be less than ca. 3 degrees. Producing controlled impacts with such small angles is difficult, and there are also problems in taking measurements from such sequences. Ideally velocities of a few hundred meters per second would be better since this would increase the angle β . A second experimental arrangement was therefore tried with a two-dimensional rectangular bore gas gun used to project the striker directly between the glass plates. This arrangement eliminated the need for separate strikers and projectiles as used in the first experiment. Having a rectangular bore gun barrel and incorporating the sabot and striker S into one projectile gave sufficient control to be able to shoot the striker accurately between the glass plates and make it possible to achieve velocities of up to ca. 300 m s^{-1} . This increased the angle , for a rigid target, to ca. 10 degrees. The Schlieren optics were improved by replacing the lenses of the former system with mirrors.

2.4 Results

(a) Wedge Impact

Figure 11 illustrates the two situations for wedge impact. For the wedge surface OA, the contact point moves supersonically with the shock attached to the contact point, the shock envelope elongated in the x-direction and no jetting motion. For the wedge surface O'A', the primary shock should be part of a circle, with the shock ahead of the contact point and a jet forming.

Figures 12-14 are all for an impact velocity of 150 m s^{-1} (ie. $M_i = 0.1$) and with wedge angles β which are below, close to and above the critical β_c respectively. For $M_i = 0.1$, β_c on linear theory ($U_e > C$) is 5.7° and on the full non-linear theory ($U_e > C + u_w$, where u_w is the particle velocity in the liquid near the contact point) is 3.7° . In figure 12, with a β value less than β_c , a strong shock envelope develops which expands much faster in the x-direction than vertically. No jet can be detected in the air wedge though a high speed jet, labelled J, of velocity ca. 1300 m s^{-1} forms when the shock envelope reflects at the right hand edge. Jet formation at the right hand edge is expected and is discussed in detail in the next section. Note that the reflected shock wave, S, now a wave of tension, causes cavitation in the liquid which is evident as the dark region labelled T.

Figure 13 is an example where β is close to the critical value. In fact, the front of the slider is slightly radiused so that β is ca. 4° at the start of impact increasing to ca. 6° at the end. Note that the contact edge is clearly supersonic in frames (a) to (c) and that during this stage the shock front at the contact point steepens. The shock front should be perpendicular to the liquid edge when it overtakes the contact point. This happens between frames (c) and (d). Careful examination of frame (d) suggests that jet formation may have started, but certainly from frame (e) onwards there is clear evidence of jetting (see arrows). The jet has a velocity of ca. 2500 m s^{-1} .

In Figure 14, β is greater than β_c . The primary wave is now part of a circle, it moves ahead of the contact point and a jet can be detected in the air wedge from frame d onwards. The jet velocity in this case was ca. 1000 m s^{-1} .

Measurements were made of the contact angle, β , and the inclination of the shock, α , to the slider impact face. The results are given in Table 5 together with Lesser's theoretical predictions for α .

(b) Target admittance

According to the theoretical work of Lesser (1981), the greater the target admittance (inverse of impedance), the larger the critical angle β_c before flow results. In the experiments described above with steel strikes, the value for β_c was shown to be $5 \pm 1^\circ$. A series of experiments covering a wide range of β 's has also been made with polymethylmethacrylate (PMMA) strikers which have a much larger admittance. Figure 15 gives an example near the critical β_c for an impact at 300 m s^{-1} ($M_i = 0.2$). The PMMA surface is slightly curved. In frames (a) to (d), the contact moves supersonically and the shock front steepens. In frame (e) onwards, the shock passes ahead of the contact point and jetting commences. Since PMMA is transparent, shocks can also be seen in it. From this and similar experiments, we have measured β_c to be $10 \pm 1^\circ$ for impacts with PMMA at $M_i = 0.2$. The experimentally determined values of β_c for impacts with steel and PMMA targets are compared with the theoretically predicted values in the discussion section.

(c) The double-angled wedge

Experiments have also been made with the double wedge geometry shown schematically in figure 16. The angle β_0 is kept below the critical angle so that the contact point moves supersonically along OA. The angle β can take values from β_c up to 90° . The interest in this geometry is that Lesser and Finnstrom (1984) have recently completed a linear analysis which predicts the velocity of jetting. Figure 17 illustrates the situation when the target surface has passed point B. It shows the position of the shock envelope, the corner waves from the points O and A, the motion of the side wall at the left and the onset of jetting in the wedge. A preliminary account of the analysis is included in Field et al (1983).

Figures 12 and 13 are effectively examples of double-angled wedges with $\beta = 90^\circ$. Figure 18 is an example with $\beta = 45^\circ$. A jet starts to form in frame (e). Its velocity averaged between frames (e) and (g) is $1100 \pm 100 \text{ m s}^{-1}$. The measured jet velocities are compared with the theoretical predictions in the discussions section.

2.5 Discussion

The present set of experiments clearly show that the main features following impact are a contact edge moving out on the target surface with supersonic velocity, an attached shock system and a confined free edge. This

latter feature of the early contact period means that the free drop surface, i.e. the surface which has not touched the target, is as yet totally unaffected by the impact. A particularly important consequence is that at this stage there is no jetting. These observations apply if the angle between the liquid free edge and the target surface is smaller than the critical angle for a given impact velocity. Thus the early stages of impact are best understood in terms of non-steady compressible flow, and in fact for most impact speeds normally encountered in practice a large number of the observed events can be understood in terms of a linearized or acoustic version of the theory.

When the contact angle exceeds the critical angle for a given impact speed, the wetted surface spreads out slower than the liquid wave speed and as a consequence the shock travels up the free edge. The liquid between the surface and advancing shock feels the effects of the impact, hence it is compressed and then expands as relief waves sweep in from the exposed edge. This expansion accelerates the fluid leading to the jet-like behaviour shown in the sequences of Figures 9, 13, 14, 15, 18, we approach even larger angles, as might be expected from an impacting cylinder, we observe a relatively slow smooth deformation of the liquid's free surface.

(a) Angle for jetting

The Bowden and Field (1964) model, based on linear acoustic reasoning, suggested that jetting would start at an angle $\beta_c = \sin^{-1} M_i$ for impact with a rigid target. The shock detachment angle for a rigid target as computed by Lesser (1981), Heymann (1969) gives an even smaller angle, e.g. for M_i 0.05, $\beta_c = 2.25^\circ$ as opposed to $\sin^{-1} M_i = 2.87^\circ$. Experimental studies have invariably found larger angles than predicted by these theories. For example, Camus (1971), Brunton & Camus (1974a and b) recorded angles between 10° and 20° with an average of 11° in the velocity range 30 to 100 m s⁻¹. Hancox & Brunton (1966) from damage studies on PMMA with their wheel-and-jet apparatus deduced an angle of ca. 17° for impact at 60 m s⁻¹.

Various ideas have been advanced to explain this. An early suggestion by Hancox & Bruton (1966) that viscosity delays the onset of jetting is not convincing considering the velocities and pressures involved. Recently one of us (Lesser 1981) suggested that the deformability of the target has a major effect on increasing β_c , thus refuting an earlier suggestion by Engel (1972) that target admittance would have only a minor effect. Another factor likely to affect experimental observations is aerodynamic distortion of the contact surface of the drop to a greater effective radius. Finally, if the

flow angle is deduced indirectly from damage studies the result will be an overestimate. The reasons for this are that when the jet first forms it may be too thin to have damage potential and further it needs to act on a perturbed surface. As Blowers (1969) has shown, the Rayleigh surface wave which gives the main component of the surface displacements takes some time to reach a peak after the supersonic contact phase ceases.

The present experiments with steel and PMMA targets (section 3) were designed to test Lesser's hypothesis. The results give clear evidence for the critical angle being greater for a material with greater admittance (ie. PMMA). At this point it is useful to re-emphasise the precise conditions for which Lesser's (1981) analysis holds. Lesser's theory treats the cases of triple supersonic impact, where the contact edge moves out ahead of all wave speeds in the impacting materials, and impact against a "fictitious" constant admittance material, ie. a given pressure-velocity relation for the material in the contact region. When the contact edge slows down below the fastest wave speed in the solid, the triple supersonic condition is violated and the theory cannot be used to predict the critical condition at which the edge shock in the liquid leaves the surface of the solid. If the solid's wave speeds were indeed smaller than the liquid's, the "effective" admittance parameter in Lesser's paper could be used to predict the critical condition. In spite of this restriction, it is of interest to see what the critical condition would be (see Table I) if the ordinary acoustic admittance of the material is used for the prediction, ie. it is assumed that a local admittance characterises the target material.

From Table I we see that for a steel or phosphor-bronze (\bar{Y} ca. 0.033) target impacting at $M_i = 0.1$ β_c is predicted to be ca. 3.8° . Experimentally (see section 4b), a value of $5 \pm 1^\circ$ was found. For a PMMA target (\bar{Y} ca. 0.55) impacting at M_i ca. 0.2, β_c is predicted to be 8.3° (ie. two degrees greater than the value of 6.3° for a steel target). The experimental value for β_c was $10 \pm 1^\circ$. The present experimental evidence confirms Lesser's view that target admittance has a major effect on the angle at which jetting starts. However, the experimental value of β_c appears to be slightly greater than those predicted in Table I. A more detailed analysis would have to take into account surface motion of the target ahead of the expanding edge, due to the larger wave velocities in the target. This would have the effect of retarding the escape of the edge, thus giving a greater β_c .

(b) Jet velocity

Jetting takes place when the shock advances ahead of the contact point and moves up the free face of the drop. Providing β is $< \beta_c$ the jet velocity is higher for smaller values of β . This point also emerged from the earlier work of Camus (1971) on liquid impact and related studies of similar geometry which also produced high speed jets such as the collapse of shaped-charges (Birkhoff, MacDougall, Pugh and Taylor, 1948), high velocity collisions (Walsh, Shreffler and Willig, 1953, Harlow and Pracht, 1966) and explosive welding (Bahrani, Black and Crosland, 1967).

The material which forms the jet initially moves perpendicularly to the drop surface, and hence towards the target surface. Since the material is in the form of small particles (a spray) the particles can cross each others' path lines. This leads to the situation shown schematically in figure 4. Careful examination of the photographic evidence and plots of computer simulation (Rosenblatt et al, 1979) supports this view.

Our photographic work on wedge impact has also shown that an abrupt change from an angle of $< \beta_c$ to a particular β drives a faster jet than impact with a wedge of angle β . The jets also form quickly once the critical conditions are achieved and this shows that we are dealing with a threshold governed event that is very sensitive to the particular impact geometry. No complete theory for predicting jet velocities during liquid drop impact yet exists, though Lesser and Finnstrom (see Field et al, 1983, for a preliminary account) have analysed the double wedge geometry shown schematically in figure 17. This figure gives the situation they analysed when the target surface has passed point A. The first step was to determine the pressure in region 2 which gives the boundary condition along the corner wavefronts. After calculation of the pressures in region 1, the pressure gradient normal to AB was used to find the velocity of the liquid surface as it is forced from its original profile to start a jet.

Selected results are shown in Figure 19. In the cases illustrated M_i was 0.1 corresponding to an impact velocity of 150 m s^{-1} . At this velocity the critical angle is 5.71° (linear theory). The x-component of the velocities, V_x , are given non-dimensionally in terms of C . R is also non-dimensional with the values 0 and 1 corresponding to the points A and B on the wedge surface (see Figure 17). Each figure contains three curves for different values of β_0 . The following general trend emerges: for a given β , the jet velocity increases as β_0 approaches the critical angle. The increase is particularly pronounced as β_0 is approached (note the changes as β_0 varies

from 5.3° to 5.5° to 5.7°).

It is important to appreciate that the initial movement of the free surface reached by the shock is at right angles to AB. One consequence of this is that for angles of β , other than 90° , the moving liquid approaches the target surface at an angle and rebounds from it. This is certainly consistent with experimental observations which show the jet lifting up from the target surface. For small values of β , the interaction between rebounding and incident liquid will be complex and the jet will quickly break up into a spray.

The results of Figure 19 for the x-component of the velocity do not give the jet velocity directly. This has to be obtained by integration. The surface begins to move when the shock wave reaches it (point B, and R value equal to 1.0). It will move with increased velocity as the target surface approaches and its R value decreases to 0. The area under the velocity/R curve is the mean velocity which equals the jet velocity, V_j . Tables 2-4 summarise the predicted jet velocities for a range of configurations. Figure 18 is an example of a double wedge with $\beta = 45^\circ$ and β_0 just sub-critical. A jet is formed in frame e. Its velocity, averaged between frames 2 and 8, is $600 \pm 100 \text{ m s}^{-1}$. This agrees reasonably with the theoretical predictions (Table 2). It is difficult to be more precise since the jet velocity depends so critically on the value of β_0 in the range 5.3° to 5.7° .

We are also able to compare the results from Figures 12 and 18 with the theoretical predictions. Here the wedge angles were sub-critical and a jet only formed when the shock interacted with the right-hand boundary (i.e. $\beta = 90^\circ$). In Figure 12, β_0 was ca. 3° and a jet velocity of ca. 1300 m s^{-1} was observed. In Figure 13, β_0 went through the critical angle and a jet velocity of ca. 2500 m s^{-1} was recorded. Comparison with the data of Table 3 shows that the second of these results is in excellent agreement. However, the jet velocity recorded for the 3° wedge is higher than predicted. The explanation for this is that as the right-hand boundary is approached, the wedge angle increases. If, for example, it is curved up to ca. 5° , this would sharpen the shock and give the higher jet velocity. It emphasises how critical the pressures and jet velocities are to small changes in contact angle.

(c) Cavitation in the drop

Another interesting and important consequence of the jetting behaviour is that it can result in cavitation of the liquid in the vicinity

of the target surface (figure 9). The production of such a cavitating region was observed, though not explained, by Camus (1971). It can clearly be understood in terms of the wave picture. In figure 20, we show a diagram for a wedge geometry but the argument would apply equally well to other liquid shapes. The expansion waves sweep in from the free edge and cross. For an acoustic or linear model, the magnitude of each pressure relief wave will be of the same order as the initial compression wave since the relief waves return and the liquid at each edge to ambient conditions. The effects of the waves superpose where they cross, bringing the liquid into a negative pressure or tensile stress state causing cavitation. From the point of view of damage, the cavitation can be important, since the collapse of the liquid cavities near a solid boundary produce both shocks and microjets and this adds to the pressures already present. The effect is likely to be most important with ductile materials near the threshold conditions for damage. This is because the main and the additional peaks add to give greater compressive and hence greater shear stresses. However, with brittle materials, failure is due to tensile stresses around the contact area and the material usually recovers from the compressive stresses (Bowden and Field, 1964) A local additional high pressure in a region already subjected to compression is unlikely to produce tensile stresses. Hence the cavitation damage mechanism is likely to be most significant with materials which fail by compression or shear.

(d) Damage patterns

The mechanisms that lead to the particular damage pattern observed in a single event clearly depend on relatively small changes in the liquid and solid geometry. It remains to explain how such highly characteristic events can cause the relatively ordered patterns observed with multiple collisions against particular material targets. Our experiments and the wave picture of the initial collision suggest various possible mechanisms which could explain some of the observed regularities. Repeated impacts, for example, on a single site frequently produce a central pit, and in extreme cases (often seen with steam turbine blades in an advanced state of erosion) the pits can extend as deep channels into the material. Figure 21 shows schematically a feasible sequence of events for repeated impact on a ductile material. Note that the diagram is meant to depict four stages in the development of damage and not necessarily the behaviour of four successive impacts.

State (a) is concerned with the formation of a surface depression. As the

hole deepens and the drop fills the depression, state (b) onwards, the duration of compressible behaviour is greatly extended. A particularly important stage occurs in figure 21(c) when the impact centre is below the surface of the oncoming drop. The angle between the free surface and target is less than the critical angle associated with shock detachment, and this leads to the strong shock associated with the pre-escape condition. The difference from the expanding outer contact surface is that the shocks focus on the impact centre, leading to extremely high pressures when the contact edges reach this point. Once the central part of the depression deepens, figure 21(d), the angle between the free surface and the target surface is now above the critical escape angle, the shock detaches and there is no shock focusing. However, jets form and they will collide and impact on the base of the hole. The pits on eroded steam turbine blades can have a depth several times the drop diameter. Eventually the "cushioning" effect of the liquid and air trapped in the pits prevents their further development.

Figure 22 shows the results of ten liquid impacts on a copper target by a liquid jet fired at 960 m s^{-1} from a 0.8 mm orifice nozzle. Other work (Field, van der Zwaag and Townsend, 1983) has shown that under these conditions the jet impact is equivalent to impact by a 5 mm diameter drop. The crater shape developed through the four stages depicted schematically in figure 21.

(e) Drop oblateness

Another important factor which emerges from liquid impact theory is that of drop oblateness. If a drop impacts in the configuration depicted in figure 23, it will be more damaging than if in spherical form. This is simply because the compressible, high pressure, regime is sustained for longer. Similarly, it is possible for target curvature (see for example figure 21(b)) to act in a similar way and delay the escape condition.

(f) Specimen orientation in erosion testing

A variety of techniques have been devised for studies of liquid-solid impact. Historically, the first was the wheel-and-jet method which has been used in various forms since the 1920's. In a typical configuration, specimens are attached to the edge of a disc so that they protrude radially. As the disc rotates, the specimens impact one or more cylindrical jets of liquid. The wheel and jets are usually in a chamber which is pumped to as low a pressure as possible to reduce aerodynamic distortion of the jets. Anyone who has used such an apparatus will know that specimen alignment is

critical if reproducible data is to be obtained. The reason for this is apparent from the theory developed above. If the specimen is perfectly aligned with the face of the specimen parallel to the axis of the jet, initial contact is along a line $00'$ (see figure 24a and b). There is then compressible behaviour with no jetting until the contact area has a width $2x$. For a brittle material, tensile failure only occurs outside this central region. This unfractured central strip corresponds to the circular region surrounded by circumferential cracks for spherical drop impact. However, if the specimen is misaligned through an angle β (see figure 24), the contact is not instantaneous along $00'$, but moves upwards with a velocity which is supersonic for sufficiently small β and subsonic for large β . In the first of the cases, high edge pressure will be generated at the contact point but there will be no flow, while for a large β a high velocity jet will move upwards. The three cases of perfect alignment, small β and large β are very different. A key point is that for the velocity used in this test the angle β which determines whether the contact point moves supersonically along $00'$ or not is a few degrees at most. Hancox and Brunton (1966) give examples of damaged PMMA specimens eroded in this test, one for perfect alignment and one inclined with $\beta = 9^\circ$. The first specimen shows an undamaged central strip with cracks and flow damage outside this. The angled specimen exhibits arc-like cracks and erosion cutting across the central axis. Very different erosion rates were also recorded.

(g) Other situations

The geometries discussed in this paper have relevance to explosive welding and jet formation from a shaped-charge. In both cases, the question of whether or not the contact point is supersonic or not is critical for jet formation. We are at present applying the techniques discussed in this paper to these and other problems.

6. Conclusions

The paper has summarized the main results of recent theoretical work on liquid impact and has shown that wave effects such as shock detachment, focusing and crossing can provide explanations of many of the features observed in liquid erosion tests and experiments. The coupling of this analytic work with the gelatine wedge technique described in this paper has great potential for solving problems of liquid impact. The power of the technique is that it allows us to extract the essential features of processes and to conveniently study the influence of otherwise very difficult

geometries. The combination of strong shocks, free surfaces and solid body motion is a complicated one, and much remains to be done before we can be sure that we have even observed all the possible phenomena. We feel that the technique developed here will provide considerable assistance in future studies.

- Adler W.F. 1979a ed. "Erosion, prevention and useful applications". STP 664, Am. Soc. Test. Mater. Philadelphia, U.S.A. pp 1 - 643
- Adler W.F. 1979b in "Erosion" ed. C.M. Preece, Academic Press, New York, 127
- Adler W.F. 1979c Proc. 5th Int. Conf. on Erosion by Liquid and Solid Impact (ed. J.E. Field) Cavendish Laboratory, Cambridge, U.K. Paper 13
- Birkhoff G., Macdougall D.P., Pugh E.M. and Taylor G.I., J. Appl. Phys. 563
- Blowers R.M. 1969, J. Inst. Math. Applic. 5, 167
- Bowden F.P. 1966 Organiser Roy. Soc. Discussion meeting "Deformation of solids by the impact of liquids". Phil. Trans. Roy. Soc. Lond A260, pp 73 - 315
- Bowden F.P. and Field J.E. 1964 Proc. Roy. Soc. Lond A282, 331
- British Hydraulic Research Association 1972, 1974, 1976, 1978, 1980, 1982 Proc. Int. Symp. Jet Cutting Technology, BIRA, Cranfield, U.K.
- Brunton J.H. 1967 Proc. 2nd Int. Conf. on Rain Erosion and Associated Phenomena (eds. A.A. Fyall and R.B. King) Meersburg, W. Germany - p. 535
- Brunton J.H. and Camus J-J 1970a. Proc. 3rd Int. Conf. on Rain Erosion and Associated Phenomena (eds. A.A. Fyall and R.B. King), Meersburg, W. Germany, p.327 R.A.F. Farnborough, U.K.
- Brunton J.H. and Camus J-J 1970b. Proc. 9th Int. Conf. High-Speed Photog. (eds. W.G. Hyzer and W.G. Chase), SMPTE, New York, p. 444
- Brunton J.H. and Rochester M.C. 1979. In "Erosion" ed. C.M. Preece Academic Press, New York, p. 185
- Camus J-J 1971 University of Cambridge, U.K. PhD Thesis
- Engel O.G. 1972. J. Appl. Phys. 44, 692
- Field J.E. 1979 ed. Proc. 5th Int. Conf. on Erosion by Liquid and Solid Impact. Cavendish Laboratory, Cambridge, U.K.
- Field J.E., Gorham D.A. and Rickerby D.G. 1979 In "Erosion; prevention and useful applications" (ed. W.F. Adler) STP 664. Am. Soc. Test. Mater. Philadelphia, U.S.A. p. 298
- Field J.E., Lesser M.B. and Davies P.N.H. 1979 Proc. 5th Int. Conf. on Erosion by Liquid and Solid Impact (ed. J.E. Field) Cavendish Laboratory, Cambridge, U.K. Paper 2
- Field J.E. and Corney N.S. 1983 eds. 6th Int. Conf. on Erosion by Liquid and Solid Impact. Cavendish Laboratory, Cambridge, U.K.
- Field J.E., Dear J.P., Davies P.N.H. and Finnström M. 1983 Proc. 6th Int. Conf. on Erosion by Liquid and Solid Impact (eds. J.E. Field and N.S. Corney) Cavendish Laboratory, Cambridge, U.K. Paper 19
- Field J.E., van der Zwaag S. and Townsend D. 1983 Proc. 6th Int. Conf. on Erosion by Liquid and Solid Impact (eds. J.E. Field and N.S. Corney) Cavendish Laboratory, Cambridge, U.K. Paper 21
- Fyall A.A. 1967 Proc. 2nd Int. Conf. on Rain Erosion and Associated Phenomena (eds. A.A. Fyall and R.B. King), Meersburg, W. Germany - p. 563

- Glenn L.A. 1974 Z. Angew. Math. Phys. 25, 383
- Hancox N.L. and Brunton J.H. 1966 Phil. Trans. Roy. Soc. Lond A260, 121
- Harlow F.H. and Pracht W.E. 1966 Physics of Fluids, 9, 1951
- Heymann F.J. 1969 J. Appl. Phys. 40, 5113
- Hutchings I.M. and Winter R.E. 1975 J. Phys. E. Sci. Instrum. 8, 84
- Jenkins D.C. and Booker J.D. 1960 In "Aerodynamic Capture of Particles" ed. E.G. Richardson, Pergamon, Oxford pp 97
- Lesser M.B. 1981 Proc. Roy. Soc. Lond A 377, 289
- Lesser M.B. and Field J.E. 1974 Proc. 4th Int. Conf. Rain Erosion and Associated Phenomena (eds. A.A. Fyall and R.B. King) Meersburg, W. Germany, p. 235
- Lesser M.B. and Field J.E. 1983a, Ann. Rev. Fluid Mech. 15, 97
- Lesser M.B. and Field J.E. 1983b Proc. 6th Int. Conf. on Erosion by Liquid and Solid Impact (eds. J.E. Field and N.S. Corney) Cavendish Laboratory, Cambridge, U.K. Paper 17
- Lesser M.B. and Finnström M. 1984 University of Luleå, Sweden. Private Communication
- Freece C.M. 1979 ed. "Treatise on Materials Science and Technology Vol. 16 Erosion". New York, Academic Press
- Rochester M.C. 1979 PhD thesis, University of Cambridge, U.K.
- Rochester M.C. and Brunton J.H. 1974a STP 567, Am. Soc. Test. Mater., Philadelphia, U.S.A. p 128
- Rochester M.C. and Brunton J.H. 1974b 4th Int. Conf. on Rain Erosion and Associated Phenomena (ed. A.A. Fyall and R.B. King) Meersburg, W. Germany, p 371
- Rochester M.C. and Brunton J.H. 1979 Proc. 5th Int. Conf. on Erosion by Liquid and Solid Impact (ed. J.E. Field) Cavendish Laboratory, Cambridge, U.K. Paper 6
- Rosenblatt M., Ito Y.M. and Eggum G.E. 1979 In "Erosion: prevention and useful applications" (ed. W.F. Adler) STP 664 Am. Soc. Test. Mater. Philadelphia, U.S.A. p 227
- Rickerby D.G. 1977 PhD Thesis. University of Cambridge, U.K.
- Walsh J.M., Shreffler R.G. and Willig F.J. 1953 J. Appl. Phys. 24, 349

TABLE 1

Predicted critical angles β_c , and normalised wall pressures \bar{p} for different target materials of normalised admittance \bar{Y} , with respect to water

$U_i/\text{m s}^{-1}$	M_i	Rigid, $\bar{Y} = 0$		$\bar{Y} = 0.033$		$\bar{Y} = 0.55$	
		$\beta_c/^\circ$	\bar{p}	$\beta_c/^\circ$	\bar{p}	$\beta_c/^\circ$	\bar{p}
150	0.10	3.7	3.4	3.8	3.3	4.8	1.0
200	0.13	4.7	3.2	4.9	3.2	6.2	1.2
250	0.17	5.4	2.8	5.6	2.8	7.2	1.2
300	0.20	6.0	2.7	6.3	2.7	8.3	1.2
500	0.31	8.2	2.9	8.6	2.9	12.3	1.2

TABLE 2

Data for $\beta = 45^\circ$ and β_o varied for
 $M_i = 0.1$, where $\beta_c = 5.71^\circ$

$\beta/^\circ$	$\beta_o/^\circ$	Mean V_x/C	Mean $V_x=v_j/m \text{ s}^{-1}$
45	1	0.056	80
45	3	0.086	130
45	5	0.182	270
45	5.3	0.236	350
45	5.5	0.326	490
45	5.7	1.44	2160

TABLE 3

Data for $\beta = 90^\circ$ and β_o varied for
 $M_i = 0.1$, where $\beta_c = 5.71^\circ$

$\beta/^\circ$	$\beta_o/^\circ$	Mean V_x/C	Mean $V_x = V_j/m \text{ s}^{-1}$
90	1	0.102	150
90	3	0.117	180
90	5	0.207	310
90	5.3	0.268	400
90	5.5	0.371	560
90	5.7	1.64	2460

TABLE 4

Data for various β with β_o kept constant
for $M_i = 0.1$, where $\beta_c = 5.71^\circ$

$\beta/^\circ$	$\beta_o/^\circ$	Mean V_x/C	Mean $V_x = V_j/m \text{ s}^{-1}$
10	5.7	0.396	590
20	5.7	0.758	1140
30	5.7	1.07	1610
40	5.7	1.34	2010
50	5.7	1.53	2300
60	5.7	1.66	2490
70	5.7	1.72	2580
80	5.7	1.71	2570
90	5.7	1.64	2460

TABLE 5

Experimental and theoretical values of
 α for different β

Figure	$\beta / ^\circ$	$\alpha_{\text{expt}} / ^\circ$	$\alpha_{\text{theo}} / ^\circ$
12	3	39 ± 1	38°
†	4	61 ± 1	60°
14	$4 \rightarrow 6^*$	$51 \pm 1 \rightarrow 83 \pm 1$	$60^\circ \rightarrow \text{jetting}$

† unpublished figure

* radiused front surface to slider

LIST OF FIGURES

Figure 1(a) Early stage of impact during which the contact edge.

Figure 2(a) Supersonic contact edge illustrating the formation of the shock envelope from many individual wavelets

Figure 2(b) Supersonic contact edge illustrating the wave moves up the free edge of the drop, expansion waves move into the compressed liquid, and jetting commences.

Figure 3. In this representation, a drip impacting at a particular M_i can be represented by line 1. When point A reaches the curves reaches its critical value β_c .

Figure 4. Jet formation; droplets detach in a direction normal to the drop surface and move initially towards the target.

Figure 5. Shock configurations for wedges, with the primary shocks and the corner waves illustrated. In (a), the shocks move ahead of the contact point and the liquid releases forming a jet in the air wedge.

Figure 6. Non-dimensional "edge" pressures versus M_i for various values of β . Note that values of the edge pressure can reach about three times the "water hammer" pressure.

Figure 7. Absolute values of "edge" pressures versus M_i and velocity of impact U_i for various values of β .

Figure 8. Velocities associated with the region in the liquid behind a supersonic contact point.

Figure 9. Impact with a two-dimensional drop at 70 m s^{-1} . Noteing the absence of flow in (a), and the shock structure, high pressure lobes (labelled p) and jetting in (b) and (c). The textured appearance at the interface above B is due to the formation of cavitation bubbles. The drop diameters are ca. 2mm (Camus, 1971).

Figure 10. Top and side views, not to scale, of the impact geometries. W is the water/gelatine wedge, P is the plastic sabot and S the impacting striker. In the initial experiments, S was stationary, and P was fired from a circular bore gun. In the final arrangement, S was projected from a two-dimensional gun, and higher impact velocities with W were achieved.

Figure 11. Impact geometries for a target striking a liquid wedge for (a) supersonic contact with the shock envelope attached to the contact point (b) subsonic contact with the primary shock advancing ahead of the contact point and a jet forming.

Figure 12. Impact with a wedge with β ca. 3° and $M_i = 0.1$. There is a supersonic contact point and no jetting in the wedge. A jet, labelled J, forms only when the shock reaches the boundary. The dark region labelled T, behind the reflected shock S, is due to cavitation. Width of gel 7.5 mm.

Figure 13. Impact with a slightly curved slider so that β varies from 4 to 6° . The shock steepens in frames (a) to (c) and overtakes the contact point between (c) and (d). Jet formation then starts. The jet, labelled in frame (f) has a velocity of ca. 2500 m s^{-1} . Width of gel 8.5 mm.

Figure 14. Impact with the wedge with β ca. 12° , $M_i = 0.1$. The contact point is subsonic and the wave much weaker. A jet, labelled J, appears in the gap between target and liquid. Width of gel 7.5 mm.

Figure 15. Impact with a high admittance plastic target M_i (PMMA) at $M_i = 0.2$. The target is slightly curved. In the frame (f) the shock passes ahead of the contact point and jetting starts. β_c was ca. 10° which was significantly higher than for a rigid target. Width of gel 10 mm.

Figure 16. Impact with a double-angled wedge with $\beta_o < \beta_c$ and variable in the range β_c to 90° .

Figure 17. Situation when the target surface has passed point A and jetting has commenced. The positions of the shock envelope and the corner waves from O and A are shown.

Figure 18. An example of impact at $M_i = 0.1$ with a double-angle wedge with β_o just sub-critical and $\beta = 45^\circ$. The arrows mark the jet which has a velocity of $1100 \pm 100 \text{ m s}^{-1}$ in agreement with theory. Note the corner wave labelled C in frame g. Width of gel 11 mm.

Figure 19. The x-component of the flow velocity plotted nondimensionally in terms of position along the line AB (figure 17) for various double-wedge configurations. $R = 0$ corresponds to point A, and $R = 1$ to point B. Note the dramatic increase in V_x as β_c (5.71°) is approached.

Figure 20. When the expansion waves, shown dotted, cross, tensile stresses develop and cavitation can result.

Figure 21. Repeated impact on a ductile material can produce a depression with a central pit. (a) to (d) represent four stages in the development of the damage. See text for details.

Figure 22. The result of ten impacts by a liquid jet (equivalent to impact by a 5 mm diameter drop) at 960 m s^{-1} on a copper target (a) top view (b) cross-sectional view. Note the development of the central pit.

Figure 23. An oblate drop can cause more damage since the effective radius at the contact point is greater and the compressible pressures last longer (a) impact of drop showing enlarged region of compressible behaviour (b) pressure profile.

Figure 24. Impacts between specimen and jet in a wheel-and-jet apparatus (a) plan view (b) side view for a well-aligned specimen (c) an angled specimen.

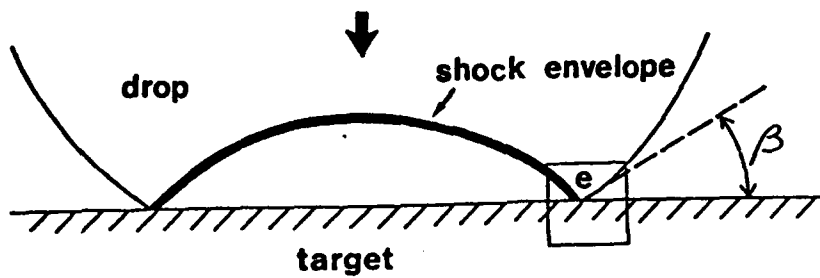


Figure 1(a) Early stage of Impact during which the contact edge.

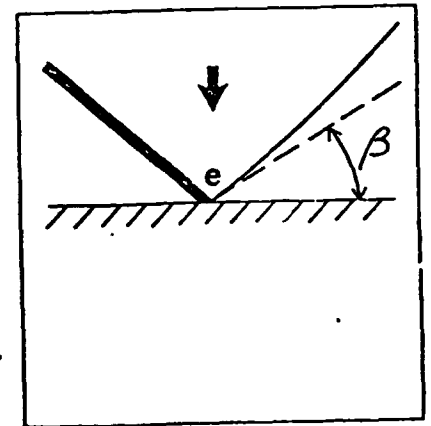


Figure 1(b) an enlarged view near, e, and the definition of the angle β.

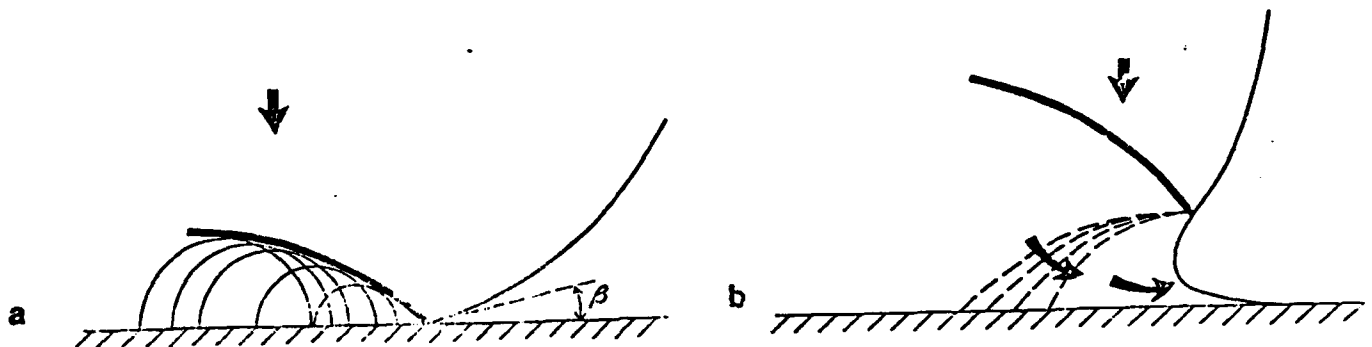


Figure 2(a) A supersonic contact edge illustrating the formation of the shock envelope from many individual wavelets (b) the wave moves up the free edge of the drop, expansion waves move into the compressed liquid, and jetting commences.

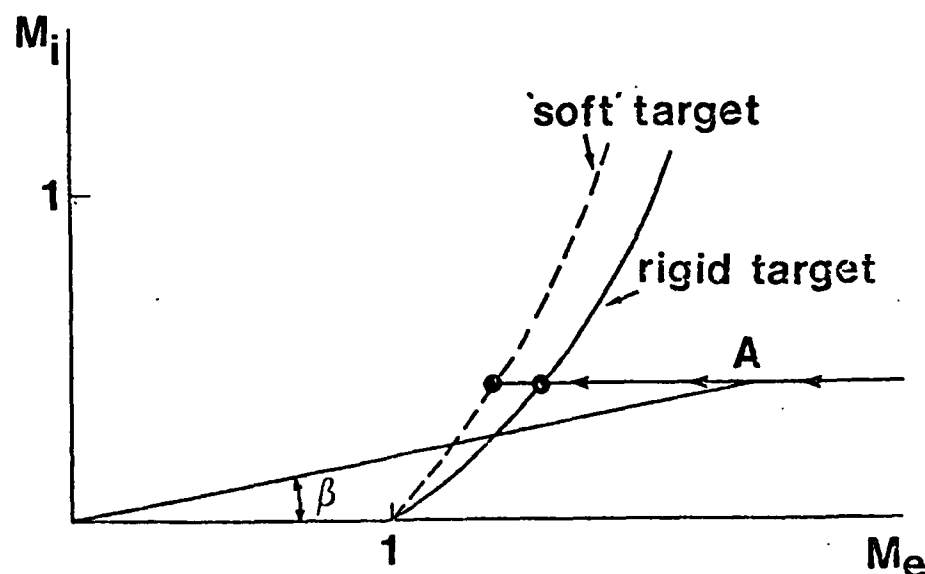


Figure 3. In this representation, a drop impacting at a particular M_i can be represented by line 1. When point A reaches the curves reaches its critical value B_c .

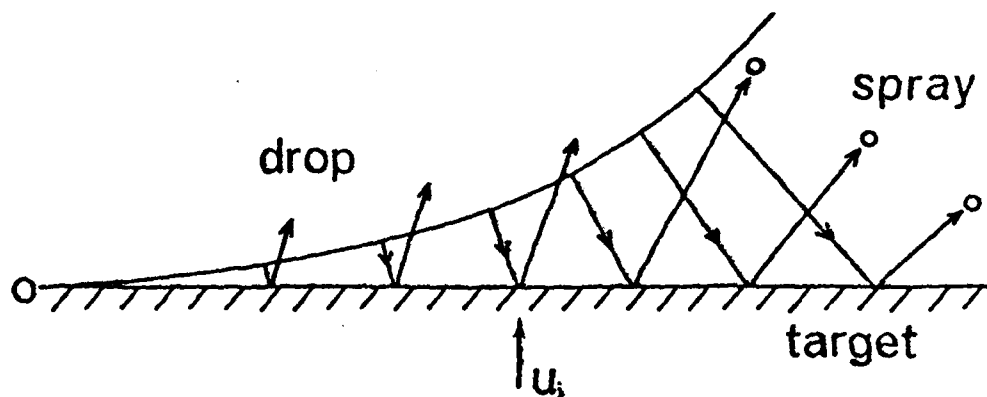


Figure 4. Jet formation; droplets detach in a direction normal to the drop surface and move initially towards the target.

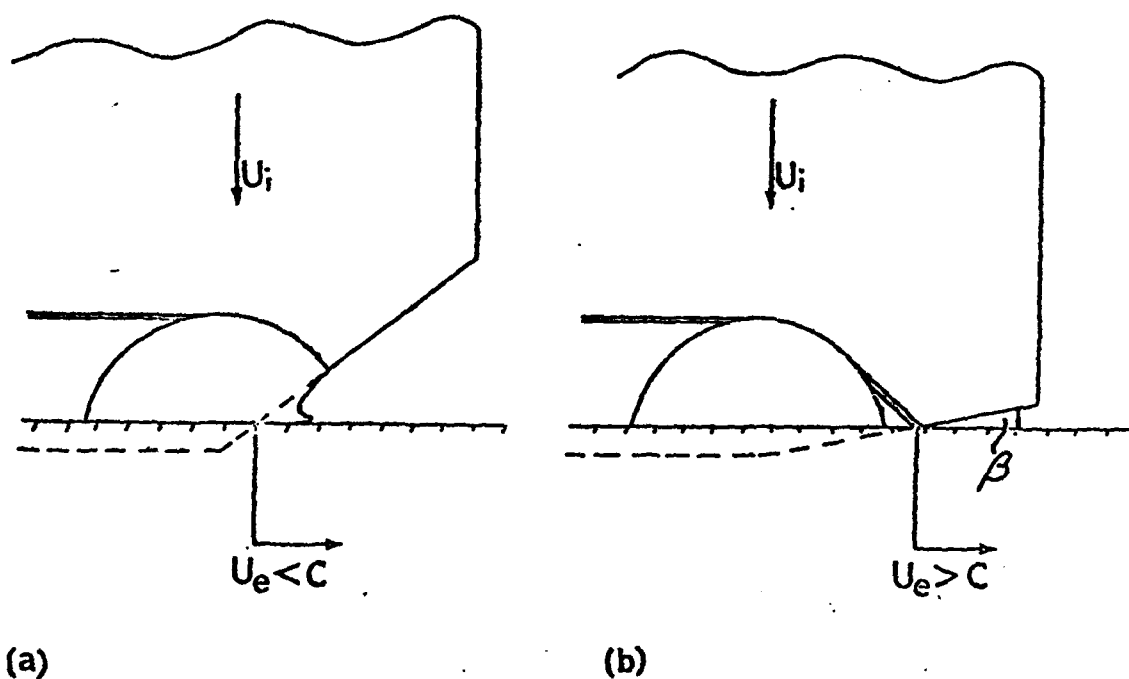


Figure 5. Shock configurations for wedges, with the primary shocks and the corner waves illustrated. In (a), the shocks move ahead of the contact point and the liquid releases forming a jet in the air wedge.

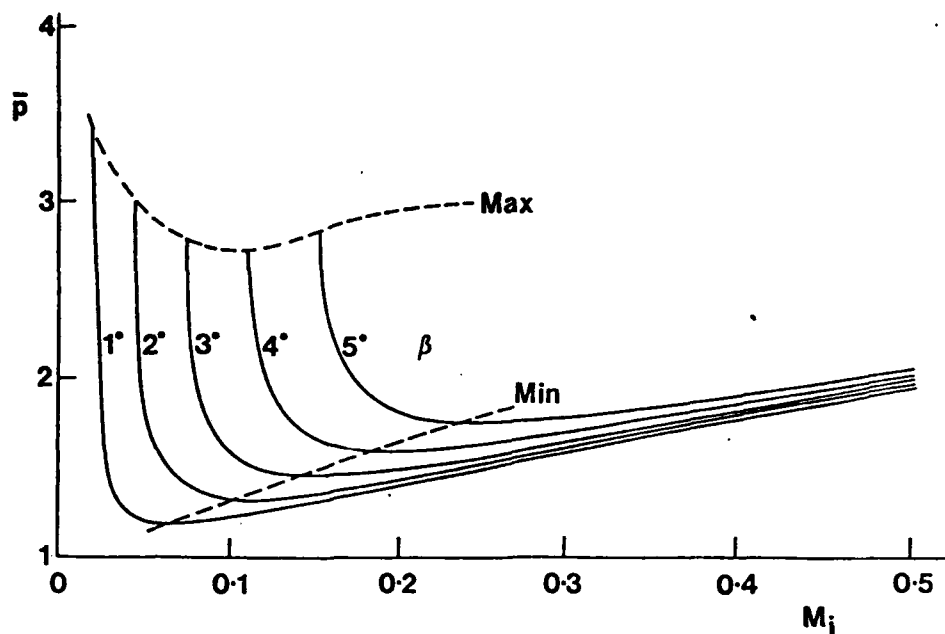


Figure 6. Non-dimensional "edge" pressures versus M_i for various values of β . Note that values of the edge pressure can reach about three times the "water hammer" pressure.

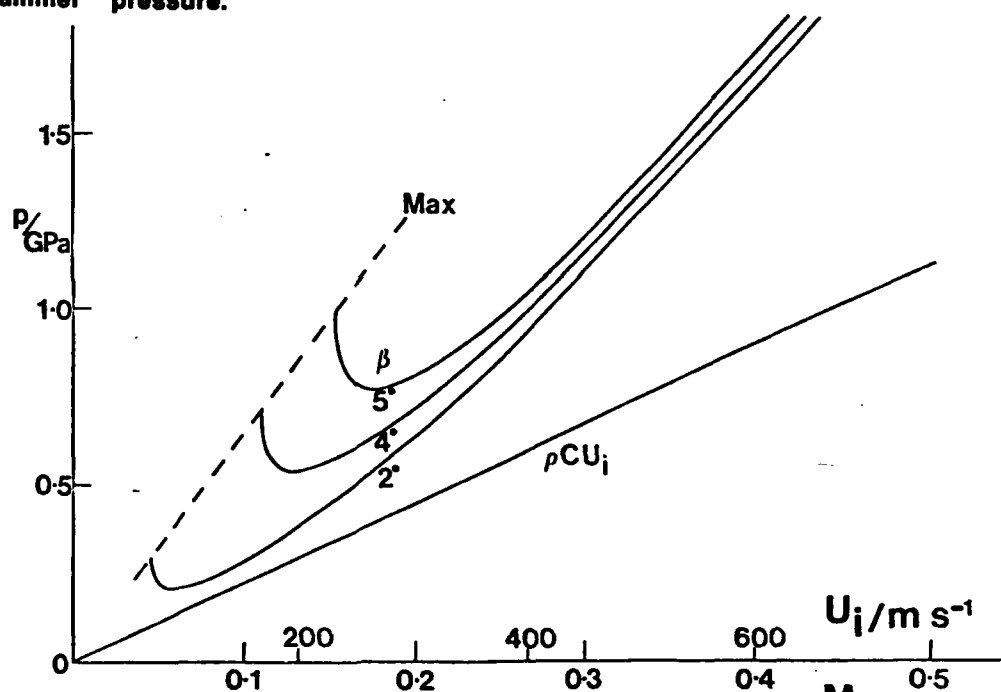


Figure 7. Absolute values of "edge" pressures versus M_i and velocity of impact U_i for various values of β .

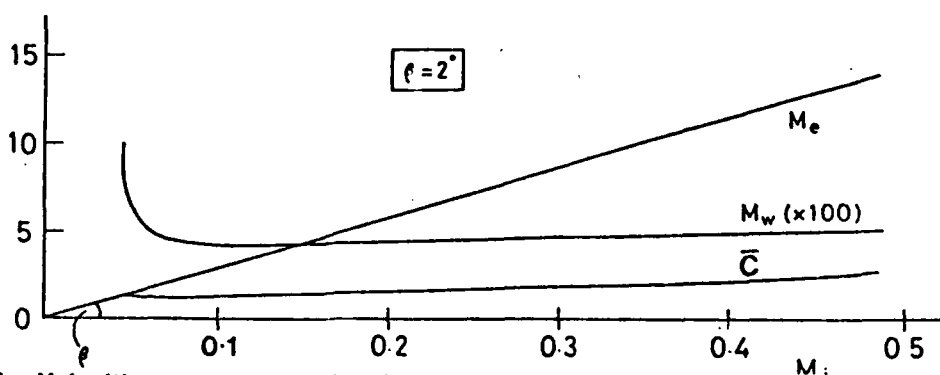
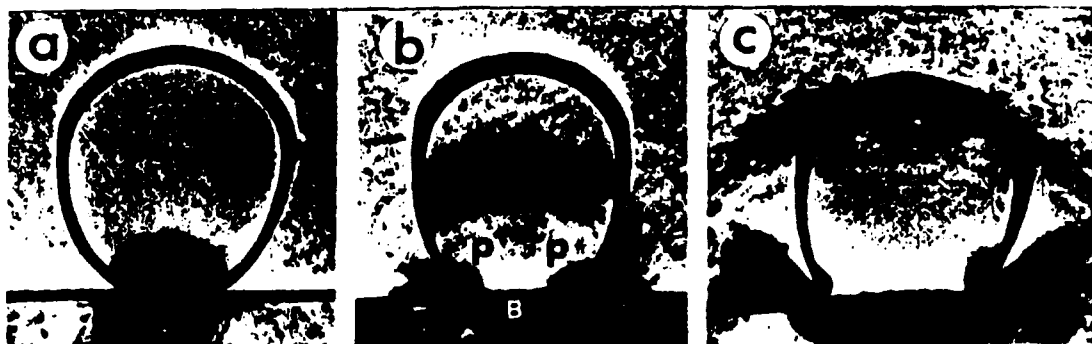
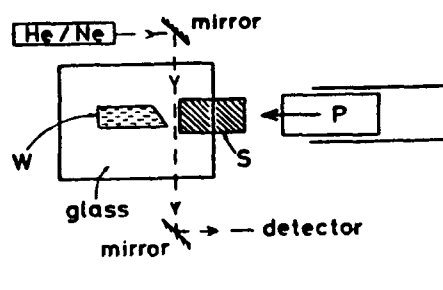
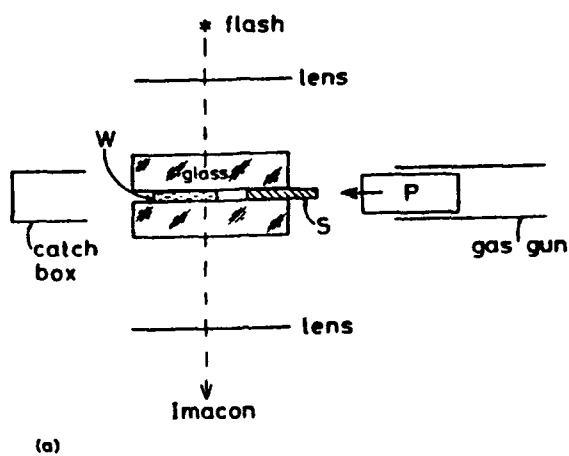


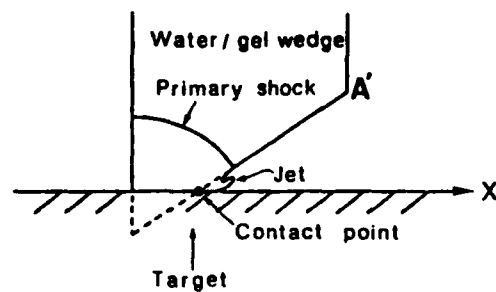
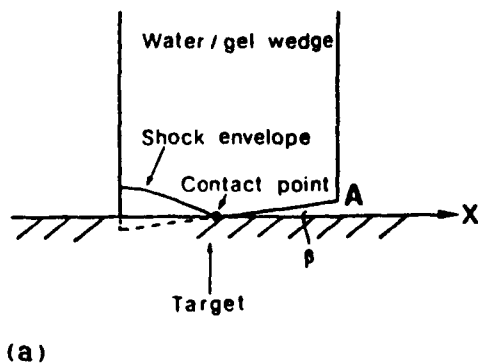
Figure 8. Velocities associated with the region in the liquid behind a supersonic contact point.



9



10



11

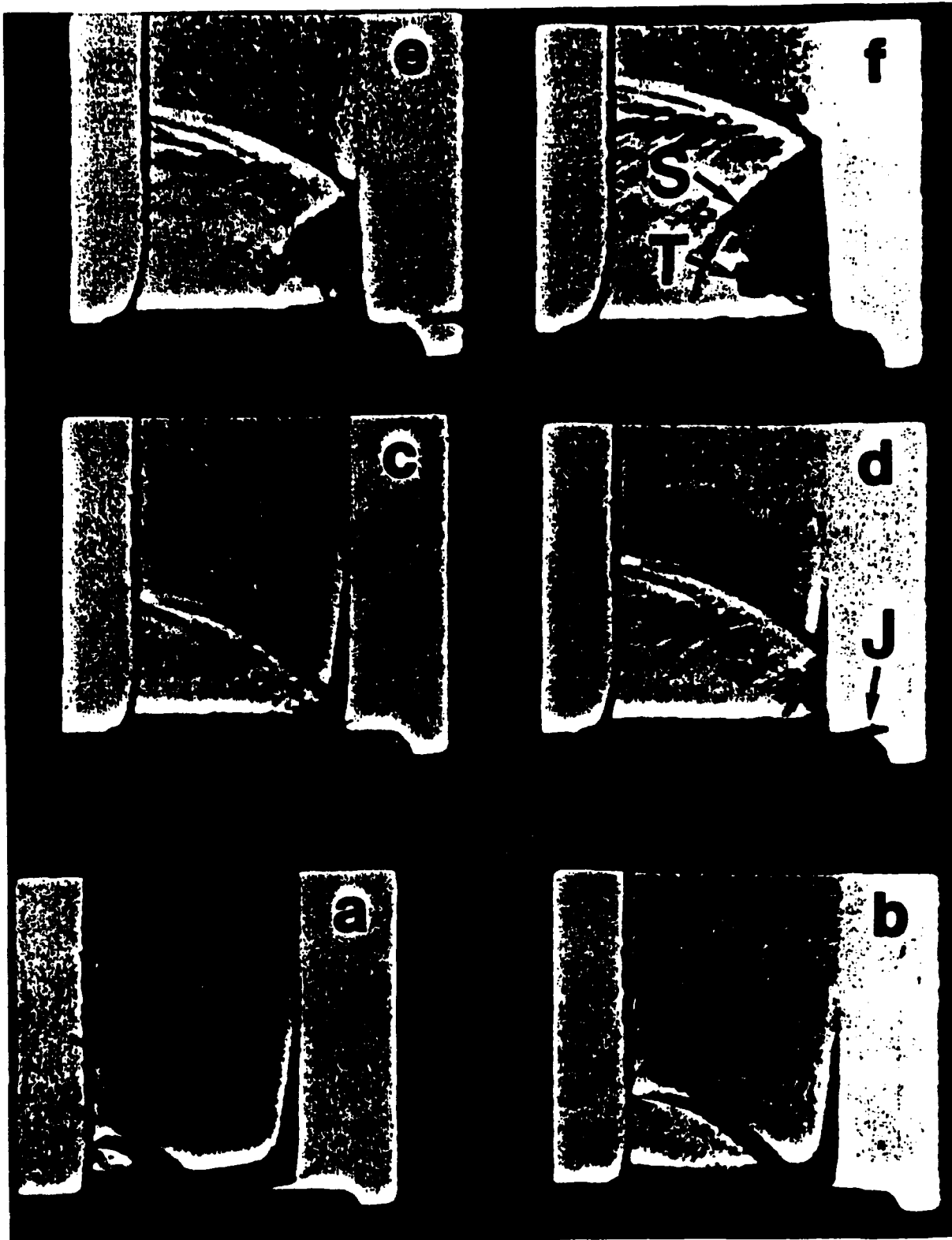
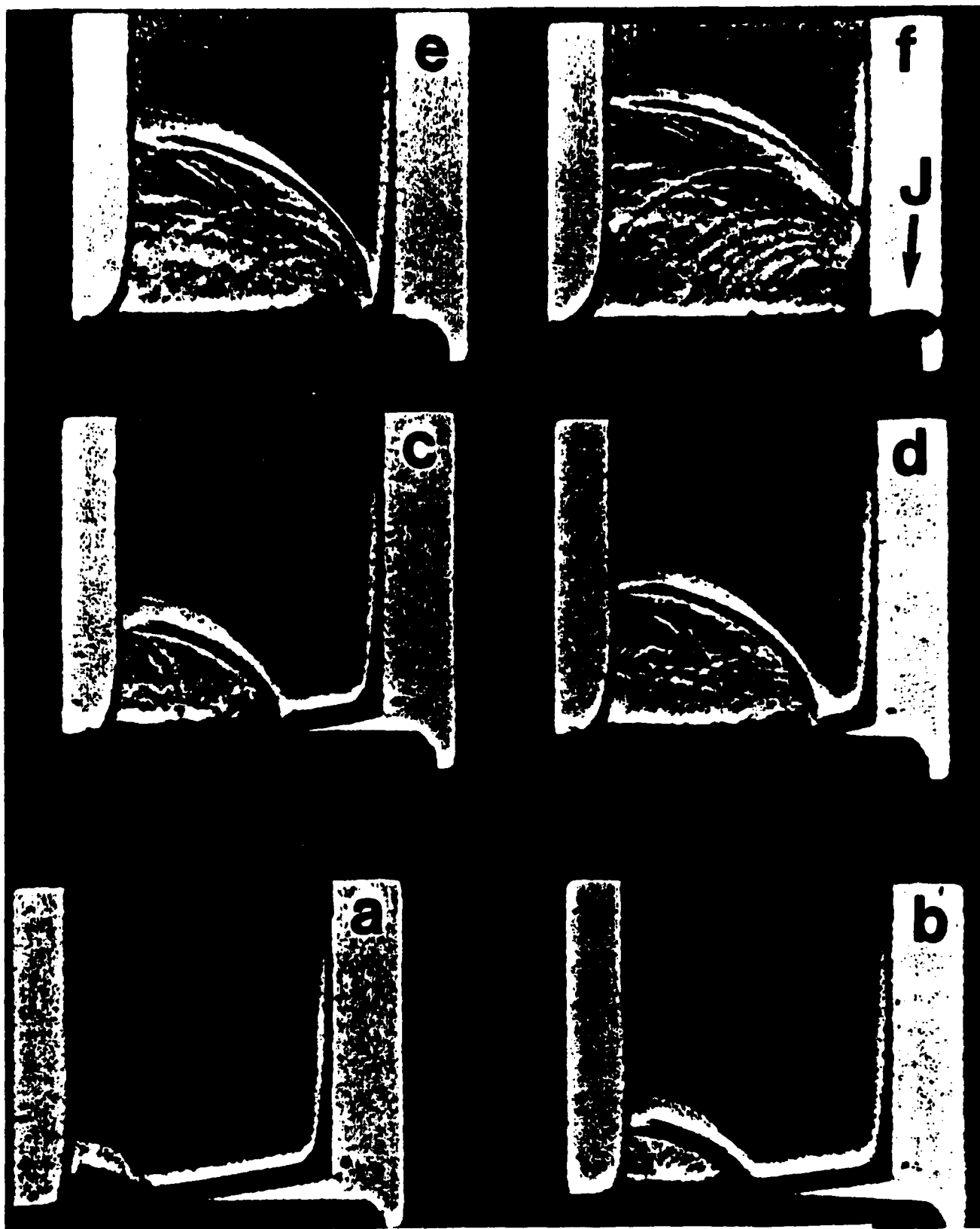


Figure 12. Impact with a wedge with θ ca. 3° and $M_1 = 0.1$. There is a supersonic contact point and no jetting in the wedge. A jet, labelled J, forms only when the shock reaches the boundary. The dark region labelled T, behind the reflected shock S, is due to cavitation. Width of gel 7.5 mm.



13. Impact with a slightly curved slider so that θ varies from 4 to 6°. The shock steepens in frames (a) to (c) and overtakes the contact point between (c) and (d). Jet formation then starts. The jet, labelled in frame (f) has a velocity of ca. 2500 m s⁻¹. Width of gel 8.5 mm.

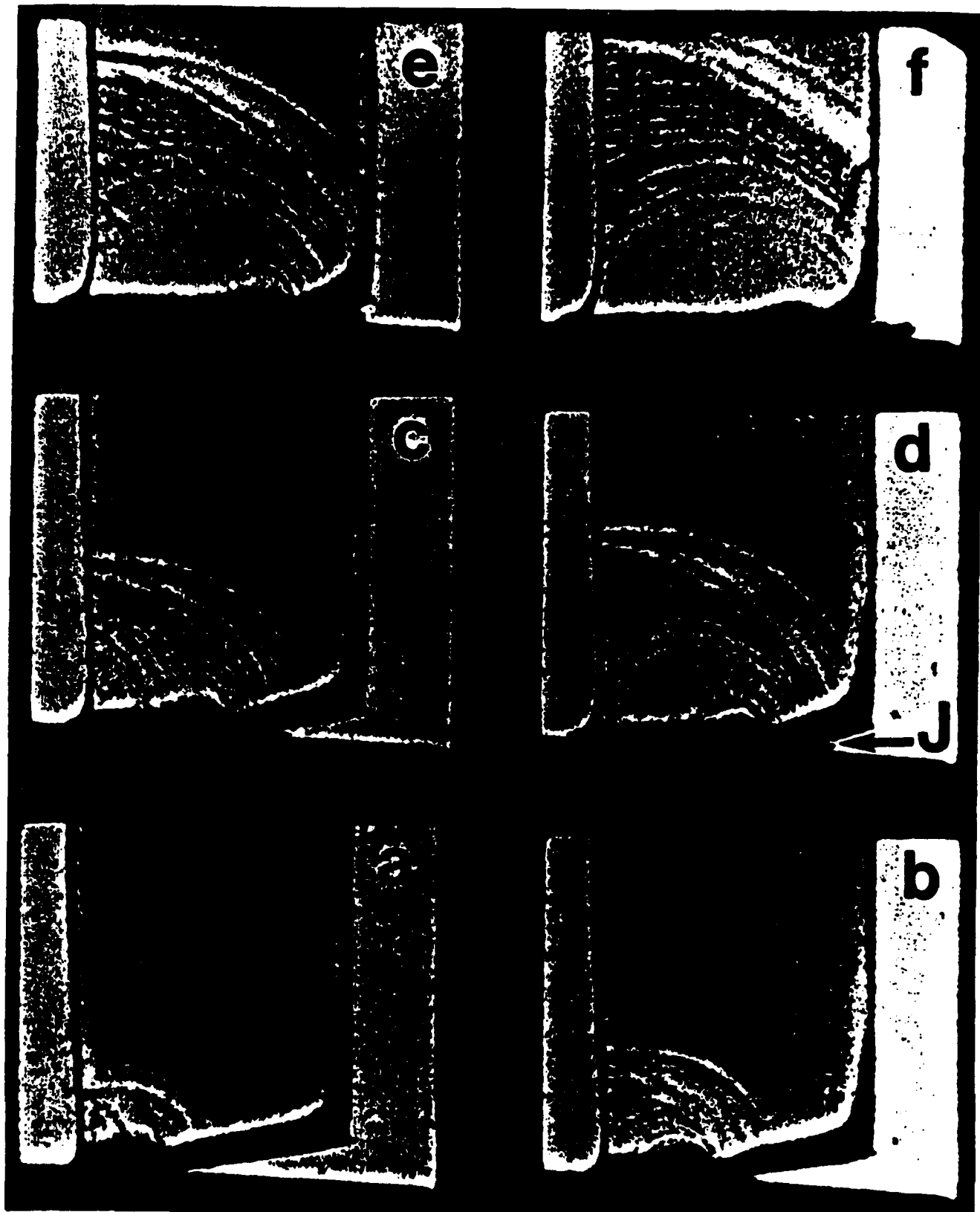


Figure 14. Impact with the wedge with θ ca. 12° , $M_1 = 0.1$. The contact point is subsonic and the wave much weaker. A jet, labelled J, appears in the gap between target and liquid. Width of gel 7.5 mm.

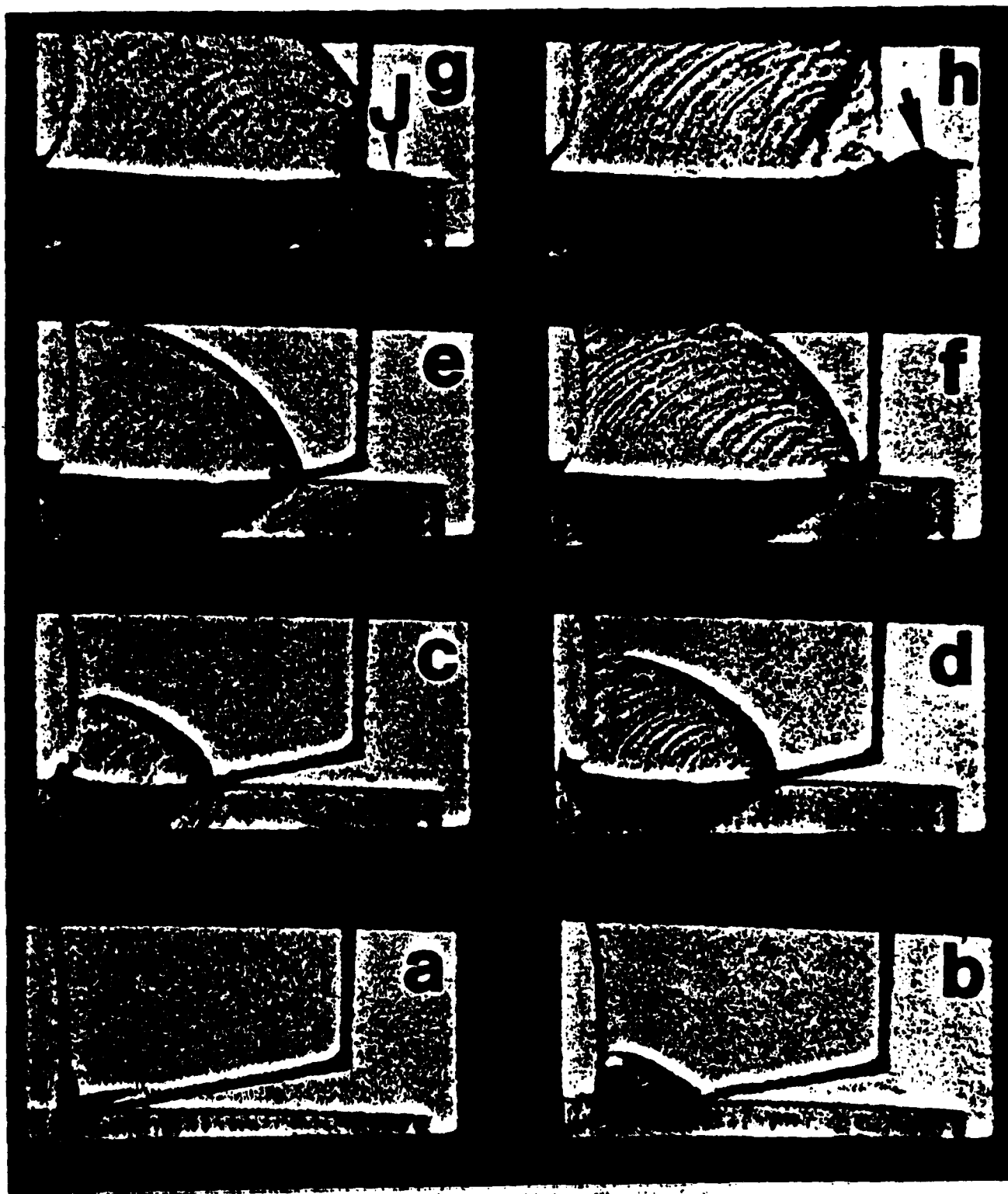


Figure 18. Impact with a high admittance plastic target M_1 (PMMA) at $M_1 = 0.2$. The target is slightly curved. In the frame (f) the shock passes ahead of the contact point and jetting starts. δ_c was ca. 10° which was significantly higher than for a rigid target. Width of gel 10 mm.

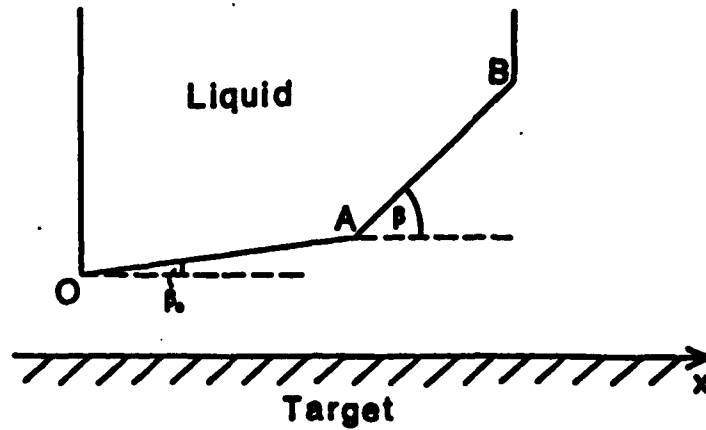


Figure 16. Impact with a double-angled wedge with $\beta_0 < \beta_c$ and variable in the range β_c to 90° .

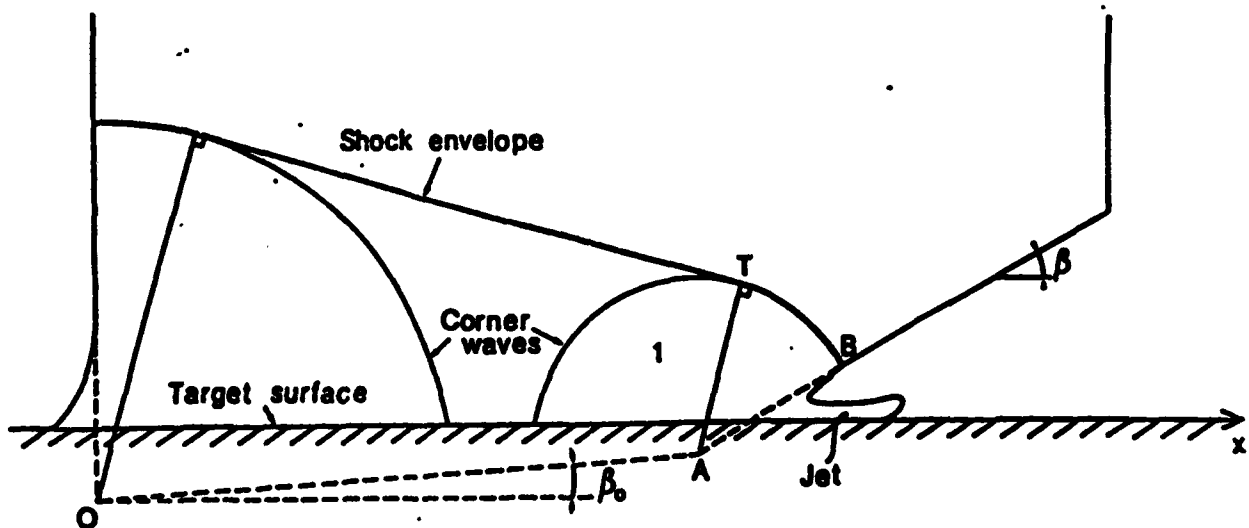


Figure 17. Situation when the target surface has passed point A and jetting has commenced. The positions of the shock envelope and the corner waves from O and A are shown.

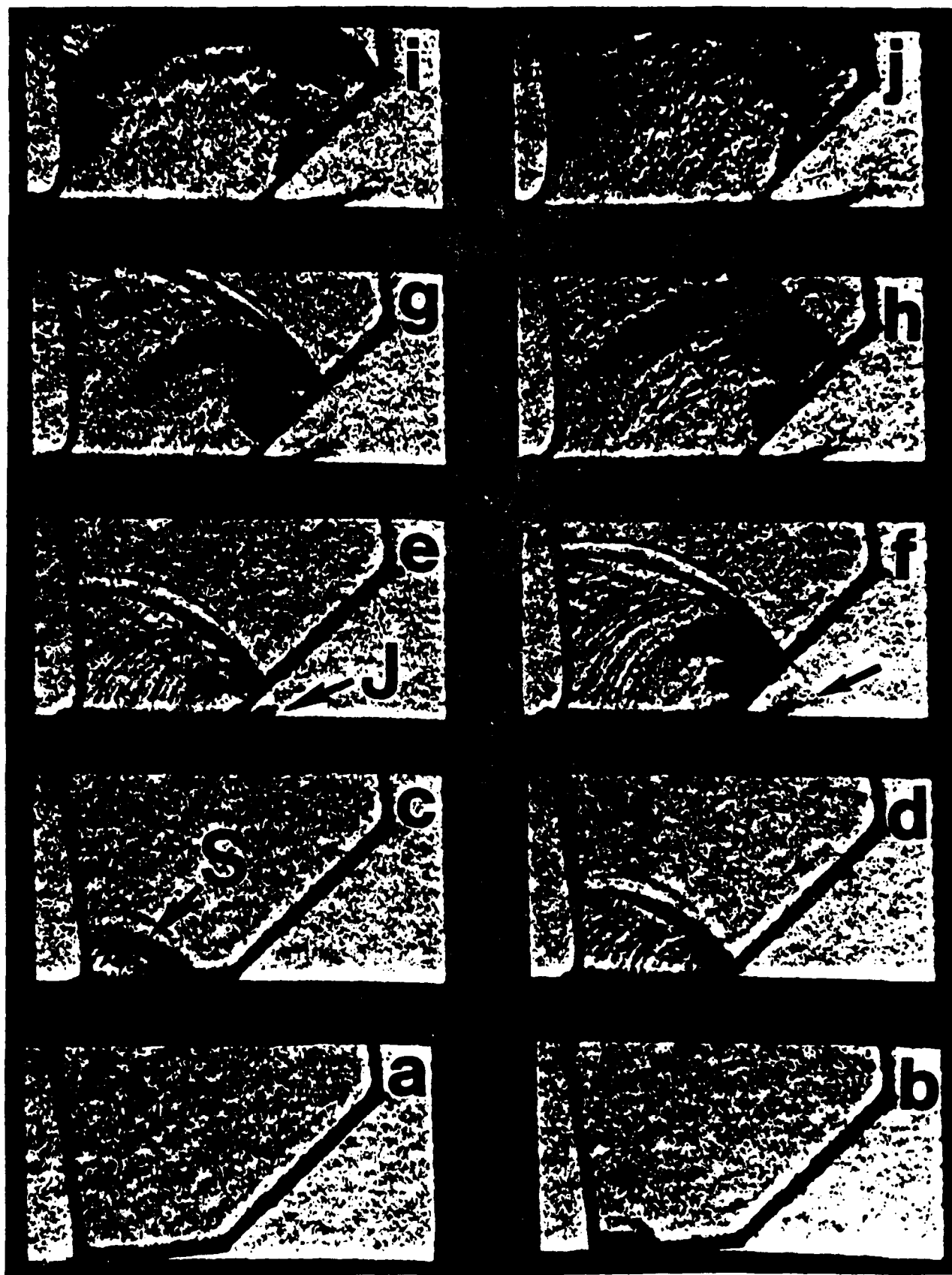


Figure 18. An example of impact at $M_1 \approx 0.1$ with a double-angle wedge with θ_0 just sub-critical and $\theta \approx 45^\circ$. The arrows mark the jet which has a velocity of $1100 \pm 100 \text{ m s}^{-1}$ in agreement with theory. Note the corner wave labelled C in frame g. Width of gel 11 mm.

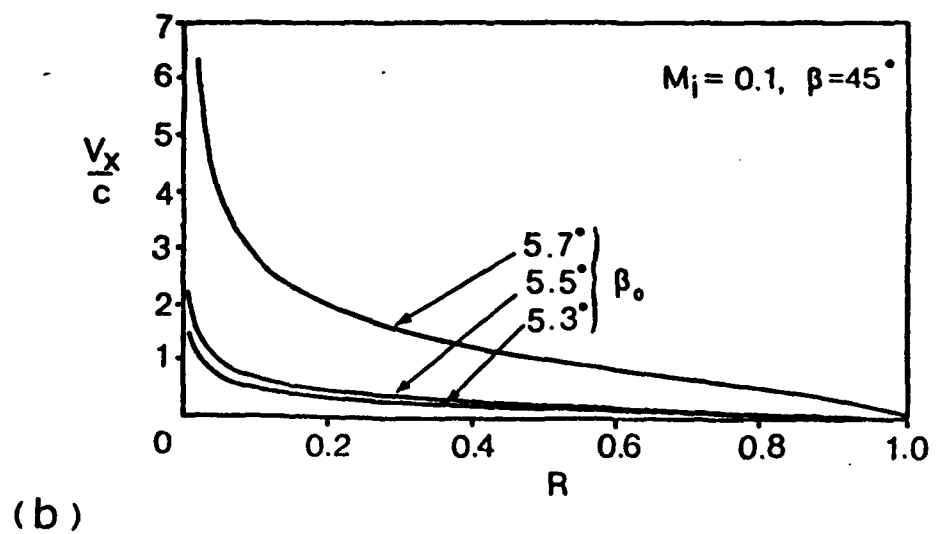
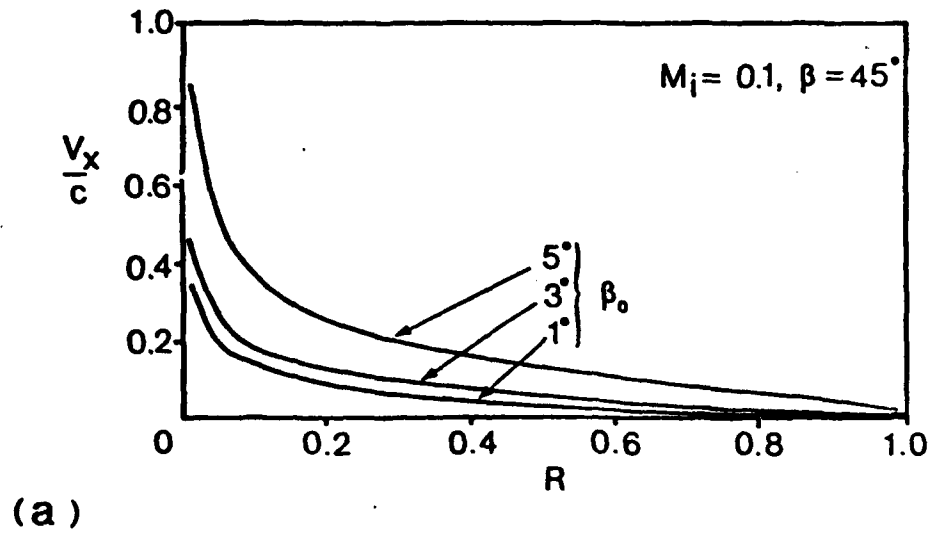


Figure 19. The x-component of the flow velocity plotted nondimensionally in terms of position along the line AB (figure 17) for various double-wedge configurations. $R \approx 0$ corresponds to point A, and $R \approx 1$ to point B. Note the dramatic increase in V_x as β_c (5.71°) is approached.

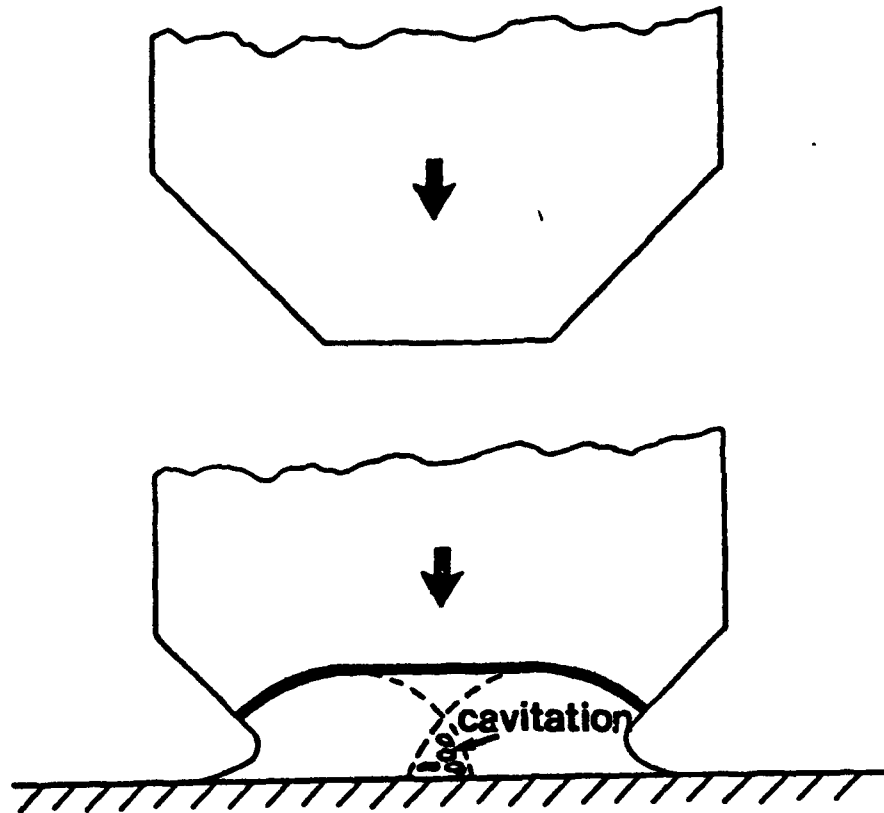


Figure 20. When the expansion waves, shown dotted, cross, tensile stresses develop and cavitation can result.

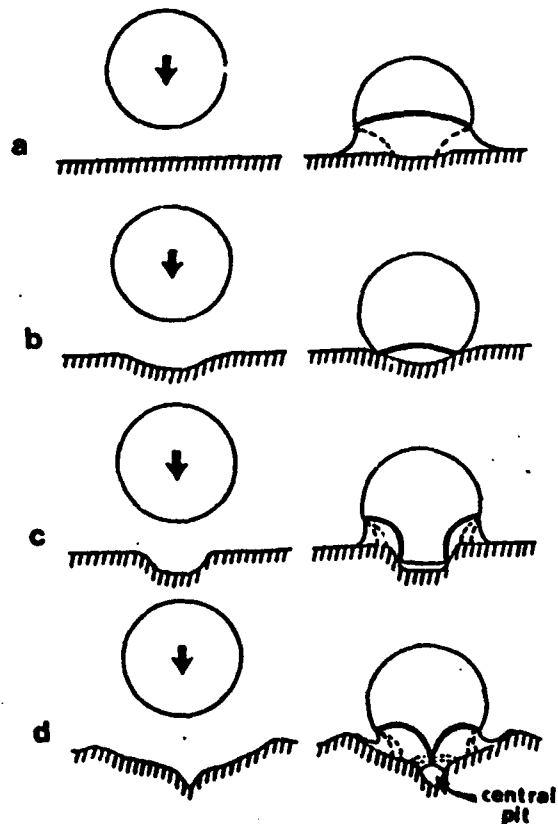


Figure 21. Repeated impact on a ductile material can produce a depression with a central pit. (a) to (d) represent four stages in the development of the damage. See text for details.

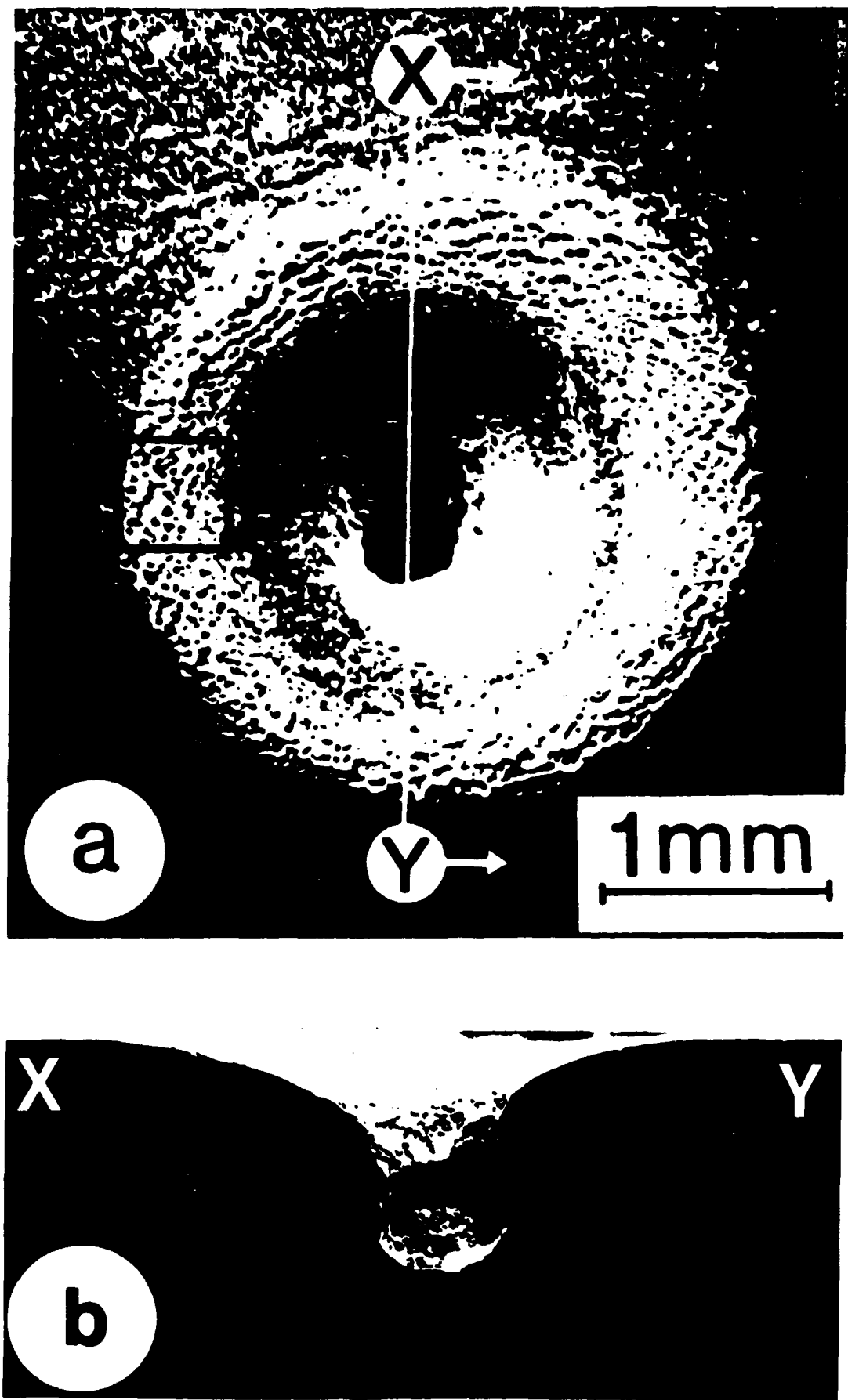


Figure 22. The result of ten impacts by a liquid jet (equivalent to impact by a 5 mm diameter drop) at 960 m s^{-1} on a copper target (a) top view (b) cross-sectional view. Note the development of the central pit.

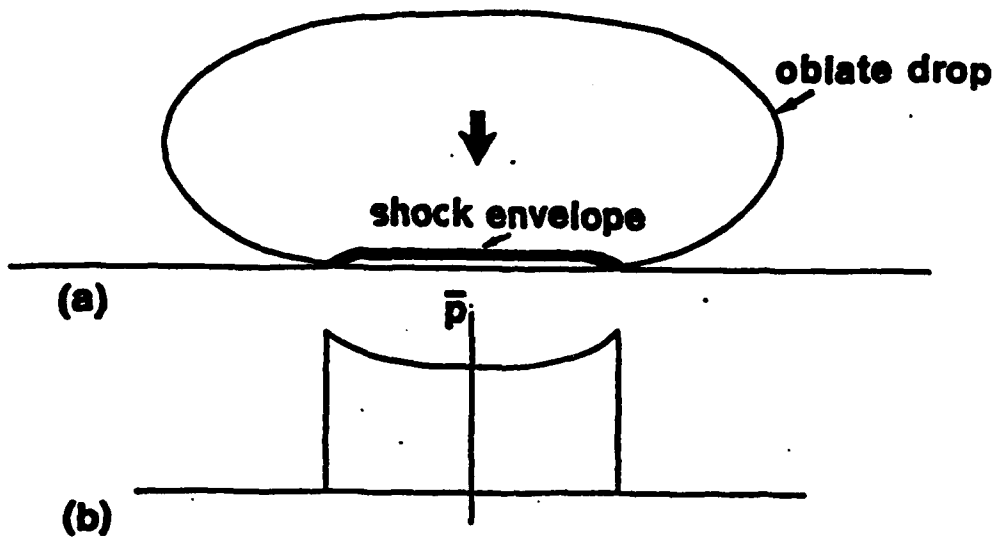


Figure 23. An oblate drop can cause more damage since the effective radius at the contact point is greater and the compressible pressures last longer (a) impact of drop showing enlarged region of compressible behaviour (b) pressure profile.

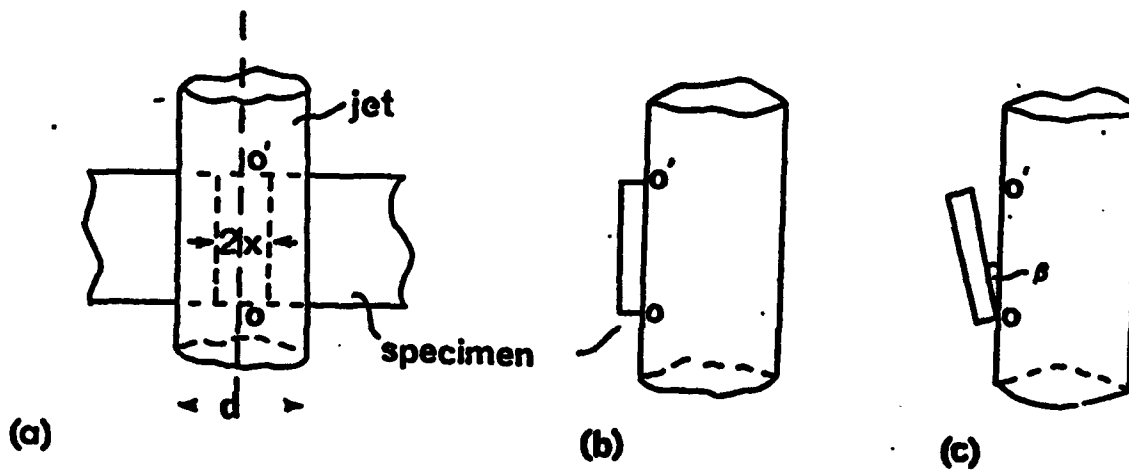


Figure 24. Impacts between specimen and jet in a wheel-end-jet apparatus (a) plan view (b) side view for a well-aligned specimen (c) an angled specimen.

SECTION III

LIQUID JET APPARATUS FOR RAIN EROSION STUDIES

3.1 INTRODUCTION

When a liquid mass impacts a solid, two distinct regimes of behaviour can be distinguished. Firstly, an initial stage during which very high pressures are generated due to the compressible behaviour of the liquid. These pressures for a rigid target are given by the equation $P = \rho CV$ where ρ is the liquid density, C , the shock wave velocity in the liquid and V the impact velocity. They are so-called "water-hammer" pressures. For a compressible target, the pressure is given by $P = V\rho_1 C_1 \rho_2 C_2 / (\rho_1 C_2 + \rho_2 C_1)$ where ρ_2 and C_2 refer to the solid. The high pressure regime continues so long as the contact area between the impacting drop and the solid expands supersonically with respect to the waves in the liquid (1-4). The duration of this stage depends on the impact velocity and the radius of curvature of the drop but is generally in the range of 0.1 - 1 μ s. In the second stage of the impact, the shock waves generated by the impact move up the free surface of the drop, jetting begins and the impact pressure drops to lower values due to incompressible flow. Incompressible flow pressures P_i are of the order $\frac{1}{2}\rho V^2$. For a 500 m s⁻¹ impact, the incompressible flow pressure is only about 10% of the pressures generated in the compressible phase. Most of the impact damage in brittle materials is associated with the initial high-pressure regime. It is for this reason that liquid jets with a smoothly curved front profile can be used to simulate drop impact to a reasonable accuracy.

A considerable amount of research has been performed at Cambridge to place the jet technique on a quantitative basis and to be able to relate jet to drop impact. This research has involved theoretical studies, damage assessment and pressure measurement for both jet and drop impact. The claim that jet impact can simulate drop impact to a reasonable accuracy has also been confirmed by work in America; research which was funded by the U.S. Navy to study the techniques developed at Cambridge (5,6).

For reasons discussed in reference 1, the radius of the region over which a drop produces water-hammer pressures is less than the drop radius and is given by $r \approx RV/C$ where R is the drop radius and V and C are as defined earlier. On the other hand, a jet (essentially a coherent cylinder of liquid) produces the high pressures over the full cylinder head radius. Thus for normal impact (i.e. at right angles to the target surface) a smaller radius jet simulates a larger radius drop. Figure 1 illustrates this point.

Curves giving the "equivalent drop" size for different sized jets plotted as a function of impact velocity are reproduced in figure 2.

3.2 JET IMPACT

The jet method was first devised by Brunton (7,8). A projectile is fired into a stainless steel chamber containing water sealed in by a neoprene disc. The projectile and neoprene drive forward as a piston and extrude the water through an orifice. The ratio of jet velocity to projectile velocity is typically 3-5. The latest version of the jet apparatus, with solenoid valve and pressure cylinder is shown in Fig. 3.

In references (9,10) we described how the 60° nozzle of Figure 4a could be used to produce jets of different sizes by varying the diameter of the orifice d . A 0.4 mm orifice jet reproduces 2 mm diameter drop impact for velocities in the range 200-600 m s⁻¹ (see fig. 2). Since a rain drop may have an oblate shape when impacted, and hence a much larger effective radius in the contact region, impacts by larger jets are also of interest. Drop sizes intermediate between the curves can be simulated by choosing an orifice size by interpolation. Very much larger jet diameters and velocities can also be produced, but these are of more practical interest in, for example, mining applications.

A disadvantage of using the chamber of Fig. 4A for a wide range of jet sizes is that it is not optimized for a particular jet size. Recently we have studied various types of nozzle design in an attempt to improve the reproducibility of our 0.4 and 0.8 mm jets. Figs. 4B and C show the nozzles which have resulted from this research. In brief, with smaller diameter jets, it helps to reduce the 60° of the Fig. 4A nozzle to ~45°. Further, if smoothing of the inside angles is practicable this also helps. This smoothing process is not easily performed with the 0.4 mm nozzle and so the design of Fig. 4B is used. However, with the 0.8 mm nozzle, it is possible and the "curved" nozzle of Fig. 4C has been adopted. Both new nozzles are loaded to the full position (F), with the liquid/air interface convex outwards.

The reproducibility of the jets was studied by taking high-speed photographs and by measuring damage marks on PMMA (polymethylmethacrylate). The results showed that if the chambers were loaded carefully (i.e. no gas bubbles or solid particles in the liquid) good coherent jets were produced each time. Compared with the nozzle of Figure 4A, the scatter in damage dimensions was reduced by about 60%. The equivalent curves of Fig. 2 apply to these latest nozzles.

Fig. 5 shows a single shot picture of a jet from a 0.8 mm nozzle. The

umbrella of spray comes mainly from the water in the parallel section of the orifice. It is made up of droplets of micron size which do not contribute to the damage. The jet front velocity increases over a distance of about 10 mm. This is clearly shown in Figs. 6 and 7 where jet velocity versus distance travelled is plotted. This behaviour is reasonable since it is only the liquid in the main part of the chamber which is accelerated through the nozzle section and it takes a finite distance for it to pass through the slower moving liquid from the orifice section. In all our experiments, the specimen is placed at a stand-off position of 10 mm.

In Figs. 8b, c we show pictures taken with the Imacon image converter framing camera of jets from 1.6, 0.8 and 0.4 mm nozzles. Note the front profiles are smooth and slightly curved. This is basically why they simulate impacts with spherical drops as well.

3.3 PRACTICAL POINTS

3.3 (a) Loading a chamber

A good quality jet will not be produced if there is any debris from the previous shot in the chamber, or if air bubbles form in the liquid.

The liquid can be added through the back of the chamber using a syringe fitted with a hyperdermic needle. The neoprene diaphragm is then added (this step may require a little practice). This diaphragm must then be pressed in until it is flush with the rear surface of the chamber. The diaphragm should then be pressed lightly until the liquid/air meniscus is convex outwards. If there is not enough liquid in the chamber to allow this, liquid should be added through the orifice section with the syringe and hyperdermic needle. Take care not to add air bubbles at this stage.

3.3 (b) Reason for convex meniscus

This type of meniscus gives jets with a smooth, slightly curved front, as illustrated in figures 5 and 8. However, a concave meniscus gives a small precursor jet, ahead of the main one. This precursor jet forms by processes similar to those which give jets from shaped charges. If such a jet is fired, it can give extra damage near the centre of the damage site. Clearly, if we are attempting to simulate drop impact, such jets must be avoided.

3.3 (c) Low velocity shots; momentum exchanger

For small orifice diameters, the ratio between the velocity of the lead slug and that of the jet is about 5. This leads to rather high minimum impact velocities, which are for some materials above their impact damage threshold velocities. To reduce the minimum impact velocity which can

reproducibly be obtained, a "momentum exchange" technique is used (figure 9a). A steel cylinder of 4.8 mm length and 4.75 mm diameter is placed between the sealing neoprene disc and the impacting lead slug. This technique reduces the jet velocity by a factor of about two.

A further reduction in minimum jet velocity is obtained by a modification of the technique illustrated in figure 9b. The dimensions of the steel or aluminium block are 12 x 12 x 21 mm. The effect of these modifications on the jet velocities for the 0.4 and 0.8 mm jets is shown in figures 10a and b respectively. Curve 1 is made without any form of momentum exchange, curve 2 with the cylindrical momentum exchanger and curves 3 and 4 with the cylinder and an aluminium and steel block respectively. The minimum jet velocity is now down to about 90 m s^{-1} for the 0.8 mm jet and to about 125 m s^{-1} for the 0.4 mm jet. These velocities are below the impact damage velocities for most of the materials of interest in aircraft applications. If required, even lower minimum impact velocities could easily be obtained by increasing the mass of the metal block used in the newest modification of the jet impact technique.

3.3 (d) PMMA

This is a useful and inexpensive test material, which at these strain rates behaves in a brittle manner. It is useful for checking that the jets are well-behaved. There should be a central, relatively undamaged central area (corresponding to compressive loading) surrounded by an annular region of short cracks. This pattern, when viewed under a low-powered optical microscope, should be symmetric.

3.3 (e) Acoustic matching

It is useful to add a backing disc of material if there is a need to impact an effectively thicker specimen. A smear of vaseline or grease will hold the specimen and backing material together, if they have flat, smooth surfaces. The longitudinal wave caused by the impact will pass over such an interface, but when it returns as a reflected tensile pulse from the rear of the sandwich, it will not pass into the specimen and affect the front surface damage.

With thin specimens, which are not acoustically matched, the reflected longitudinal wave can add to the front surface damage with high velocity impacts (see van der Zwaag and Field, 11) for discussion of this point). With soda-lime glass of 3 mm thickness, the effect was detectable above about 250 m s^{-1} , for impacts with 0.8 mm jets (equivalent to 5 mm diameter drops). This was well above the threshold velocity for sold-lime glass. For other materials, it would depend on the specimen, thickness and the acoustic attenuation coefficient. It has to be remembered that glass has a low acoustic attenuation coefficient.

The choice of whether or not to acoustically match will depend on the practical application.

Note that perfect acoustic matching need not be with the same material. All that has to be made equal is the acoustic impedance which is given by the product of density, ρ , and stress wave velocity (or, what is effectively the same $\sqrt{\rho E}$ where E is Young's modulus).

4. DAMAGE ASSESSMENT

For a discussion on how we assess damage in brittle materials quantitatively, reference should be made to last year's report (12) and also references 11 and 13. These papers give information on (a) damage in brittle materials (b) the techniques that we have developed for post-impact (residual) strength measurement which allow damage to be studied quantitatively (c) threshold damage values (d) the theory and equations for converting jet impact data to drop impact values and (e) results for Zns and relations between stress intensity factor K_{Ic} , hardness H and grain size.

REFERENCES

1. Bowden, F.P. and Field, J.E. 1964, Proc. Roy. Soc. Lond. A282, 331.
2. Heymann, F.J., 1969, J. Appl. Phys. 40, 5113.
3. Lesser, M.B. 1981, Proc. Roy. Soc. Lond. A377, 289.
4. Lesser, M.B. and Field, J.E. 1983, Ann. Rev. Fluid Mech. 15, 97.
5. Case, E.D., Louie, K.M. and Evans, A.G. 1984, J. Mat. Sci. Lett. 3, 879-884.
6. Case, E.D., Louie, K.M. and Evans, A.G. 1984, Final Report O.N.R. Contract No. N00014-81-K-1362, Univ. California, Berkeley, U.S.A.
7. Bowden, F.P. and Brunton, J.H. 1958, Nature, 181, 873,
8. Bowden, F.P. and Brunton, J.H. 1961, Proc. Roy. Soc. Lond. A263, 433
9. Field, J.E., Camus, J-J., Gorham, D.A. and Rickerby, D.G. 1974. Proc. 4th Int. Conf. on Rain Erosion and Allied Phenomena (eds. A.A. Fyall and R.B. King), R.A.E. Farnborough, 395.
10. Field, J.E., Goham, D.A. and Rickerby, D.G. 1979, ASTM STP 664 (ed. W.F. Adler), p.298.
11. van der Zwaag, S. and Field, J.E. 1983, Engng. Fract. Mech. 17, 367.
12. Field, J.E. van der Zwaag, S. and Townsend, D. 1983, Proc. 6th Int. Conf. on Erosion by Liquid and Solid Impact (eds. J.E. Field, N.S. Corney) Cambridge, U.K. Paper 21.
13. Field, J.E., van der Zwaag, S., Townsend, D. and Dear, J.P. 1983, Final Report AFWAL-TR-83-4101.

FIGURE CAPTIONS

- Fig.1 Relation between jet radius, R_j , and drop radius, R . The shaded area shows schematically the compressed liquid which generates the high pressures.
- Fig.2 Equivalent drop size as a function of impact velocity for jets of different sizes.
- Fig.3 Schematic diagram of the jet gun apparatus.
- Fig.4 (A) Nozzle which can produce jets of a wide range of sizes; d from 0.4 to 3.2mm (B) nozzle chosen for 0.4 jets (C) nozzle chosen for 0.8mm jets.
- Fig.5 Single shot photography of a jet from a 0.8mm nozzle.
- Fig.6 Jet velocity versus distance at different firing pressures for a 0.4mm nozzle. Note a plateau value is reached for a stand-off distance of ~ 10 mm.
- Fig.7 As for Fig.4 but for a 0.8mm nozzle.
- Fig.8 High-speed photographs taken with an interframe interval of $1 \mu s$ for jets from (a) 1.6mm, (b) 0.8mm, and (c) 0.4mm nozzles.
- Fig.9 Methods for reducing the jet velocity:
(a) the "momentum exchange" technique,
(b) the new method for very low velocities.
- Fig.10 (a) Jet velocity as a function of the firing pressure for the new 0.4mm diameter jet (see text),
(b) Jet velocity as a function of the firing pressure for the new 0.8mm diameter jet (see text).

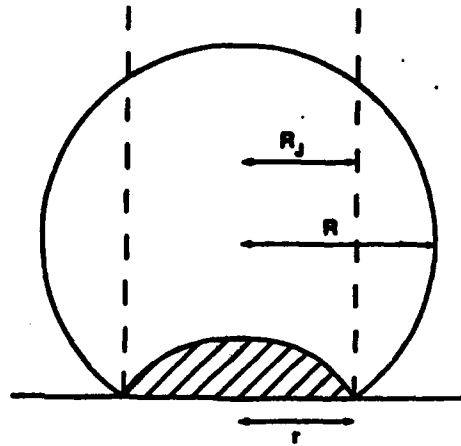


Fig. 1 Relation between jet radius, R_j , and drop radius, R . The shaded area shows schematically the compressed liquid which generates the high pressures.

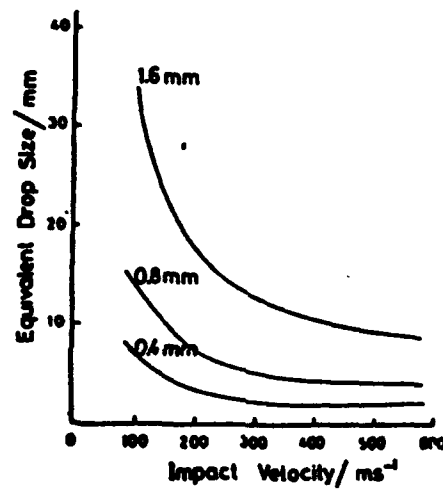


Fig. 2 Equivalent drop size as a function of impact velocity for jets of different sizes.

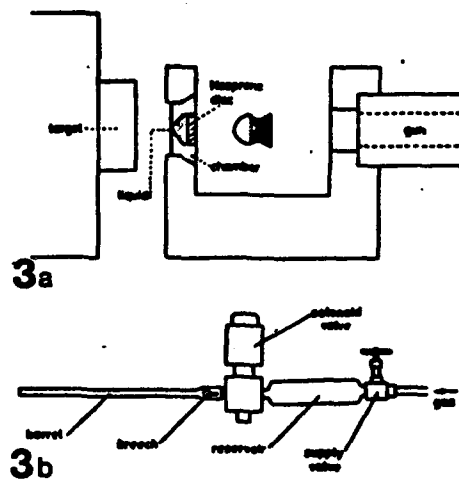


Fig. 3 Schematic diagram of the jet gun apparatus.

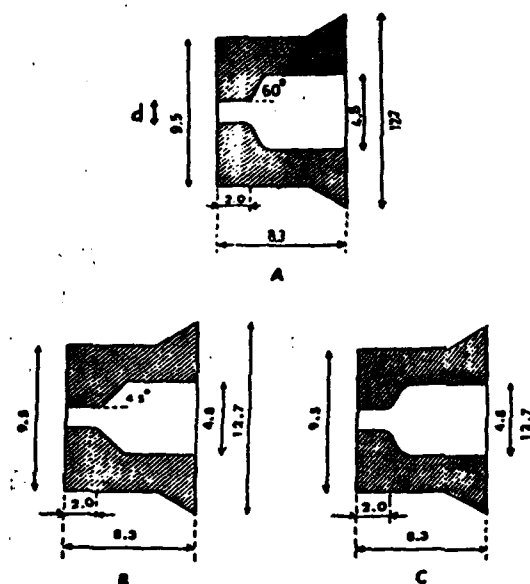


Fig.4 (A) Nozzle which can produce jets of a wide range of sizes; d from 0.4 to 3.2mm (B) nozzle chosen for 0.4 jets (C) nozzle chosen for 0.8mm jets.

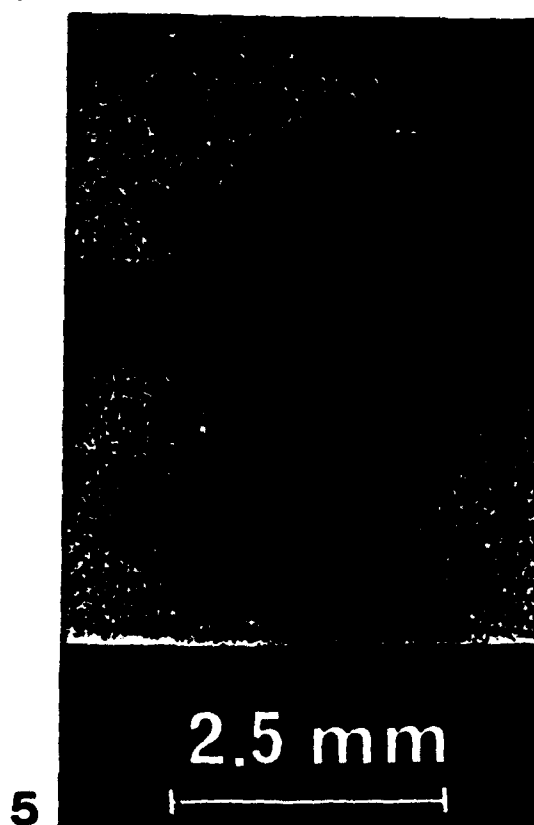


Fig.5 Single shot photography of a jet from a 0.8mm nozzle.

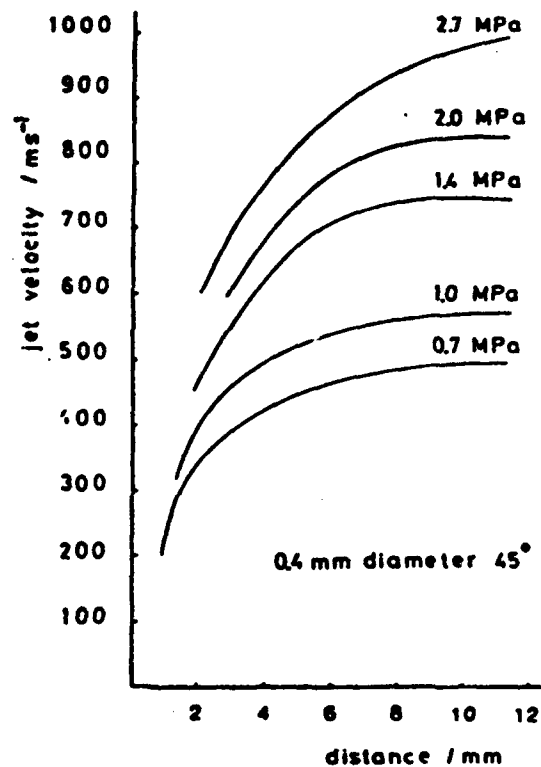


Fig.6 Jet velocity versus distance at different firing pressures for a 0.4mm nozzle. Note a plateau value is reached for a stand-off distance of $\sim 10\text{mm}$.

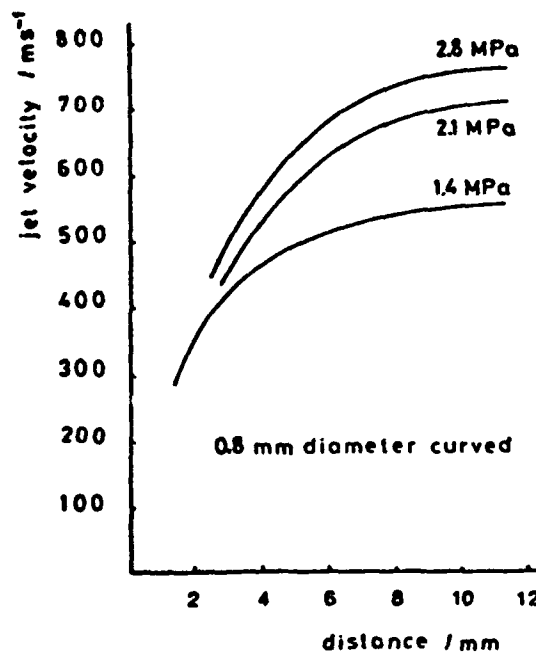


Fig.7 As for Fig.4 but for a 0.8mm nozzle.

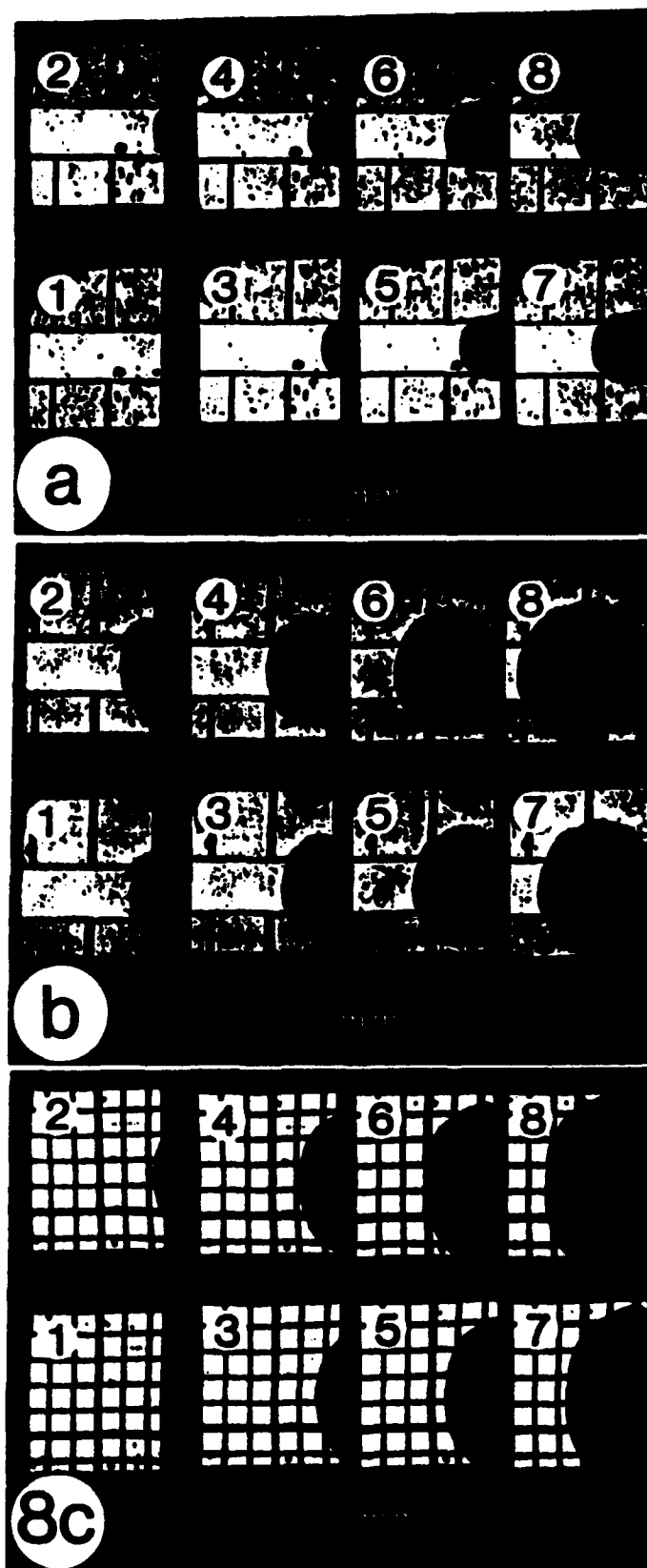


Fig.8 High-speed photographs taken with an interframe interval of $1\ \mu\text{s}$ for jets from (a) 1.6mm, (b) 0.8mm, and (c) 0.4mm nozzles.

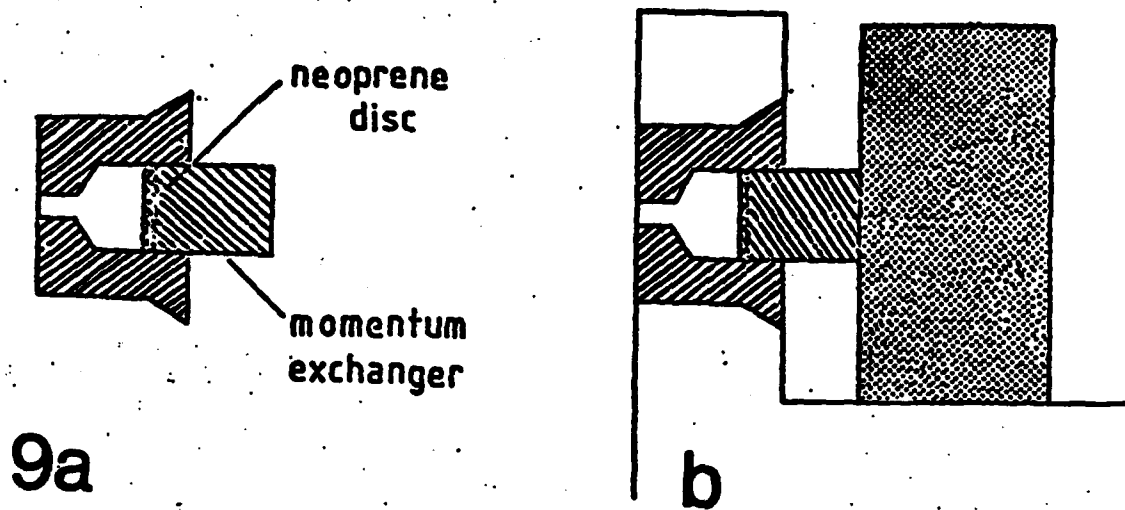


Fig. 9 Methods for reducing the jet velocity:
 (a) the "momentum exchange" technique,
 (b) the new method for very low velocities.

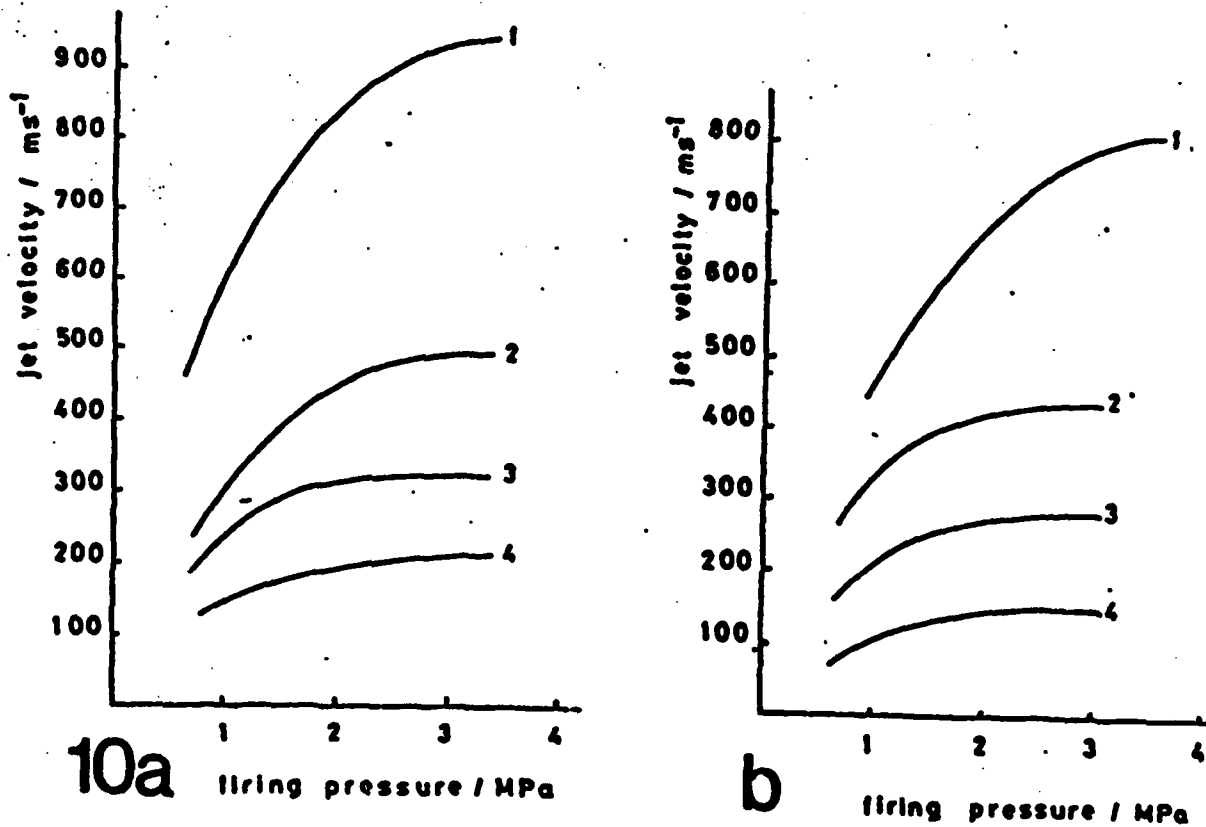


Fig. 10 (a) Jet velocity as a function of the firing pressure for the new 0.4mm diameter jet (see text),
 (b) Jet velocity as a function of the firing pressure for the new 0.6mm diameter jet (see text).

SECTION IV

THE EFFECT OF DOUBLE LAYER COATINGS OF HIGH MODULUS ON CONTACT STRESSES

4.1 INTRODUCTION

In many high technology applications a wide range of material properties is demanded for a single component. When such a range is unobtainable from a single material, surface coatings can assist in meeting the complex demands. Typical examples of well-established types of coatings are low friction coatings, wear resistant coatings, corrosion resistant coatings and optical coatings.

Coatings have also been used to improve the rain erosion resistance of exposed aircraft components. The present anti-rain erosion materials can be divided into two categories namely compliant (elastomers) and rigid materials (metals and ceramics). It has been shown theoretically (Matthewson, 1979, 1981, 1982) that a substrate is most effectively protected by a compliant coating when the Poisson's ratio of the coating approaches 0.5. The observed excellent performance of neoprene based coatings (Schmitt, 1970) is in good agreement with these predictions.

In the case of hard coating materials, very good results have been obtained for nickel plated fibre composites (Weaver, 1967). However, the application of metallic coatings will be limited since metals are opaque over a wide range of frequencies, including the visible and radar spectrum.

In comparison with the other materials, ceramic coatings are still underdeveloped because of their brittle behaviour which causes serious problems in obtaining a perfect bond between coating and substrate. However, there are several applications such as infrared transparent windows where only ceramic coatings would meet the stringent optical requirements. So far the development of ceramic coatings has been based primarily upon their optical properties and the resulting rain erosion protection has been shown to be small (Walton and Gorton, 1970; Hackworth et al 1979; Peterson, 1979).

In order to determine the optimum mechanical properties for protective coatings, a finite element model, in which rain drop impact is simulated by a static spherical indentation, has been developed (Van den Zwaag and Field, 1982). In this model, the effect of the elastic properties of the coating material and the coating thickness on the stresses in the coating and the substrate has been examined for coatings consisting of a single layer. Considerable reduction in the maximum

tensile stress in the substrate, which is responsible for crack propagation in brittle materials, can be obtained with very rigid coatings of sufficient thickness.

Ball indentation experiments on carbon-coated germanium (Van der Zwaag and Field, 1983) have shown that a thin coating ($\leq 3 \mu\text{m}$) can increase the critical load for crack nucleation up to 400%. The observed increase of the fracture load with the effective coating thickness was in good agreement with the theoretical predictions.

In the present work we have expanded the model to examine the potential of coatings consisting of two different rigid materials.

4.2 THE MODEL

In the model a circular area with a radius a is loaded normal to the coating surface. The pressure distribution over the contact area is given by

$$P(r) = P \left\{ \frac{a^2 - r^2}{a^2} \right\}^{1/2} \quad (1)$$

where r is the radial coordinate and P the maximum pressure at the centre. This pressure distribution is identical to the pressure distribution in the case of Hertzian contact on a uniform half space (Hertz 1881, Huber, 1904). Due to the circular symmetry of the problem the stress fields can be calculated using a two-dimensional finite element model. The elements are in the plane of a cross-section through the centre of contact.

The element distribution used is shown in figure 1a. The elements are divided into three groups: one with the (fixed) substrate properties and two with the (variable) coating properties. Figure 1b shows a detail of the element distribution near the contact zone. The elements with the coating properties are shaded in this figure. The accuracy of the finite element programme has been tested by comparing the results for an uncoated halfspace (i.e. the properties of the two coating layers are equal to those of the substrate) with the analytical solution of the stress field. For the present element distribution, the difference between the two solutions is always less than 1%. Throughout the analysis the elastic properties of the substrate are kept constant with a Young's modulus of 61GPa and a Poisson's ratio of 0.25 (i.e. typical values for a soda lime glass). Young's moduli of the two coating materials were varied between 2 and 10 times that of the substrate material. This range covers nearly all possible hard coating materials. Since the analysis for single layer

coating systems has shown that the effect of the Poisson's ratio of the coating material on the stress field is small for Poisson's ratio varying from 0.20 to 0.30, the Poisson's ratio of all coating materials was kept constant at $\nu = 0.25$.

The effect of the total coating thickness has been investigated for thicknesses up to 12% of the contact radius. In the following sections, the stresses are normalised to the maximum pressure at the centre of the contact area such that positive values indicate tensile stresses and negative values compressive stresses. To distinguish between the various coating systems, the following notation is introduced: $E_1/E_2/t_1/t_2$ where E_1 and E_2 are the moduli of the outer and interlayer both normalised to the modulus of the substrate E_s and t_1 and t_2 the corresponding thicknesses.

4.3 RESULTS

Elastic contact between an uncoated brittle material and an indenting or impacting particle can cause damage due to the development of radially oriented tensile stresses in a shallow surface layer around the contact area. The circumferential and axial stresses are compressive everywhere in and around the contact zone and do not contribute to the damage process. Also in the case of the coated halfspaces investigated here, the finite element calculations have shown that the only stresses which can be tensile and hence can cause crack propagation are the radial stresses. It is for this reason that this paper deals primarily with the effect of the various coating parameters on the radial stress field.

4.3(a) The radial stress fields in two example programmes.

Before dealing with the results in a general way, the radial stress fields in two double layer coating systems are presented and discussed in detail. In the first demonstration programme, the stresses are calculated for a 5/2/0.015a/0.015a coating system. The second demonstration programme deals with a 2/5/0.015a/0.015a system. Figures 2 and 3 show parts of the radial stress field at the surface, at the interlayer and at the substrate for the two coating systems.

The plotted radial stress for the interlayer is the stress field in the interlayer at the interface with the surface coating. Similarly, the plotted radial stress in the substrate is that which occurs in the substrate at the interface with the interlayer. In both figures the radial stress field which would occur in an uncoated halfspace of substrate material at the depth of the substrate interface is indicated by

a dashed line. The figures show that both coating systems reduce the substrate stresses by an equal amount. For an uncoated specimen, the maximum radial stress at a depth of $0.03a$ below the surface is $0.078P$ while for both coated specimens the maximum radial stress in the substrate is $\sigma_r \max = 0.043P$. This value should be compared with $\sigma_r \max = 0.060P$ for a monolayer coating with $E_c = 5E_s$ and a thickness of $0.015a$ and with $\sigma_r \max = 0.031P$ for a coating thickness of $0.03a$. As expected intuitively the coating configurations in the example programmes are more effective than just a thin monolayer of the most rigid coating material and less effective than a monolayer of equal thickness to the sum of the outer and interlayer thicknesses.

When comparing the stresses at the surface and at the interlayer for the two coating systems of figures 2 and 3, large differences are observed. In the case of the rigid interlayer, the largest radial stresses occur below the surface while with the 5/2 system a more normal behaviour is observed. The largest radial stresses occur in the system with a rigid facing. The high stresses in the coatings are due to the relatively large deflections of the perfectly adhering substrate.

4.3(b) Effect of the coating parameters on the radial stress in the substrate

As was shown for the 5/2/0.015a/0.015a and 2/5/0.015a/0.015a coating systems (figures 2 and 3), the presence of a coating leads to a significant decrease of the radial stresses in the substrate. In figure 4 the normalised maximum radial stress in the substrate is plotted versus the coating thickness for all coatings investigated. In all double layer coating systems the thickness of the surface layer equals that of the interlayer. The dashed line labelled "Hertz" indicates the decay of the maximum radial stress with depth below the surface for a uniform halfspace with the properties of the substrate.

The dashed lines labelled 2, 5 and $10E_s$ indicate the stress reduction for the case of a monolayer coating with a Young's modulus of 2, 5 and $10E_s$ respectively. The conclusion from the two demonstration programmes in the previous section that the radial stress field in the substrate is independent of the stacking of the two layers (i.e. a system with a rigid surface layer is as effective as a system with a rigid interlayer) is valid for all coating combinations investigated. Figure 4 shows that at a fixed total coating thickness the effect of a double layer system is always less than that for the case of a monolayer of the more rigid coating material but more than that for a coating of the less rigid

material.

This is shown in more detail in figure 5 which shows the maximum radial stress at the substrate for 5 combinations of relative coating thicknesses at a fixed total coating thickness of $0.03a$. Young's modulus of the surface layer is $5E_s$ and that of interlayer $2E_s$. The calculations show a continuous decrease in maximum radial stress with increasing relative coating thickness of the more rigid coating material. Similar results are obtained for coatings of the 2/5 type.

It should be noted that the presence of a (single or double) coating increases the radial distance at which the maximum stress in the substrate occurs. Since the probability of propagating pre-existing defects in brittle materials depends on both the magnitude of the stress field and the size of the surface area stressed, the increase in distance reduces the effect of the coating. However, since the radial tensile stress is everywhere smaller than that for an uncoated substrate these hard coatings do indeed protect the substrate.

4.3(c) Effect of the coating parameters on the interlayer stresses

The maximum tensile stresses in the interlayer at the interface with the outer coating are plotted for the various coating systems in figure 6 as a function of the total coating thickness. The figure shows a rapid decrease of the maximum stress with coating thickness. In the case of a hard interlayer the stress level is high due to the limited protection offered by the outer coating while for the 10/2 and 5/2 systems the stresses in the interlayer are relatively low.

4.3(d) Effect of the coating parameters on the surface stresses

In contact problems involving brittle coating and substrate materials, failure of the total structure may be caused by propagation of flaws located either at the coating surface or at the substrate. It is therefore important to examine stresses at the surface of the outer coating.

The maximum tensile stresses at the surface are plotted in figure 7 as a function of the coating thickness. In all coating systems examined the maximum tensile stress is higher than the value for a homogeneous halfspace $\sigma_{\max} = 0.167P$. The largest increase is found for coatings of the 10/2 type while the smallest increase occurs in the 2/10 systems.

For the double layer coatings examined here, the maximum radial stress for a given coating system is approximately constant for total coating thickness less than $0.12a$. Calculations for monolayer coatings

have shown that the maximum tensile stress in these cases increases with coating thickness. Unfortunately, with the present model no accurate calculations of the surface stresses are possible for coating thickness less than 0.015a.

4.4 DISCUSSION

When an uncoated substrate is loaded the maximum tensile stress is $\sigma_r, \max = 0.167P$. In all coating systems examined here, higher values for the maximum stress are found, either in the interlayer (2/5 and 2/10 systems) or in the outer coating (5/2 and 10/2 systems). This indicates very clearly the point that only those materials which have a higher fracture stress than the substrate material can be used as a protective coating.

However, examination of the mechanical and elastic properties of various (infrared transparent) materials shows that in general the fracture stress σ_f (for macroscopic specimens) increases with increasing Young's modulus as shown in figure 8. Such a linear dependence between fracture stress and Young's modulus is also predicted by simple models for the theoretical strength of solids which yields $\sigma_f = (E\gamma_0/r_0)^{1/2}$ where γ_0 is the fracture surface energy per unit area and r_0 the interatomic distance. For the data compiled in figure 8, the data can be described by $\sigma_f = E/1600$. Although such a simple relation is unlikely to hold true for very thin coatings of rigid materials the general trend is probably correct. Also our results for indentations on carbon coated germanium support this prediction.

As mentioned earlier, not only the magnitude of the stress field is important but also the spatial distribution of the tensile stresses. Whilst the maximum tensile stress is almost independent of the total coating thickness, the distribution of the radial stress changes markedly with coating thickness. This is illustrated in figure 9 where the radial stress outside the contact area is plotted for three different coating thicknesses. In all cases $E_1 = 5E_s$, $E_2 = 2E_s$ and $t_1 = t_2$. In these figures the decay of the radial stress with radial distance for an uncoated halfspace ($\sigma_r = \sigma_{r, \max} a^2/r^2$ for $r \geq a$) is indicated with a dashed line. For the thin coatings the relatively large deflections of the interlayer cause a significant increase in the area stressed by relatively large tensile stresses. For brittle materials, such an increase is clearly detrimental. Similarly, in the case of a rigid interlayer the tensile stresses in the outer coating decay more rapidly than in the case of an uncoated halfspace.

It should be mentioned here that in the model it is assumed implicitly that there is a perfect bond at the various interfaces. In practice, however, delamination can occur which will reduce the effect of the coating considerably and which will lead to coating removal and a complete loss of protection. Examination of the interfacial shear stresses for several single and double-layered systems has shown that the magnitude and spatial distribution of the interfacial shear stresses do not vary much between the different systems. This means that the interfacial bond strength rather than the coating properties will determine the likelihood of delamination. Since the bond strength depends on technological parameters and the reactivity of the compounds and not on the elastic properties, no suggestions can be made for coating systems with a high resistance against coating delamination.

Finally, the problem of the correct layer sequence of a double coating is addressed. While the sequence of coating layers will often depend on technological feasibility and/or restrictions due to optical requirements the stress analysis presented here, in conjunction with the assumed linear dependence of fracture stress on Young's modulus, suggests that coatings with a rigid outer layer and an interlayer of intermediate stiffness are likely to perform better than coatings with a rigid interlayer.

This preference for rigid outer coatings is based on the ratio's of the maximum surface stresses. For example, for coatings of the 10/2 type $\sigma_{r,max} = 0.62P$ and for coatings of the 2/10 type $\sigma_{r,max} = 0.23P$ (figure 7). The ratio of the two stresses is less than the predicted ratio between the fracture stresses of the two materials (which is 5). The relatively large area with high tensile stresses for coatings with a rigid outer layer (figure 9) makes the difference between the two types of coating smaller.

4.5 CONCLUSIONS

It has been shown that thin hard coatings, either consisting of a monolayer or a double layer, reduce the maximum tensile stress in the substrate compared to the values for an uncoated halfspace under the same loading conditions. Thin, hard coatings can therefore in principle be used to protect brittle materials against elastic contact damage. Comparison of double layer coatings with monolayer coatings shows that for a given total coating thickness the substrate stresses are more effectively reduced by a monolayer of the hardest of the two materials used in the double layer. However, for the double layer coatings the

surface stresses in the outer coating are lower than in the case of monolayer coatings in particular for larger coating thickness. A further important practical advantage is that thick monolayers are difficult to fabricate without developing residual stresses which encourage delamination. A multilayer system with layers of different modulus could, in principle, be built up to relatively large thicknesses without delamination.

Although the performance of a coating depends on a number of factors other than just the stresses, such as fracture strength and toughness of coating and substrate material, interfacial strength, pre-existing stresses and flaw statistics, the calculations suggest that double layer coatings might perform better than monolayer coatings. The best results are predicted for the coatings with a rigid outerlayer and an interlayer of intermediate stiffness.

REFERENCES

1. Hackworth J.V., Kocher L.H. and Snell I.C. (1979), In "Erosion; Prevention and Useful Applications", STP 664 ASTM Philadelphia, PA. (ed. W.F. Adler) p.225
2. Hertz H. (1881), J. Reine u. Angew. Math. 92, 156
3. Huber M.T. (1904), Ann. Physik. 14, 153
4. Matthewson M.J. (1979), Ph.D. thesis, University of Cambridge
5. Matthewson M.J. (1981), J. Mech. Phys. Solids 29, 89
6. Matthewson M.J. (1982), J. Phys. D: Appl. Phys. 15, 237
7. Peterson T. (1979), In "Erosion; Prevention and Useful Applications", STP 664 ASTM Philadelphia, Pa. (ed. W.F. Adler) p.279
8. Schmitt G.F. (1970), Proc. 3rd Int. Conf. on Rain Erosion (eds. A.A. Fyall and R.B. King), R.A.E. Farnborough, U.K. p.107
9. Van der Zwaag S. and Field J.E. (1982), Phil. Mag. A 46, 133
10. Van der Zwaag S. and Field J.E. (1983), Phil. Mag. A 49, 767
11. Walton J.D. and Gorton C.W. (1970), Proc. 3rd Int. Conf. on Rain Erosion (eds. A.A. Fyall and R.B. King), R.A.E. Farnborough, p.209
12. Weaver J.H. (1967), Proc. 2nd Int. Conf. on Rain Erosion, Meersburg, West Germany (eds. A.A. Fyall and R.B. King) R.A.E. Farnborough, U.K. p.401

Figure Captions

- Figure 1 : a) Finite element distribution for double coating systems.
b) Detail of a) near the contact area. The two coatings are indicated.
- Figure 2 : The radial stress field outside the contact area at the surface, interface and substrate for a 5/2/0.015a/0.015a double layer coating system.
- Figure 3 : The radial stress field outside the contact area at the surface, interface and substrate for a 2/5/0.015a/0.015a double layer coating system.
- Figure 4 : Variation of the maximum radial stress in the substrate with normalised coating thickness for mono and double layer coatings. In the case of double coatings $t_1 = t_2$.
- Figure 5 : The maximum radial stress in the substrate as a function of relative coating thicknesses for 5/2 coatings. For $t_1/(t_1 + t_2) = 0$ or 1 the coating consists of a monolayer with $E_c = 2E_s$ and $E_c = 5E_s$ respectively. In all cases $t_1 + t_2 = 0.03a$.
- Figure 6 : The maximum radial stress in the interlayer versus the total coating thickness for various double layer coatings. In all cases $t_1 = t_2$.
- Figure 7 : The maximum radial stress in the outer coating surface versus the coating thickness for double and mono-layer coatings. In the case of double layer coatings $t_1 = t_2$.
- Figure 8 : The fracture stress of macroscopic specimens versus their Young's modulus for various infrared transparent materials.
- Figure 9 : The radial stress field on the coating surface outside the contact area for three 5/2 type coatings with $t_1 = t_2$.
a) $t_1 + t_2 = 0.03a$ b) $t_1 + t_2 = 0.06a$
c) $t_1 + t_2 = 0.12a$
The dashed lines indicate the Hertzian decay for an uncoated halfspace.

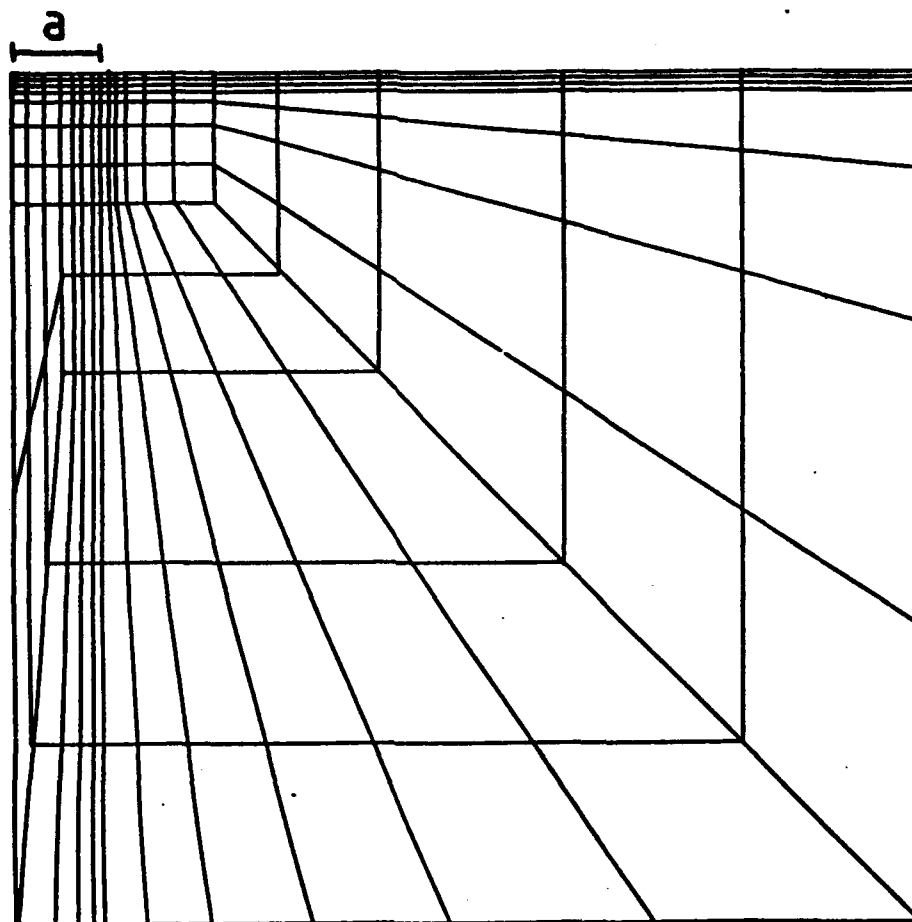


Fig. 1a

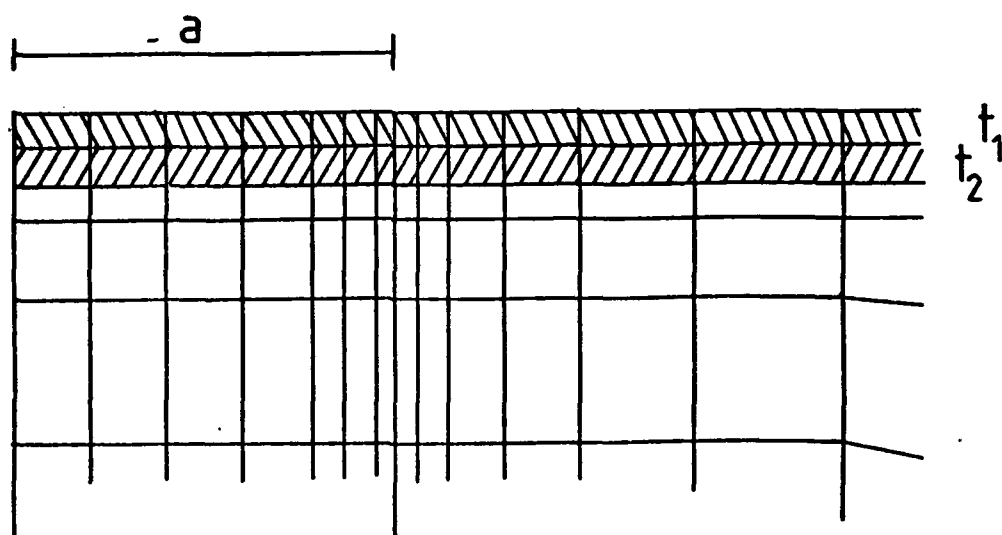


Fig. 1b

Figure 1 : a) Finite element distribution for double coating systems.
 b) Detail of a) near the contact area. The two coatings are indicated.

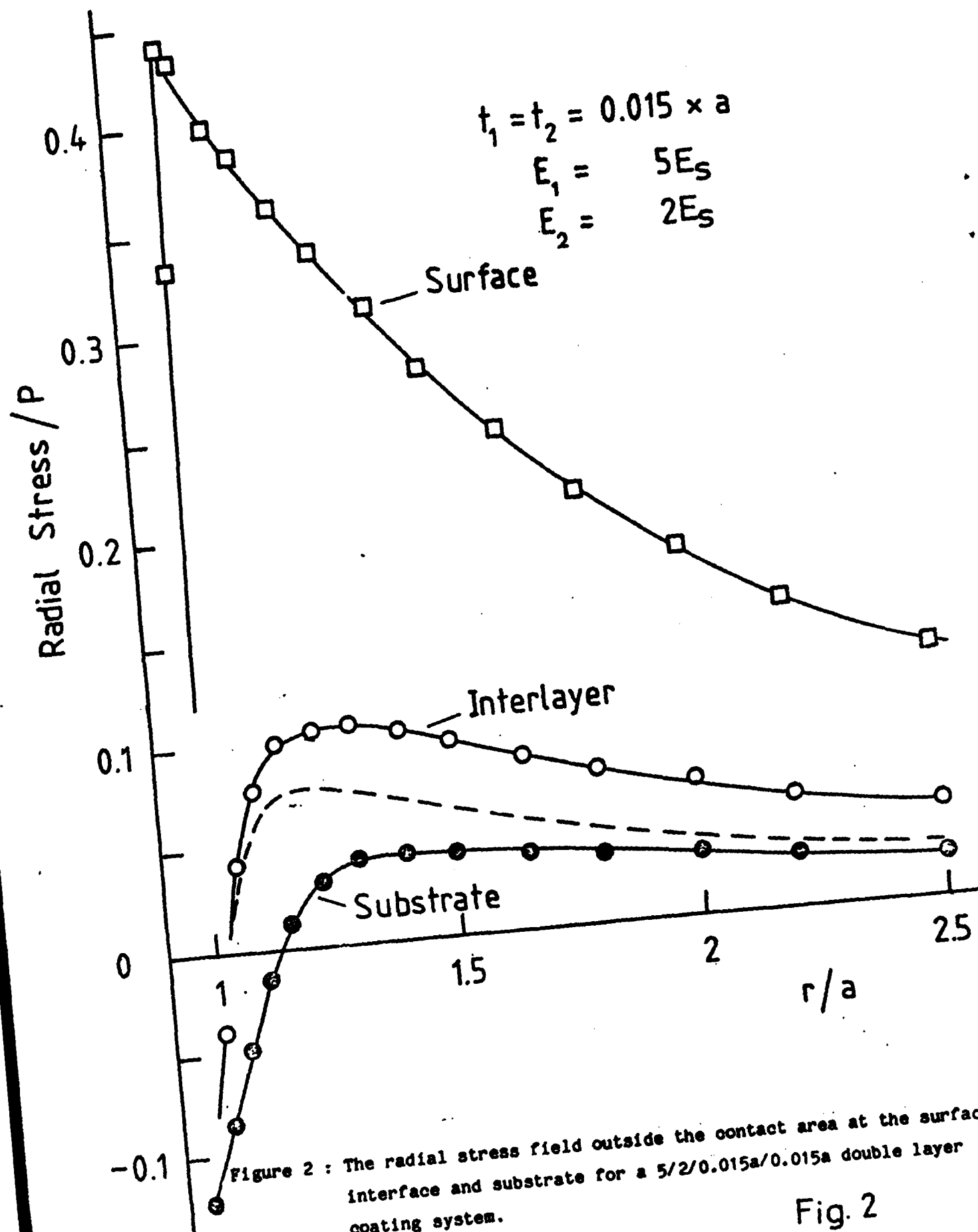


Fig. 2

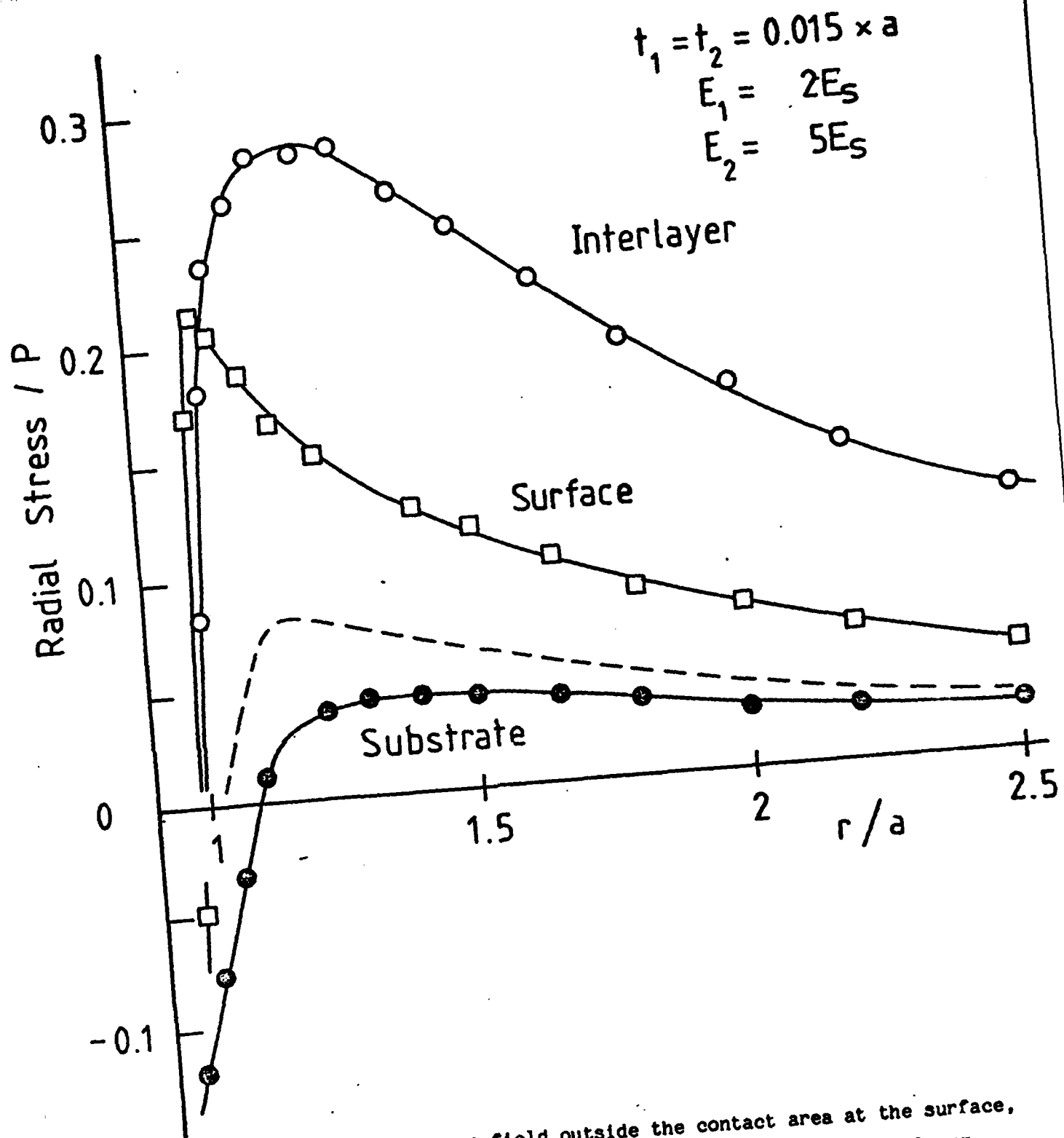


Figure 3 : The radial stress field outside the contact area at the surface, interface and substrate for a 2/5/0.015a/0.015a double layer coating system.

Fig. 3

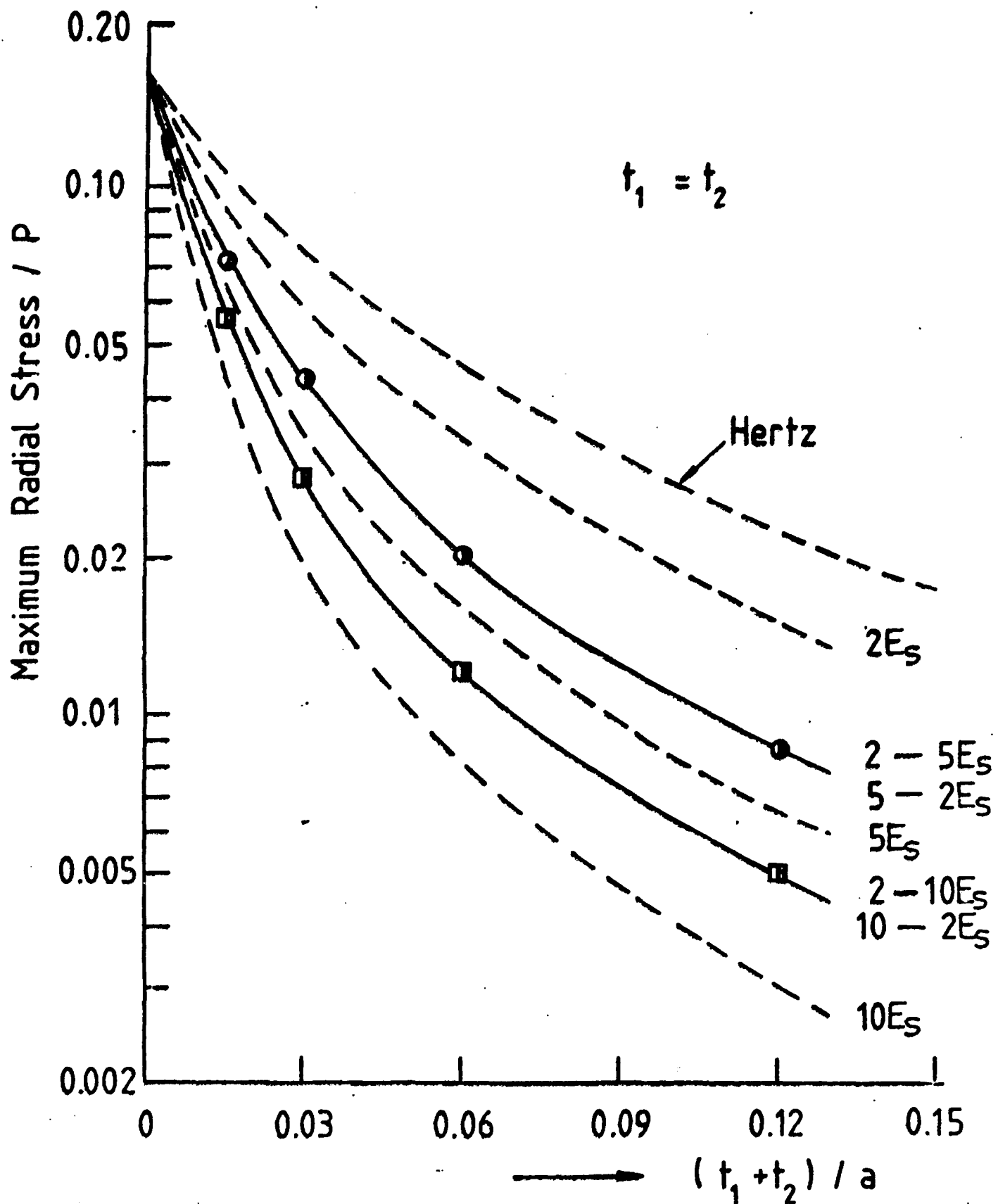


Figure 4 : Variation of the maximum radial stress in the substrate with normalised coating thickness for mono and double layer coatings. In the case of double coatings $t_1 = t_2$.

Fig.4

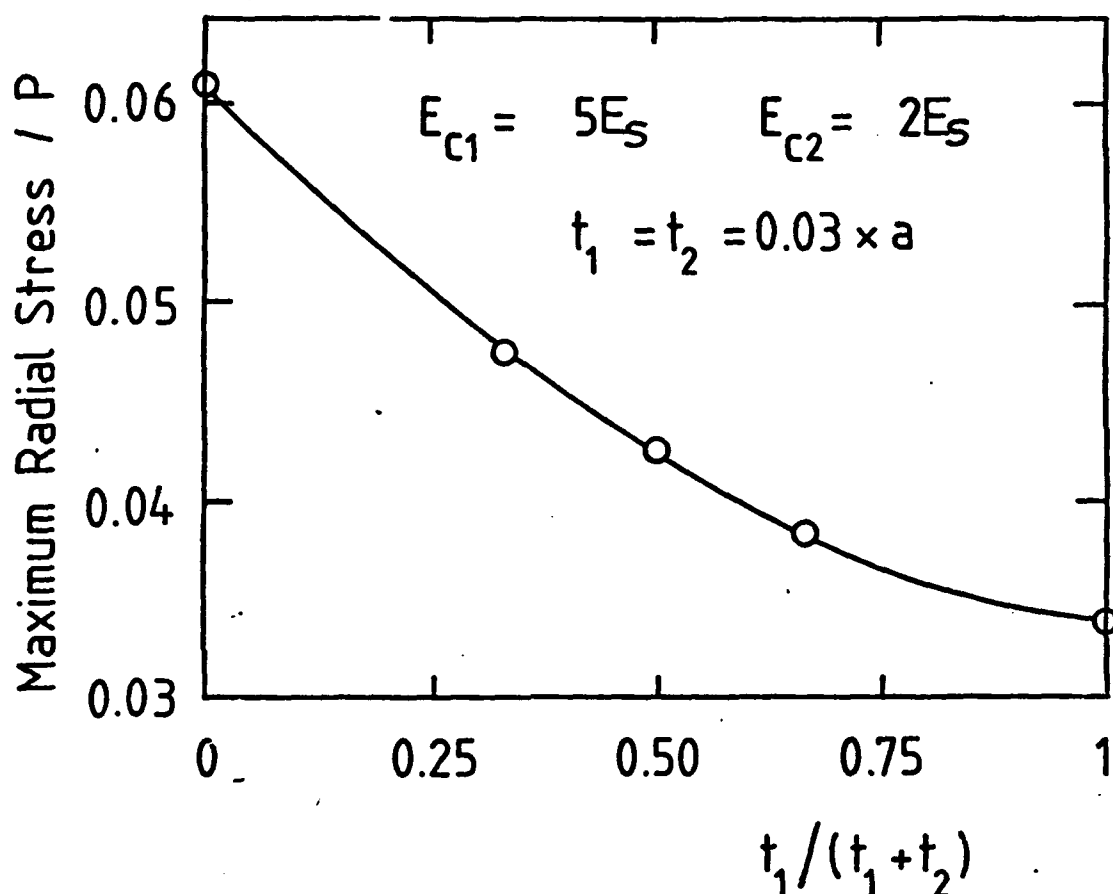


Figure 5 : The maximum radial stress in the substrate as a function of relative coating thicknesses for 5/2 coatings. For $t_1/(t_1 + t_2) = 0$ or 1 the coating consists of a monolayer with $E_c = 2E_s$ and $E_c = 5E_s$ respectively. In all cases $t_1 + t_2 = 0.03a$.

Fig. 5

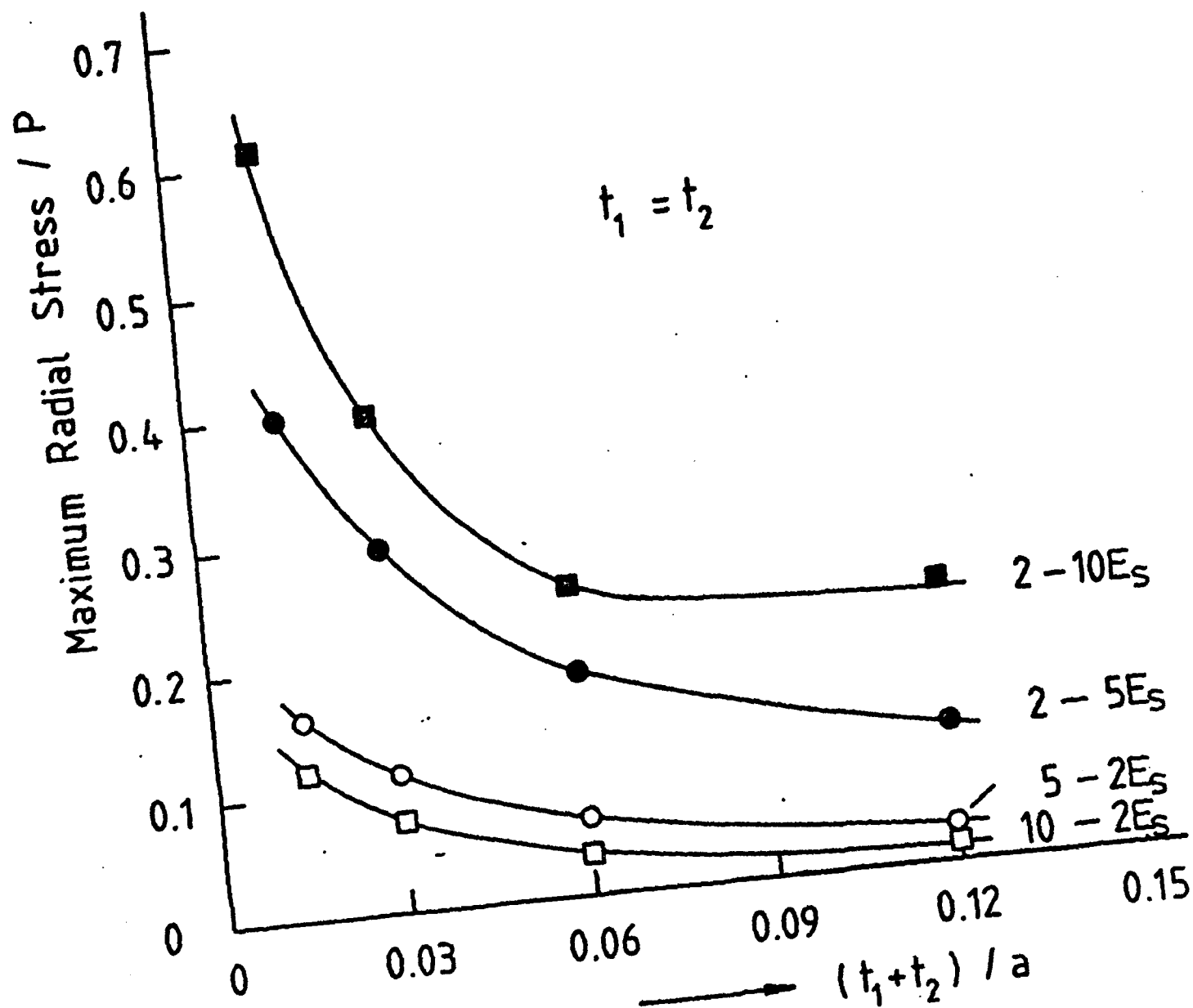


Figure 6 : The maximum radial stress in the interlayer versus the total coating thickness for various double layer coatings. In all cases $t_1 = t_2$.

Fig. 6

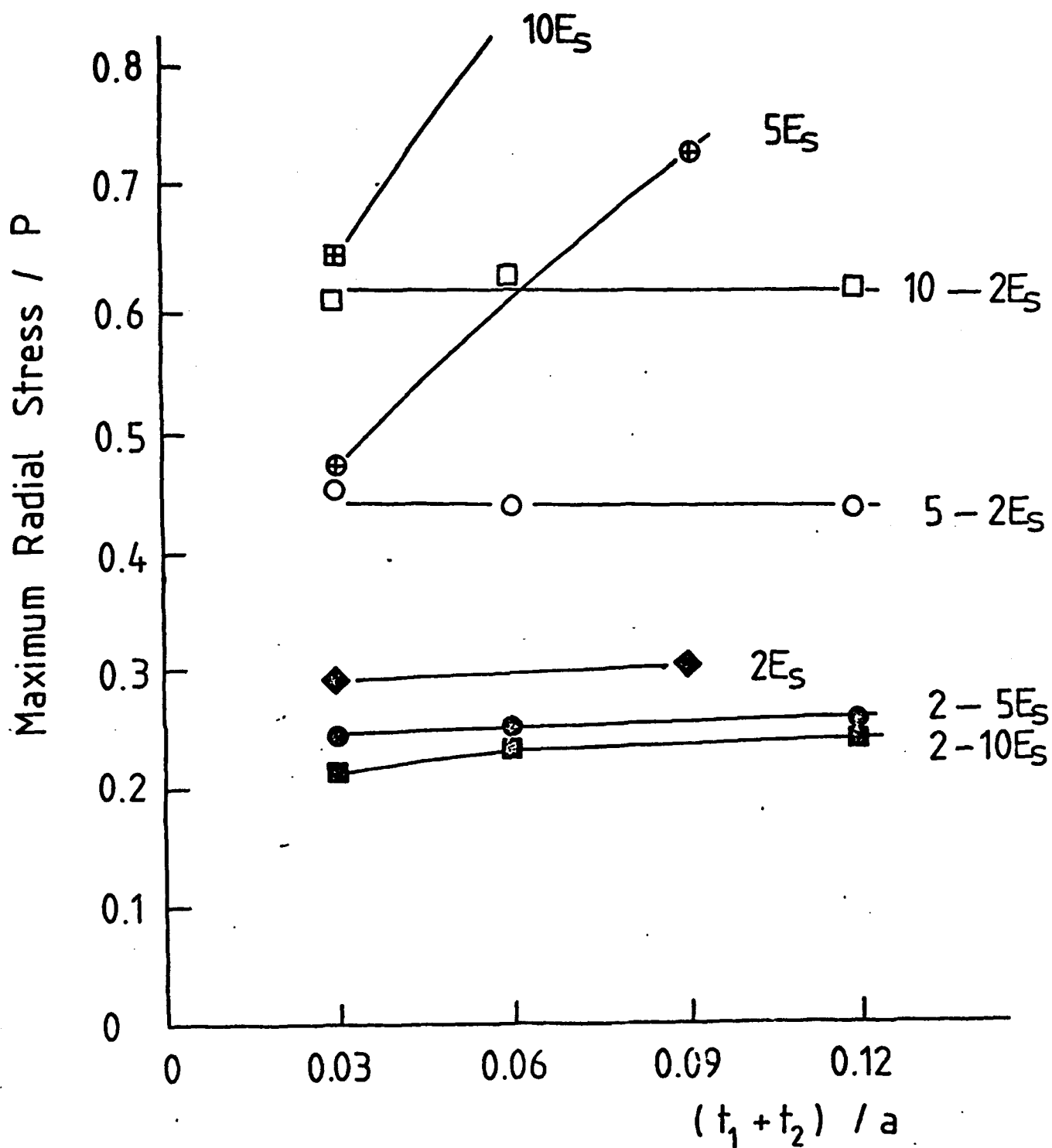


Figure 7 : The maximum radial stress in the outer coating surface versus the coating thickness for double and mono-layer coatings. In the case of double layer coatings $t_1 = t_2$.

Fig.7

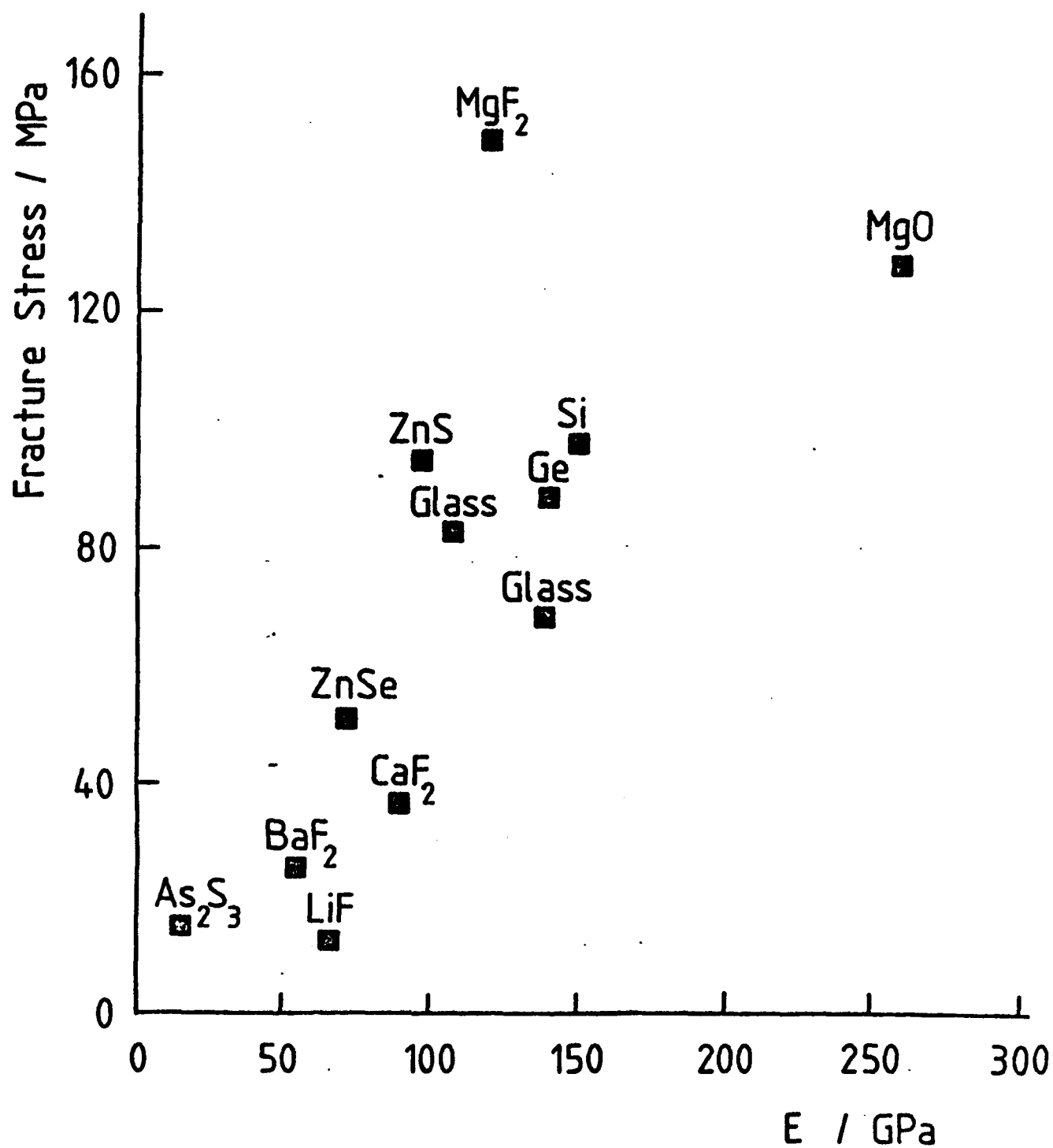


Figure 8 : The fracture stress of macroscopic specimens versus their Young's modulus for various infrared transparent materials.

Fig. 8

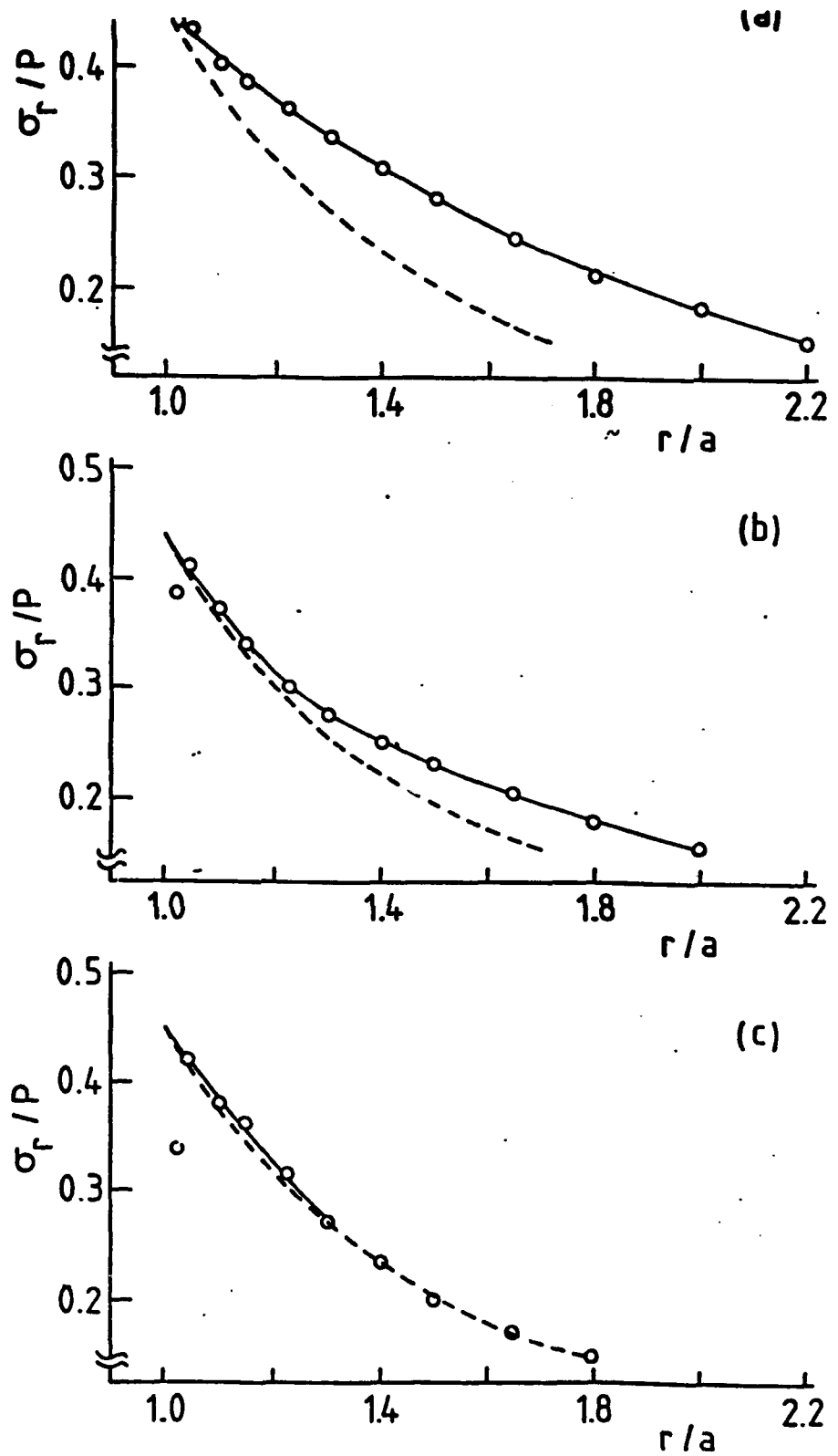


Figure 9 : The radial stress field on the coating surface outside the contact area for three 5/2 type coatings with $t_1 = t_2$.

a) $t_1 + t_2 = 0.03a$

b) $t_1 + t_2 = 0.06a$

c) $t_1 + t_2 = 0.12a$

The dashed lines indicate the Hertzian decay for an uncoated halfspace.

SECTION V

COMPRESSIVE STRESS-STRAIN CURVES OF VARIOUS POLYMERS AT STRAIN RATES OF $2 \times 10^4 \text{ s}^{-1}$

5.1 INTRODUCTION

The apparatus used in these experiments (fig. 1) was designed in this laboratory by Gorham and Field (see Gorham 1979 for a description). It was built because it was desired to obtain stress-strain curves for very hard materials at higher compressive rates of strain than is possible in a conventional Hopkinson bar. To do this, the input bar was dispensed with and the apparatus was miniaturised; the bar has a diameter of 3 mm and the metal specimens used were 1 mm in diameter and 0.5 mm thick. The specimen is mounted on the end of the output bar and impacted directly by a metal rod which has been accelerated in a sabot by a gas-gun. Typical impact speeds are ca. 20 m s^{-1} , implying for a 0.5 mm thick specimen an initial strain rate of ca. $4 \times 10^4 \text{ s}^{-1}$, assuming the surfaces are constrained to move at the same speed as the striker. The advantage of dispensing with the input bar was that problems of dispersion were overcome. Dispersion tends to reduce the strain rate experienced by the specimen in a conventional bar because the high frequency Fourier components of the stress pulse travel more slowly than the low frequency components (Davies, 1948). Thus, by the time the pulse has travelled down the input bar to the specimen, the loading rate has dropped considerably. In a conventional Kolsky apparatus, typical strain rates achieved are only ca. 10^3 s^{-1} . However, the absence of an input bar in our method means that only one set of force measurements can be made, ie. those of the wave propagating down the output bar. To obtain the stress and the strain at any time, the instantaneous specimen dimensions must be found in some way. The original method was to follow the radial expansion using high speed photography (the camera used was a Hadland Image Converter camera or Imacon). The specimen strain $\epsilon(t)$ is then given by:

$$\epsilon(t) = 2 \ln(D(t)/d_0) \quad (1)$$

where $d(t)$ is the diameter at any time and d_0 is the original diameter. The specimen stress $\sigma(t)$ is given by:

$$\sigma(t) = 4F(t)/\pi(d(t))^2 \quad (2)$$

where $F(t)$ is the force deduced from the calibrated strain gauges on the output bar. A plot of $\sigma(t)$ against $\epsilon(t)$ gives the stress-strain curve (the moment of impact is known to better than $1 \mu\text{s}$).

Direct observation enables the actual behaviour of specimens to be

seen during impact. Gorham (1979) was able to determine the best lubrication conditions to assure uniform uniaxial compression, the technique being extremely sensitive to non-uniformities induced by plastic waves. If the lubricant jetted, this could be seen and discounted, which is not the case if a light beam/photodiode system is used to measure the expansion. Measurements from the photographs gave up to 14 data points on a strain-time graph with accuracies of 0.01 in strain and 0.1 μs in time. This work is the standard against which alternative methods must be compared.

There are some disadvantages, however: (i) the strain is obtained as a series of discrete points (up to ca. 14). At a framing speed of 10 m s^{-1} , only at most 14 μs of data can be obtained, whereas the load can be applied for up to 30 μs , depending on the projectile used. (ii) Data processing is slow as each experiment requires the measuring of several lengths on a photograph; (iii) the method only measures displacement along one radius vector, so that if for any reason (such as localised shear banding) the displacement were different along the line of sight, the area over which the force is acting would be calculated wrongly, and hence also the stress and the strain (from equations 1 and 2). For these reasons, Pope and Field (1984) developed a method of computing the strain from the force-time data directly. Another motive for this calculation was to try and estimate the inertial stresses, for polynomial fits to the data when differentiated twice to find the strain acceleration gave answers that were very sensitive to the fitting coefficients, so that estimates of these stresses varied by orders of magnitude.

Their method is as follows. If the specimen is sufficiently thin, the force acting on the face where the projectile is striking equals the force transmitted through the back face at any instant into the output bar, i.e. there is no stress gradient; this is the assumption of quasi-static equilibrium. A timescale for this to be established can be found from stress-wave theory (Briscoe and Nosker, 1984). When the projectile strikes the specimen, a wave propagates from the interface into the polymer and the striker. If we assume an initial elastic response for the polymer, the stress attained during the first wave transit of the specimen is:

$$\sigma_t = \frac{2(Z_2/Z_1)\rho c v}{1+(Z_2/Z_1)(A_2/A_1)} \quad (3)$$

(Graff, 1975, pp 84-97) where the subscripts 2 refer to the polymer, 1 to the striker and Z is the material acoustic impedance, A is the cross-sectional area, ρ is the density of the striker, c its wave speed and v

its impact velocity. Using the following (approximate) values, σ_t can be calculated: if $Z_2 = 10^6 \text{ kgm}^{-2} \text{ s}^{-1}$, $Z_1 (= \rho c) = 20 \times 10^6 \text{ kgm}^{-2} \text{ s}^{-1}$, $A_1 = 7 \times 10^{-6} \text{ m}^2$, $A_2 = 2 \times 10^{-6} \text{ m}^2$, $v = 20 \text{ m s}^{-1}$, then $\sigma_t = 90 \text{ MPa}$. This is above the value of the yield stress of the very softest polymers tested, but below that of most (see Table 1). Thus a few of the polymers yield during the first wave transit, whereupon the impedance of the polymer drops to the value appropriate to the local slope of the stress-strain curve. For the speed of plastic waves is given by

$$c_p = \sqrt{\frac{1}{\rho} \frac{\delta \sigma}{\delta \epsilon}} \quad (4)$$

(Johnson, 1972, p.214).

If the material flows at constant stress, which most of the polymers tested do, then $Z_2 = 0$ and hence from equation 3, $\sigma_t = 0$. This means that no further stress wave activity occurs and the assumption of quasi-static equilibrium is valid from ca. $1 \mu\text{s}$ onwards, for the elastic wave speed in polymers is ca. 1000 m s^{-1} (Kolsky, 1956; Theocaris and Papadopolou, 1978) and the specimens are 1 mm thick.

If the transmitted stress does not reach the yield stress on the first transit, elastic stress wave activity persists, building up the stress in a step-wise manner. In our particular case, we have a polymer sandwiched between an impacting titanium alloy rod and a steel output bar. Our calculations show that all the polymers we have tested so far should have yielded by the time 4 or $5 \mu\text{s}$ have passed. The point of this calculation is to give a timescale for the onset of plasticity in this experiment.

After $4 - 5 \mu\text{s}$, the length $l(t)$ of the specimen is given by

$$l(t) = l_0 - vt + u_1(t) + u_2(t) \quad (5)$$

where l_0 is the initial length (or thickness), and $u_1(t)$, $u_2(t)$ are the displacements of the surfaces of the pressure bar and projectile due to their elastic compression. u_1 and u_2 may be expressed in terms of the particle speeds at the ends of the two rods, thus:

$$u(t) = \int_0^t v(t') dt' \quad (6)$$

where the zero of time is the instant of contact. The acoustic impedance Z_r of the rod allows the particle velocity to be related to the force $f(t)$ acting on its end, for

$$Z_r = f/v \quad (7)$$

(Graff, 1975, p.84). Since we measure separately the acoustic impedance Z of the material of the rod (which equals Z_r/A , where A is its cross-sectional area),

$$Z = f(t)/Av(t) \quad (8)$$

Substituting this into equation 6 gives

$$u(t) = (1/ZA) \int_0^t f(t') dt' \quad (9)$$

Now in general the projectile and pressure bar have different acoustic impedances Z_1 , Z_2 but the same cross-sectional area. So substituting for $u_1(t)$ and $u_2(t)$ in equation 3 gives

$$l(t) = l_0 - vt + (Z_1 + Z_2)/(Z_1 Z_2 A) \int_0^t f(t') dt' \quad (10)$$

This expression is valid during the period in which the stress wave launched into the projectile at the start of the impact travels down it and back again, ie. for a time

$$t = 2l/c \quad (11)$$

where $2l$ is the length of the projectile and c the longitudinal wave speed in the rod material (the pressure bar is much longer than the striker). This time can be found by performing a direct rod impact (ie. with no specimen present). For a 70 mm long Ti rod, the "time window" for the experiment was measured to be 30 μ s.

All the terms in the RHS of equation 10 can be measured or recorded. v is found by causing the striker to pass through three light beams of known separation shining through the barrel of the gas-gun onto photodiodes (three are used so that a correction can be made for any acceleration that is occurring (see fig. 1)). $f(t)$ is recorded using two small semiconductor strain gauges mounted either side of the pressure bar a sufficient distance from the end so that the stress at the surface (where the gauges are) is the same as in the bar interior. Kennedy and Jones (1969) analysed this problem (the dynamic St. Venant principle). They concluded that differences in average dynamic stresses and strains were negligible at distances greater than 5 bar diameters from the end, but one needed to go to 20 bar diameters to make differences in peak values negligible for various radially varying end stress distributions. Our gauges are placed at 10 bar diameters (S in fig. 1) as a compromise with dispersive effects. Two are used so that the effect of flexural waves is cancelled out. Their small size (150 x 100 μ m) means that the smallest time they are sensitive to is 30 ns (for a bar with wave speed of 5 km s⁻¹).

The combined output of the gauges is passed to a transient recorder set to sample its inputs every 50 ns. The contents of its memory can be transferred to a microcomputer for analysis. To convert the electrical signal into a force history, the system must be calibrated, and any non-linearity in the gauge response allowed for. A static calibration can be performed in an Instron mechanical testing machine, applying a known

force to the bar ends. Two methods have been used to obtain a dynamic calibration:

Method (1) (in Gorham et al, 1984)

Phosphor-bronze spheres were fired at low velocity from a gas-gun onto the end of the bar, and the impact and rebound speeds found using high-speed photography. This gives the total impulse delivered to the bar. This must equal the area under the volts/time curve multiplied by the gauge calibration factor $K(N V^{-1})$. Thus

$$K \int_0^t V(t') dt' = m \Delta v \quad (12)$$

where m is the mass of the sphere.

Method (11) (in Gorham et al, 1984, and Safford, 1984)

Direct rod impacts are performed at various speeds. If the two rods have the same cross-sectional area but different impedances (Z_1 , for the projectile, Z_2 for the pressure bar), then from equation 3, the stress pulse in the bar is of magnitude:

$$\sigma = \frac{2(Z_2/Z_1)}{1+(Z_2/Z_1)} \rho c v \quad (13)$$

The duration of this pulse t is given by equation 18, so that the total mechanical impulse passing the strain gauges is

$$\sigma t = \frac{2(Z_2/Z_1)}{1+(Z_2/Z_1)} \rho v l \quad (14)$$

The gauge calibration factor is then given by

$$K \int_0^t V(t') dt' = \frac{2(Z_2/Z_1)}{1+(Z_2/Z_1)} \rho v l \quad (15)$$

Gorham et al (1984) found that the expression

$$F = K(1 + bV)V \quad (16)$$

was adequate to compute the force accurately. For their bar, they found $bV = 0.02$ and $b = 0.05 V^{-1}$. Safford (1984) found that for our system $K = 10010 \pm 0.5\% N V^{-1}$ and $b = 0.13 V^{-1}$. Each bar-gauge system will have to be independently calibrated.

As has been already mentioned, the gauges are mounted some 10 bar diameters from the end (which is the lower end of the range suggested by Kennedy and Jones, 1969) because of dispersion effects. Photographs of the voltage output from the gauges show oscillation named after Pochhammer and Chree. The effects of the different wave speeds for different frequency components of the stress pulse are that the rise time is

lengthened to about 1 μ s and the height of the stress pulse is lowered. It is hoped soon to implement a Fast Fourier Transform technique which will use an experimentally determined amplitude-phase relationship for the bar to work out what the force pulse at the specimen must have been to produce the pulse measured at the gauges. When this is done, it should improve our confidence in the first few microseconds of data, so that yield phenomena may be reliably observed. At the present, although the stress-strain curves obtained look like typical elastic-plastic graphs measured say in an Instron, the Young's modulus and the yield strain are almost certainly not what they appear to be on the graph. At best, the initial slopes of the curves are lower bounds on the modulus. The position of the gauges then is a compromise between satisfying St. Venant's principle (where the spatial details of the loading no longer matter) and dispersion.

5.2 PRESENT EXPERIMENTS

The polymer specimens tested to date were solid cylinders of diameter 2 mm and thickness 1 mm. These were made from sheets of the material (wherever possible) bought from a local supplier, or from thin cuts turned from rods. The best tool for cutting out the specimens was found to be a leather punch, but some polymers were either too tough or too brittle for this approach. These polymers had to be tackled using a specially made miniature flat-ended punch. A few polymers have been obtained in 0.5 mm thick sheets, so that specimens 1 mm in diameter with this thickness have been prepared, but they have not been tested yet. These very small specimens should allow the strain rate to be raised by a factor of about 4 (approaching 10^5 s^{-1}).

Fig. 2 shows photographs of an oscilloscope display of the electrical signal from the strain gauges when two different specimens of nylon 6 were impacted by the 50 mm long silver steel bar. The rising portion can be seen to last 20 μ s before it either flattens off (fig. 2a) or starts to unload (fig. 2b). The top trace is "ideal" and smooth, the lower trace shows the force rising in a staircase manner which may be due to stress wave activity (as analysed before) to to over-generous lubrication leading to jetting.

If the specimen were exactly central, the maximum strain achievable before the disc equalled the bar diameter would be given by

$$\epsilon_{\max} = 2 \ln(3/2) = 0.81 \quad (17)$$

for 2 mm diameter specimens. If a low impact speed is used, the 30 μ s would be up before this strain was reached. But for a high speed, this

value (0.80 was in fact used) terminates the calculation.

It should be noted here that the calculation of strain assumes volume conservation, i.e. $v_{pl} = 0.5$. G'Sell and Jonas (1979) found that in low strain-rate tensile tests, the total strain deviated from the rigid-plastic strain by

$$(1 - 2v_{el})(\sigma/E)$$

which was a small correction, especially at high plastic strains (<1%). A high strain-rate test, however, is intrinsically adiabatic, so that the work done on the material which is dissipated as heat (ca. 90%, Taylor and Quinney, 1934) raises its temperature. The magnitude of this effect depends on the yield stress σ_y , because the work done is $\sigma d\epsilon$. For the PC specimens used, this amounts to ca. 0.3 J at a strain of 0.8. The heat capacity of the specimens is ca. $3 \times 10^{-3} \text{ J K}^{-1}$ which implies a temperature rise of ca. 100 K. The linear thermal expansion coefficient is ca. $7 \times 10^{-5} \text{ K}^{-1}$, so the volume expansion is ca. 2% at maximum strain. Thus the calculation will become erroneous by this sort of amount towards the end of the data.

Fig. 3 shows nylon 6 specimens before (top) and after an experiment with an accompanying force-time trace from the gauges. Note that in this case with the Ti bar, the rise lasts 30 μs . The specimens were cut out using a leather punch, which produces a good circular cylinder but with concave sides. This non-uniformity seems to be inevitable with any cutting or punching technique applied to polymers. The deformed specimens, with one exception, have been punched through by the projectile and squeezed to one side. This must have occurred after the force data were obtained, for the projectile only moves ca. 0.6 mm in this time. Any error produced by slightly angled impacts seems to be well within the experimental scatter. The nylon 6 stress-strain curves plotted in fig. 4 were all obtained with the silver steel projectile. The one curve obtained with the Ti rod agrees very well (fig. 5). All subsequent polymers were tested with the Ti rod.

There are several points to be made about these curves: (i) before the stress and the strain are calculated, the force-time data are smoothed using a moving average algorithm. (ii) They do not pass through the origin because the force-time graph contains a point of inflection, so that it was decided to reject that part of the measured impulse occurring before that point from the calculation as being "unphysical". (iii) No values for the dynamic Young's Modulus or yield strain can legitimately be read off these graphs because of dispersion in the bar and wave effects in the specimens (in the initial few microseconds). Thus only flow stresses

are given in Table 1. The error in the flow stress is taken as half the width of the band of lines of maximum stress in the various stress-strain graphs.

Most of the polymers studied so far yielded with almost constant flow stress (at least up to the maximum strain we can achieve, 0.8 with 2mm diameter discs): nylon 6, nylon 66, Noryl, PC, PP, PE. Noryl showed slight strain softening up to a strain of 0.4 and then strain hardened (fig. 6). PC showed strain hardening for strains greater than 0.4 (fig. 7). PTFE showed the greatest tendency to strain harden, at least when impacted at 20 m s^{-1} ($\epsilon = 2 \times 10^4 \text{ s}^{-1}$). Under these conditions, large oscillations in the force were observed near the beginning of the impact which were not seen in any other polymer. At this impact speed, the specimens shattered, as did PC specimens. Reducing the impact speed allowed deformed specimens of both polymers to be recovered, and also the oscillations were not seen in PTFE with these gentler conditions. PMMA was found to be very difficult to prepare specimens from, due to cracking. Only two impacts have been performed so far on this material and it is felt that stress-strain curves computed from this data are not meaningful. As in the case of PTFE, Noryl and PC (if hit sufficiently fast, a load drop was seen). Those polymers sufficiently ductile to deform to greater than the bar diameter showed a steadily rising force (with the exception of the nylons) until saturation of the transient recorder was reached. The soft ductile polymers, such as PE and PP, ended up as rings, for the projectile punched right through them. Substantial recovery must have occurred after impact, however, since the inner diameter of the rings was less than the bar diameter.

The results of the research to date on polymers is summarised in Table 1, along with quasi-static values from a reference book, and flow stresses obtained by us using a drop-weight machine. Note the significant increase in the yield stress for the polymers at the higher strain rates. This ratio ranges from 1.42 for PC to ca. 3.5 for a soft polymer such as PP. In some cases, we need to complete measurements on some of the polymers at low strain rates (10^{-3} s^{-1}) on well-characterised samples. This work is in progress.

Now that the techniques are established it would be relatively straightforward to obtain data on other materials.

Table 1

Compressive uniaxial yield stresses/flow stresses for various
polymers at various strain rates (figures in MPa)

Polymer	Instron (10^{-3}s^{-1})	Impact bar ($2 \times 10^{-3}\text{s}^{-1}$)	Ratio dynamic/ static
Nylon 6	86 ± 2 (48 - 97)	150 ± 10	1.7
Nylon 66	86 ± 6	165 ± 5	1.9
PC	70 ± 1	100 ± 5	1.4
Noryl (PPO)	76 ± 5 (102 - 104)	120 ± 5	1.6
HDPE	(16.5)	30 ± 5	1.8
PP	20	70 ± 5	3.5
PTFE	(5 - 12)	25 ± 5	2.9

Note: the figures in brackets were obtained from "Properties of Plastics", published by Shell Chemicals. The rest have been measured by us.

REFERENCES

- Briscoe B.J., Nosker R.W. - Wear 1984 95, 241-262
- Davies E.D.H., Hunter S.C. - J. Mech. Phys. Solids 1963 11, 155-179
- Davies R.M. - Phil. Trans. R. Soc. Lond. 1948 A240, 375-457
- Gorham D.A. - Proc. 2nd Int. Conf. on Mechanical Properties of Materials at High Rates of Strain, Oxford 1979, 16
- Gorham D.A., Pope P.H., Cox O. - Proc. 3rd Int. Conf. on Mechanical Properties at High Rates of Strain, Oxford 1984, paper 18
- Graff K.F. - Wave Motions in Elastic Solids, Clarendon Press, Oxford 1975
- Kennedy L.W., Jones O.E. - Trans. ASME: J. Appl. Mech. 1969 36, 470-478
- Kolsky H. - Phil. Mag. 1956 1, 693-710
- Pope P.H., Field J.E. - J. Phys. E: Sci. Instrum. 1984 17, 817-820
- Safford N.A. - Camb. Univ. PGCS Report, Cavendish Laboratory 1984
- Taylor G.I., Quinney H. - Proc. R. Soc. Lond. 1934 A143, 307-326
- Theocaris P.S., Papadopoulou N. - Polymer 1978 19, 215-219

FIGURE CAPTIONS

- Fig.1 Photograph of the miniaturised direct impact Kolsky bar. S strain gauges; B 3mm diameter output bar; G gas-gun.
- Fig.2 Two force-time traces from impacts on Nylon 6 specimens by the 35mm long silver steel rod. Note that loading ceases after 20 μ s.
- Fig.3 (a) Nylon 6 specimens before impact.
 (b) Force-time trace from Ti rod impact.
 (c) Specimens after impact (bottom right is an untested specimen).
- Fig.4 Stress-strain curves for nylon 6 from silver steel impact data.
- Fig.5 Stress-strain curve for nylon 6 from Ti rod impact. Agreement with silver steel data is good.
- Fig.6 Stress-strain curves for Noryl.
- Fig.7 Stress-strain curves for PC.

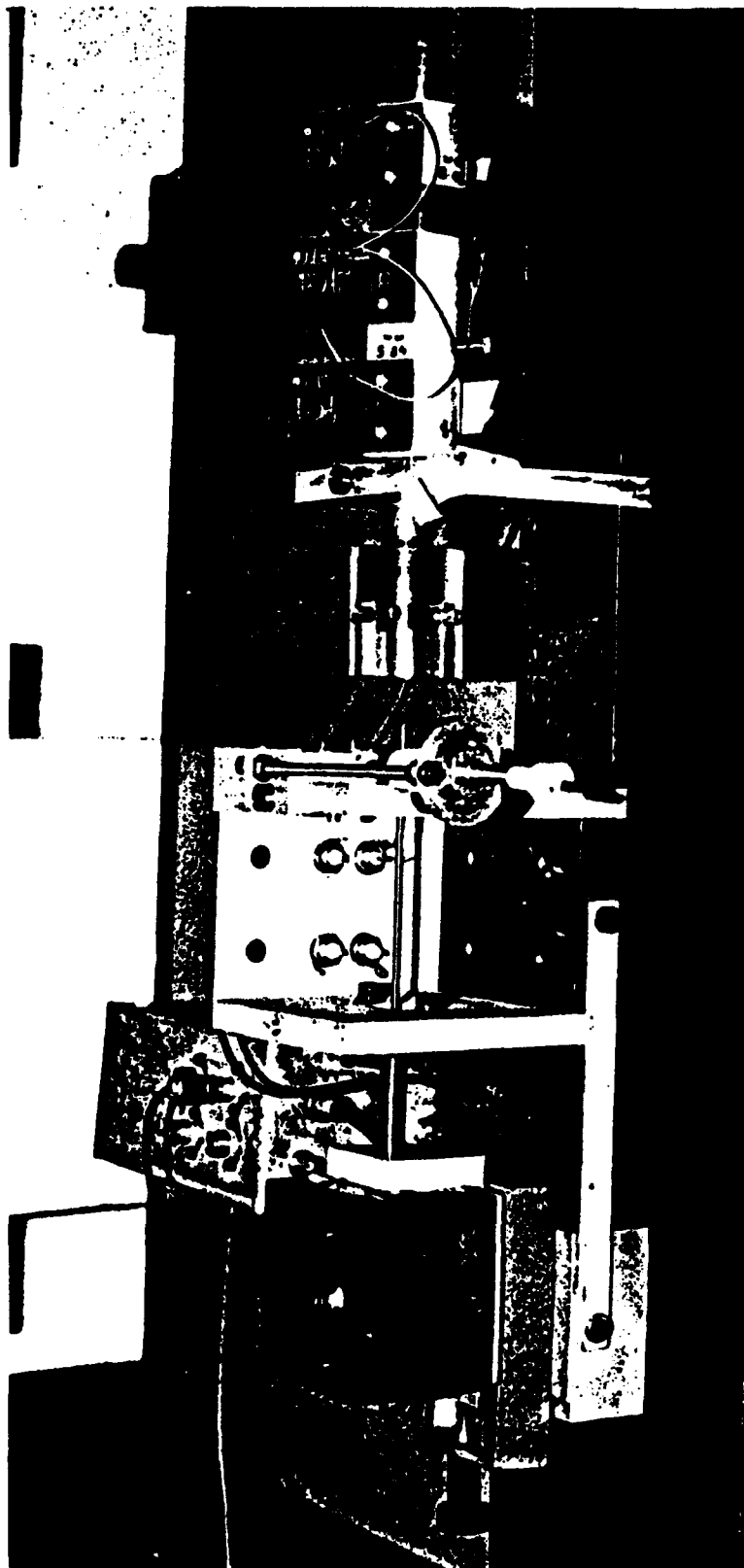
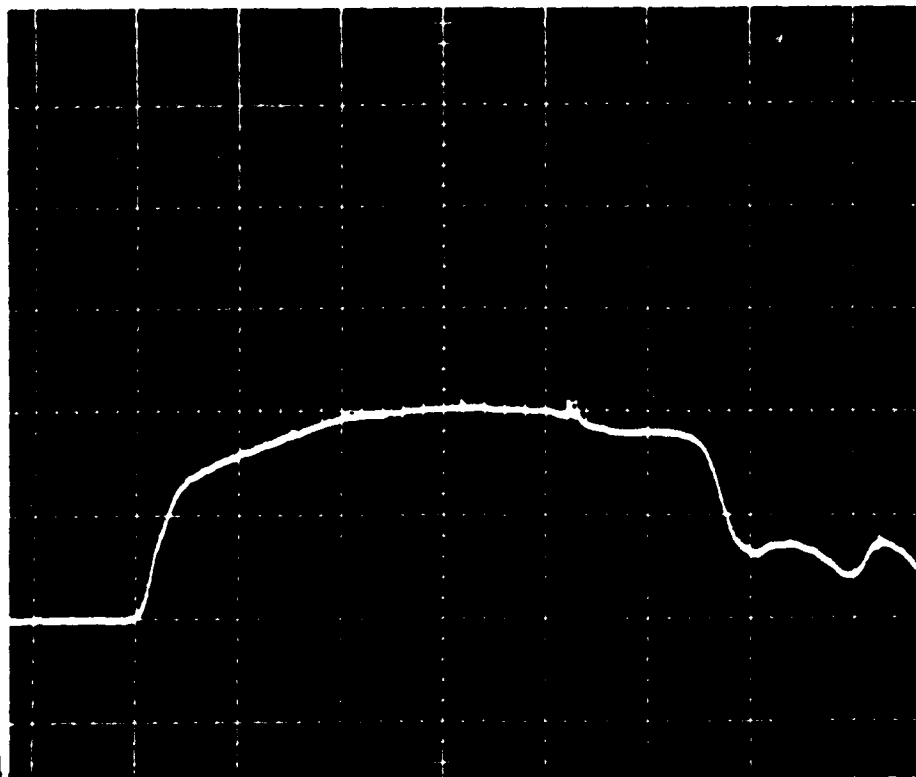


Fig.1 Photograph of the miniaturised direct impact Kolsky bar. **S** strain gauges; **B** 3mm diameter output bar; **G** gas-gun.

2a



2b

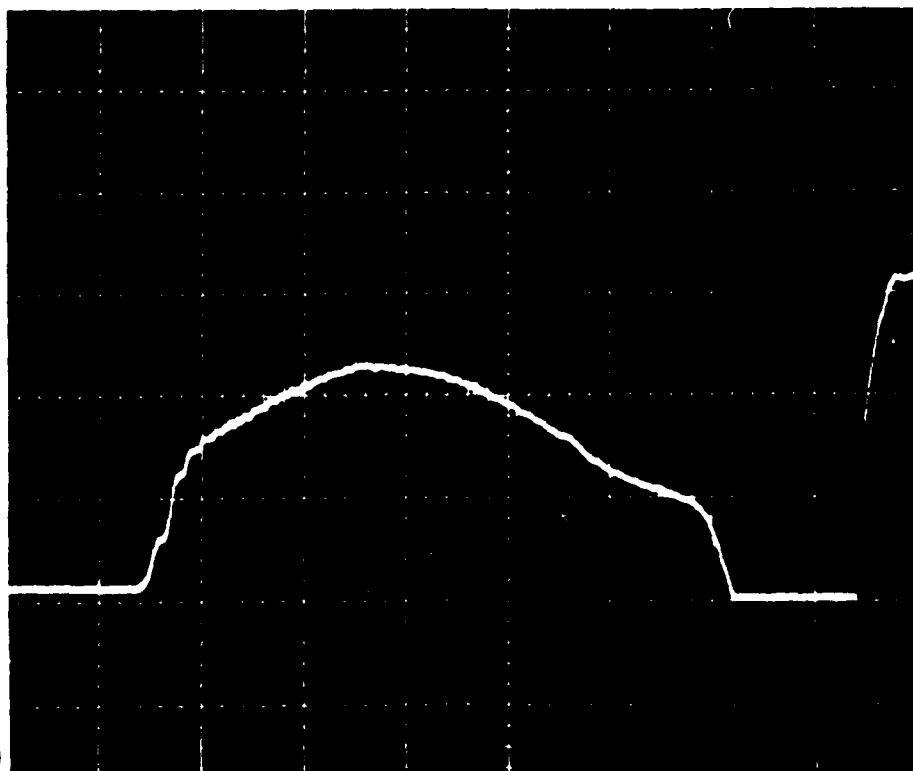
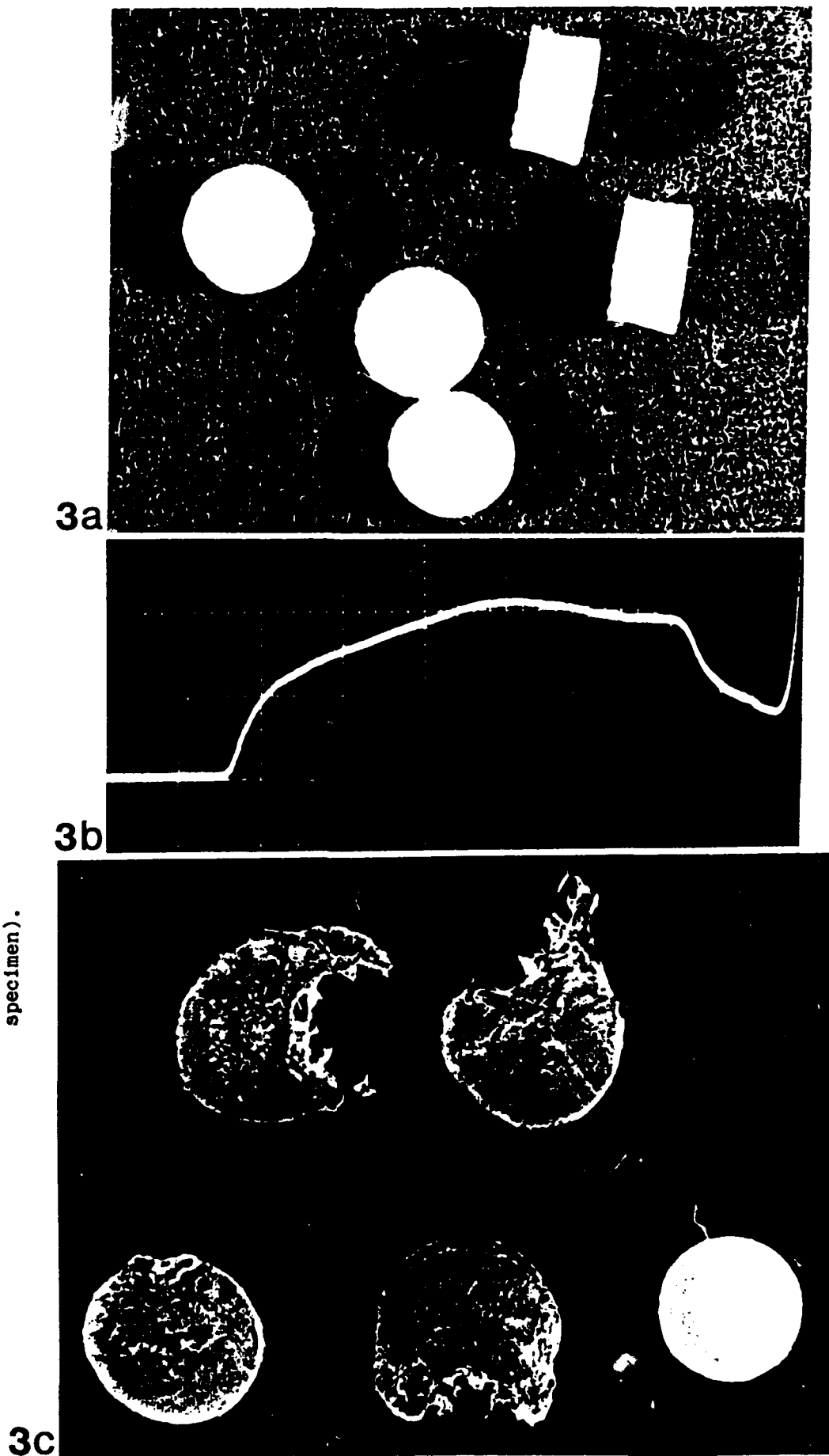


Fig.2 Two force-time traces from impacts on Nylon 6 specimens by the 35mm long silver steel rod. Note that loading ceases after 20 μ s.

Fig.3 (a) Nylon 6 specimens before impact.
 (b) Force-time trace from Ti rod impact.
 (c) Specimens after impact (bottom right is an untested specimen).



N6/17/10

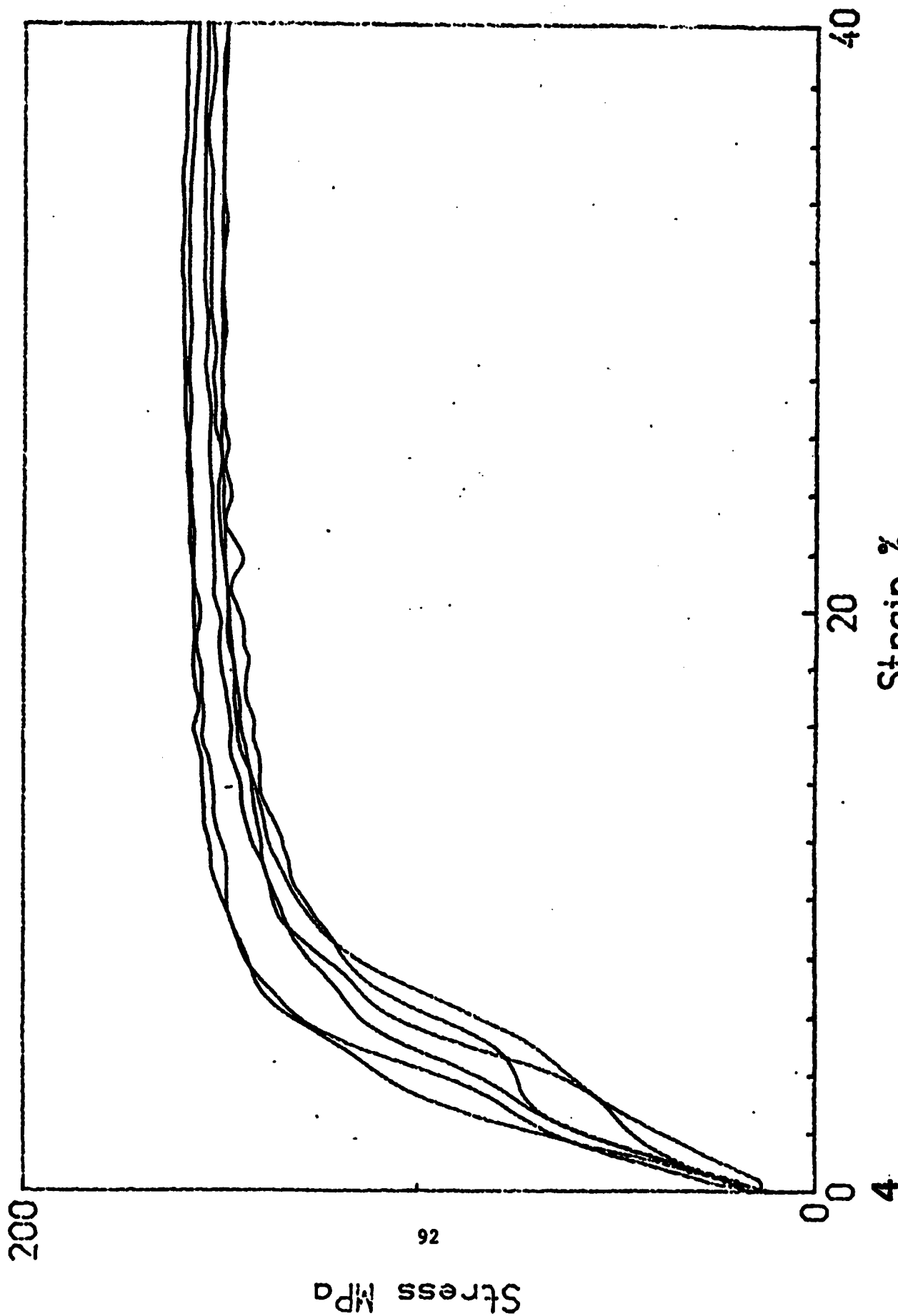


Fig.4 Stress-strain curves for nylon 6 from silver steel impact data.

N6/28/10: 6

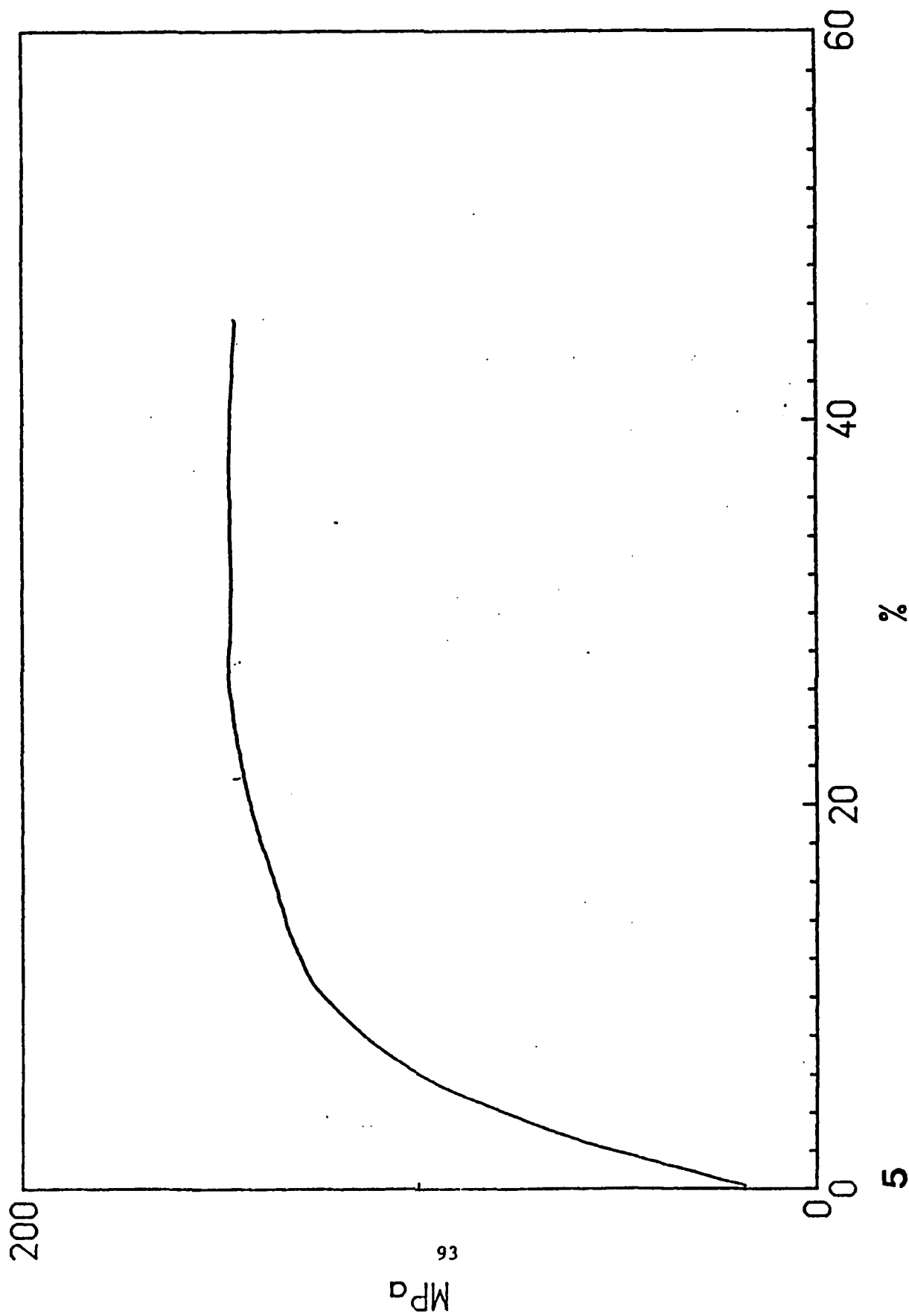


Fig.5 Stress-strain curve for nylon 6 from T1 rod impact. Agreement with silver steel data is good.

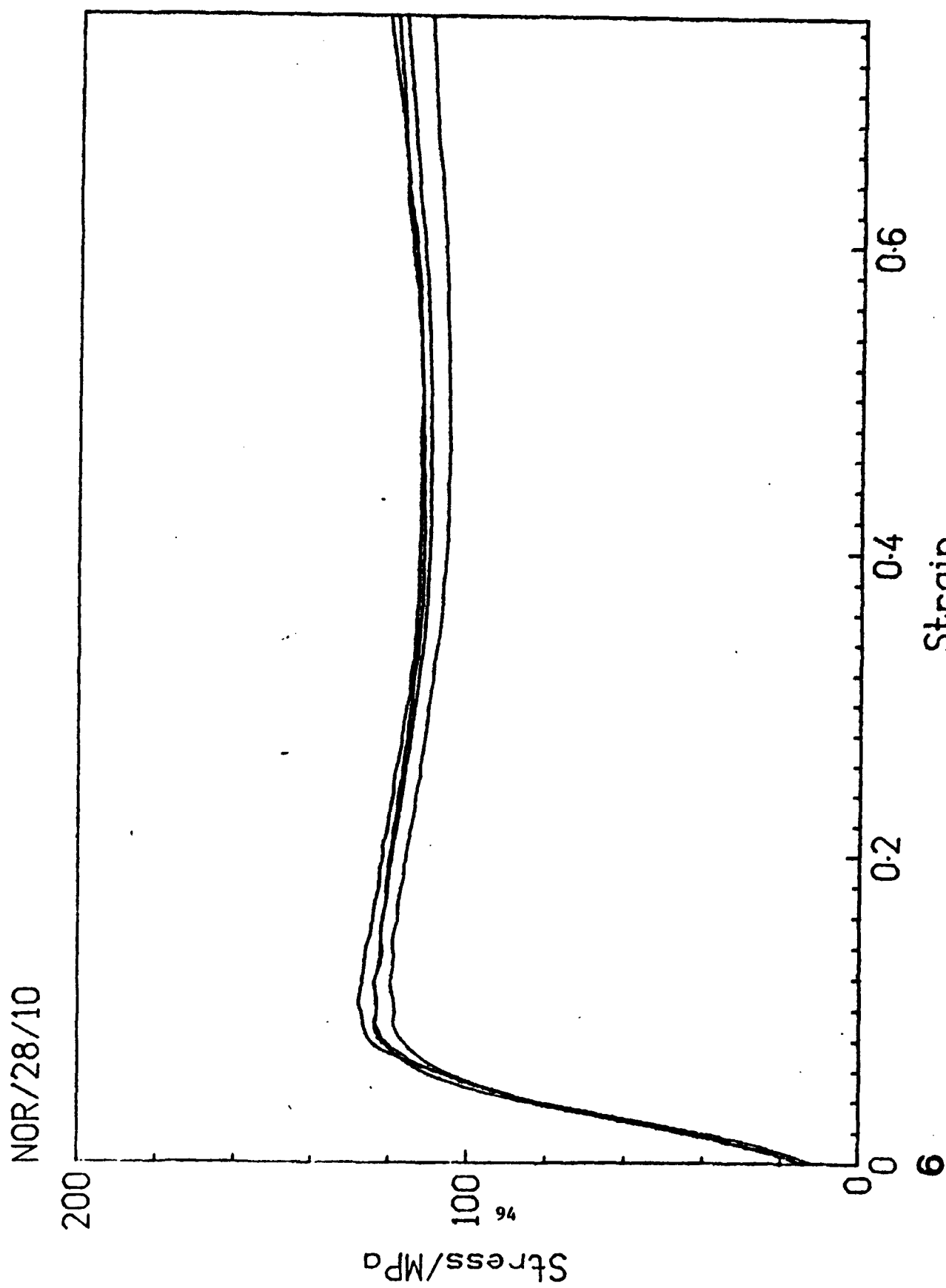


Fig.6 Stress-strain curves for Noryl.

PC/8/11

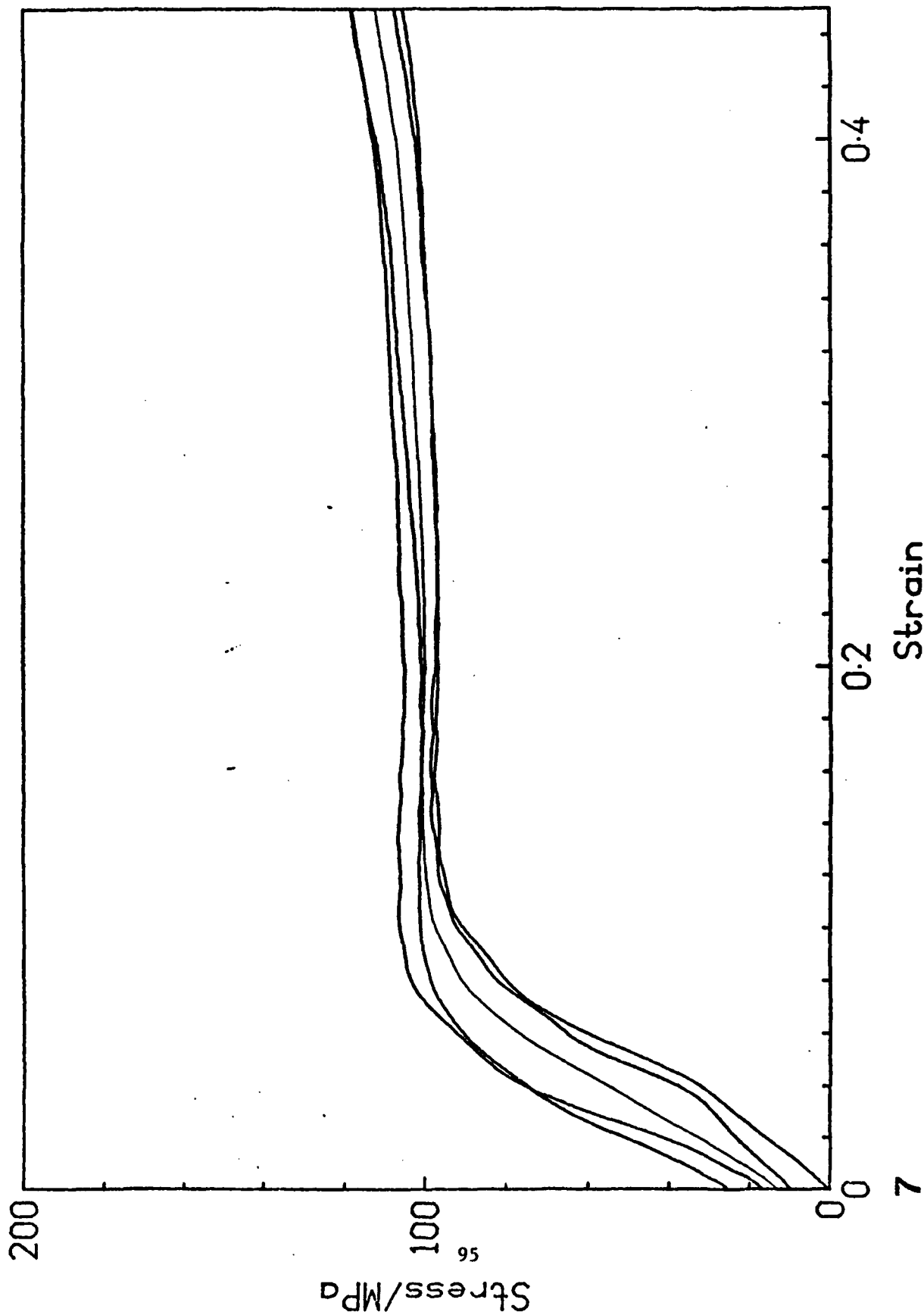


Fig.7 Stress-strain curves for PC.